

ON PHASES OF DNA, ENTANGLEMENT AND PERSISTENCE

By

Poulomi Sadhukhan

INSTITUTE OF PHYSICS, BHUBANESWAR.

A thesis submitted to the
Board of Studies in Physical Sciences

In partial fulfillment of the requirements

For the Degree of

DOCTOR OF PHILOSOPHY

of

HOMI BHABHA NATIONAL INSTITUTE



December 25, 2012.

Homi Bhabha National Institute

Recommendations of the Viva Voce Board

As members of the Viva Voce Board, we recommend that the dissertation prepared by **Poulomi Sadhukhan** entitled “On phases of DNA, entanglement and persistence” may be accepted as fulfilling the dissertation requirement for the Degree of Doctor of Philosophy.

----- **Date :**
Chairman : Chairman of committee

----- **Date :**
Convener : Convener of Committee

----- **Date :**
Member : Member 1 of committee

----- **Date :**
Member : Member 2 of committee

----- **Date :**
Member : Member 3 of committee

Final approval and acceptance of this dissertation is contingent upon the candidate’s submission of the final copies of the dissertation to HBNI.

I hereby certify that I have read this dissertation prepared under my direction and recommend that it may be accepted as fulfilling the dissertation requirement.

----- **Date :**
Guide : Prof. Somendra Mohan Bhattacharjee

DECLARATION

I, hereby declare that the investigation presented in the thesis has been carried out by me. The work is original and the work has not been submitted earlier as a whole or in part for a degree/diploma at this or any other Institution or University.

Poulomi Sadhukhan

To my father

ACKNOWLEDGEMENTS

Completion of this thesis was possible with the support of several people. I would like to express my sincere gratitude to all of them.

First of all, I am extremely grateful to my supervisor, Prof. Somendra Mohan Bhattacharjee, whose profound impact deserves special acknowledgement.

I would like to thank Prof. Sanjay Kumar and Prof. Goutam Tripathy for useful discussions, especially in connection with the work reported in this thesis. I express my gratitude to all of my teachers who helped me in understanding the subject.

This is a time to acknowledge the useful interactions with Jaya Maji, Garima Mishra and Tanmoy Pal as coauthors of some of my papers. I also thank the scholars and post-docs of IOP for various discussions and making my stay at IOP memorable.

I want to express my heartfelt gratitude and indebtedness to my friends and family for their support in every possible way.

Synopsis

In this thesis we study non-equilibrium stochastic paths, especially in the context of the binding-unbinding transition of polymers and DNA. The phases and the phase transition of DNA being the main attraction, we study the same under a force for both equilibrium and non-equilibrium cases. In course, we study an even simpler two-state system, the Ising ferromagnet, to obtain similar results. The results of a DNA system often show similarities to other systems. For example, the phase diagram resembles that of superconductors, an imaginary time transformation makes the polymer problem equivalent to a quantum problem, thereby, and, the reunion exponents and the order of phase transition are shown to be recovered from the equivalent quantum problem by studying the quantum entanglement. Such connections to other topics, which are apparently or mechanism-wise different, are explored.

We start with the equilibrium phase transition of a double-stranded DNA (dsDNA) under a force. A dsDNA is a two-stranded long double helical molecule. During many biological processes like replication, transcription, etc., the two strands of the dsDNA are needed to be opened up partially or fully. In order to make this possible, a few proteins, like helicases, sit at the junction of the two strands and exert a force on the strands. When the strands are pulled in opposite directions by a force, the two strands get separated if the applied force exceeds a critical value. This unzipping transition is first-order below a critical temperature. At this critical temperature, the dsDNA melts to a pair of single stranded DNA (ssDNA), even in the absence of any external force on the strands, and this melting transition is second-order. This phase transition is studied by different methods starting from renormalization group studies to various experiments looking at the phases. Among the theoretical studies, the most common is modeling a dsDNA as two interacting polymers.

In the first chapter, we show that a thermodynamic study can produce the features of the zipping-unzipping phase diagram of a dsDNA. We look at the interface between the zipped and the unzipped phases and classify the existing DNAs into two types in terms of the sign of the interface energy. Most of the present theoretical models ignore the helical structure to simplify the model. Our study shows that considering the helical order along with the external force under

certain circumstances can even make the unzipping transition second order, which has experimental evidence in a topology-preserved phase transition. The crucial role is played by the competition between two independent length scales induced by the helical order and the external force. This fact along with the phase diagram of a DNA matches with that of superconductors. This tempts us to name the two classes as Type I and Type II.

In reality, the essential unbinding proteins like helicases get energy from periodic ATP consumption, thus producing a periodic force on the strands of the DNA. Motivated by this, in the second chapter, we study a DNA hairpin under a periodic force. The analogous two-state Ising magnet shows a similar behaviour under a periodic magnetic field, though the detailed dynamics are different in these two systems. For an Ising ferromagnet under a magnetic field, there is a first order phase transition from a positively magnetized state to a negatively magnetized state. Under a periodic force, near the phase transition, the mismatch between the time scales of the applied field and the relaxation time of the system gives rise to a forward and a backward branches to yield a magnetization vs. magnetic field loop. This is called hysteresis. In hysteresis, usually a loop averaged over many cycles receives attention. But we find that this averaging suppresses the actual picture of the states. In this work, we quantify the phases by looking at the time-resolved loops and propose a dynamical phase diagram. This diagram is qualitatively similar to that obtained from a periodically driven DNA hairpin. The importance of this dynamical phase diagram, apart from the usual one, is that it shows the possibility of going from one phase to the other just by varying frequency alone, keeping the amplitude of the external drive fixed.

In the third chapter, we concentrate on the hysteresis of the Ising ferromagnet. Here aim is to extract the equilibrium discontinuous phase transition curve in the magnetization vs. magnetic field plane, which, in a real situation is impossible to get, no matter how long we allow the system to equilibrate. In achieve our goal, we utilize the work theorem and the histogram method. The work theorem relates the equilibrium free energy difference between any two states to the non-equilibrium work done in going from one state to the other. The histogram technique is widely used in simulation which extrapolates the equilibrium distribution given at some parameter value to that of another. We show that the work theorem can be obtained from the histogram transformation. Then we generalize the work theorem

to an arbitrary number of intensive parameters including the temperature, and express the equilibrium distribution as the principal eigenvector of a specially constructed matrix consisting of the non-equilibrium measurements of the work done. Using this weighted averaging, one can get a much better phase transition curve which can not be obtained using a simple averaging.

Next we look at the quantum problem equivalent to the polymer unbinding transition. A classical path connecting two points in the configuration space can be equivalently thought of as a trajectory in a quantum problem under the imaginary time transformation. Then the partition function in the classical problem maps on to Green's function in the quantum problem, the sum over all configurations represents the sum over all trajectories in quantum case, and so on. This equivalence maps the classical problem of two interacting polymers onto the quantum problem of two particles. Then our interest is in the unbinding transition of a pair of bound quantum particles. This depicts a quantum phase transition (QPT), governed by quantum fluctuations. To observe the signature of the QPT, one important quantity is the quantum entanglement entropy, the most common of which is the von Neumann entropy. The quantum entanglement entropy quantifies the pure quantum correlation in the system. For both the short-range and long-range potentials, we compute the von Neumann entropy and find that near the QPT, it diverges negatively. We discuss the behaviour of the entropy and its connection to the reunion exponents in the fourth chapter.

Viewed as a stochastic path, a polymer can be interpreted as a classical random walker with length of the polymer as time. A study of the paths of such a random walker is the topic of the fifth chapter. The classical walker is associated with a power law distribution of the hopping rates. The mean squared displacement and the persistence probability, the probability that a walker does not return to its starting point upto time t , are observed. We show that the quenched and the annealed averaging with the site and the bond disorders give different persistence behaviours, though all have the same behaviour for the mean squared displacement.

To summarize, our focus is to study paths, mostly in the form of polymers, and the phases of DNA, both in equilibrium and non-equilibrium. In the first part, the DNA phases are observed under pulling force at one end. Both static and periodic forces are discussed, with the corresponding phase diagrams. The results are then compared from a much simpler system of an Ising magnet, and for this case

we even go further by utilizing variants of the work theorem. The mapping to the equivalent quantum problem of interacting particles led us to look at the unbinding transition through the quantum entanglement entropy. Several interesting features of the entanglement entropy, as an entropy by itself, is discussed along with its connection to the reunion exponents of two interacting polymers. The last part is a study on the behaviour of return to the origin of a random walker in a random medium, a problem synonymous to loop formation in polymers. This thesis gives new insights about polymers and DNA problems as these are looked from new angles, e.g. by looking at time-resolved states, by exploring the connections to other systems like superconductors and quantum problems, thus bringing out the vastness and the universal nature of the polymer problems.

List of Publications/Preprints

1. Thermodynamics as a nonequilibrium path integral; Poulomi Sadhukhan and Somendra M. Bhattacharjee, *J. Phys. A: Math. Theor.* 43 (2010) 245001. (arXiv:0911.2874)
2. TYPE II DNA: when the interfacial energy becomes negative; Poulomi Sadhukhan, Jaya Maji and Somendra M. Bhattacharjee, *Europhys. Lett.* 95 (2011) 48009. (arXiv:1009.1021)
3. Entanglement entropy of a quantum unbinding transition and entropy of DNA; Poulomi Sa8dhukhan and Somendra M. Bhattacharjee, *Europhys. Lett.* 98 (2012) 10008. (arXiv:1110.2131)
4. Dynamical phase transition of a periodically driven DNA; Garima Mishra, Poulomi Sadhukhan, Somendra M Bhattacharjee, Sanjay Kumar. Submitted to journal. (arXiv:1204.2913)
5. Signature of special behaviors of $1/r^2$ interaction in the quantum entanglement entropy; Poulomi Sadhukhan and Somendra M. Bhattacharjee, *J. Phys. A: Math. Theor.* 45 (2012) 425302. (arxiv:1207.2755)
6. ¹Renormalization group limit cycle for three-stranded DNA; Tanmoy Pal, Poulomi Sadhukhan and Somendra M. Bhattacharjee, *Phys. Rev. Lett.* 109, (2012) 26. (arXiv:1208.3359).
7. Renyi entropy of two quantum particles interacting via $1/r^2$ potential, Poulomi Sadhukhan, Somendra M Bhattacharjee (Under preparation).
8. Persistence of a Brownian walker in disordered media with power law distribution of hopping rates; Poulomi Sadhukhan and Goutam Tripathy (Under preparation).

¹Not included in this thesis

Contents

1	Introduction	1
1.1	DNA	1
1.1.1	Phase transition of DNA	2
1.1.2	Interacting polymers	7
1.1.3	Path integral correspondence	10
1.2	Connection of equilibrium and nonequilibrium measurements	12
1.2.1	Work theorem	12
1.2.2	Histogram method	16
1.3	An equivalent quantum system: two interacting particles and quantum phase transition	19
1.3.1	What is quantum entanglement?	20
1.3.2	Quantification of entanglement	22
1.4	Random walk in disordered media	24
1.4.1	Persistence probability $P(t)$	24
1.4.2	Diffusion in disordered media	25
1.4.3	Modeling disordered media	26
1.4.4	Anomalous diffusion due to broad waiting time distributions	27
1.5	Organization	28
2	TYPE II DNA: when the interfacial energy becomes negative	31
2.1	Introduction	31
2.1.1	Outline	33
2.2	Theory and results	33
2.2.1	Thermodynamics	33
2.2.2	Surface energy	35
2.3	Discussion	40
2.4	Summary	42
3	Dynamical phase transition of a driven Ising magnet	44
3.1	Introduction	44
3.1.1	Outline	46
3.2	Driven DNA and results	46

3.3	Magnetic model and method	49
3.3.1	Model	49
3.3.2	Procedure	49
3.4	Numerical results	51
3.4.1	Dynamical phase diagram	52
3.5	Summary	56
4	Equilibrium probability distribution from nonequilibrium path integral	58
4.1	Introduction	58
4.1.1	Outline	59
4.2	Work theorem and path integral	60
4.2.1	Work theorem	60
4.2.2	Paths: equilibrium and nonequilibrium	61
4.2.3	Histogram transformation and infinitely fast process	62
4.2.4	Work theorem and histogram method	63
4.3	Equilibrium probability distribution	65
4.3.1	Generalization	68
4.3.2	Application to ferromagnet to get equilibrium magnetization curve	69
4.4	Equilibrium probability distribution from an eigenvalue equation: Operator \mathcal{S}	69
4.4.1	Examples	72
4.5	Numerical verification of results	74
4.5.1	Numerical verification of the equilibrium probability distribution starting from a uniform distribution	75
4.5.2	Equilibrium magnetization curve using nonequilibrium path integral	77
4.5.3	Numerical verification of the eigenvalue equation	77
4.6	Summary	78
5	Entanglement entropy of a quantum unbinding transition and entropy of DNA	81
5.1	Introduction	81

5.1.1	Outline	82
5.2	Entanglement entropy	82
5.3	DNA connection	90
5.4	Discussion	93
6	Quantum unbinding transition for a long range potential	96
6.1	Introduction	97
6.1.1	Outline	100
6.2	Model and method	100
6.3	Analytical results	101
6.4	Exact numerical results	105
6.4.1	Protocol	105
6.4.2	Behavior of the von Neumann entropy S^{vN}	106
6.4.3	Behaviour of the Renyi entropy	110
6.5	Discussion and conclusion	114
7	Random walks in disordered media	119
7.1	Lattice models and simulations	120
7.1.1	Relevance to real systems	121
7.2	Numerical results	122
7.2.1	Mean square displacement $\langle x^2(t) \rangle$	122
7.2.2	Waiting time distribution $\omega(\tau)$	122
7.2.3	Two point incremental correlation function $C(t_1, t_2)$	124
7.2.4	Persistence probability	125
7.2.5	Explanation of the observed $P(t)$	126
7.3	Summary and concluding remarks	131
8	Summary	133

List of Figures

1.1	Phase diagram of the force induced unzipping transition. Here $g_c(T)$ is the critical force for unzipping and T_c is the critical temperature for melting when no force is applied.	3
1.2	An oriented square lattice. Two polymers (red lines) starts from $r = 0$ and moves along the bonds connecting two crossing points without crossing each other in upward direction. An external force g is applied at one end.	5
1.3	A necklace of bubble (B), of length n_B , and bound (A), of length n_A segments.	7
1.4	Paths connecting an initial equilibrium state having an external parameter value λ_A to a final nonequilibrium state having a parameter value λ_B . The final state is reached in a time τ	14
1.5	A comparison of the work done between a 1-step process and an n -step process. For large n , the work distribution shows a peak at W_{eq}	15
2.1	Schematic representation of two configurations, fully zipped (above) and a configuration of coexisting phases separated by an interface (below) at $g = g_c$. The difference in the free energies of this two configuration gives the interfacial energy.	35
2.2	Schematic diagram of variation of zipping-unzipping order parameter ψ (continuous line) and applied force g (dashed line) inside unzipped and zipped phases. ξ is the length scale of variation of ψ inside the zipped phase and λ is the scale for g . For Type I (left figure), $\kappa = \lambda/\xi \ll 1$ and for Type II (right figure), $\kappa \gg 1$	37
2.3	(a) Schematic diagram of the variation of the force and the helical order inside the zipped phase for $\xi \gg \lambda$ (left figure), resulting in a positive surface energy. (b) The figure shows the ideal situation of $\xi \gg \lambda$	38

2.4	(a) Schematic diagram of the variation of the force and the helical order inside the zipped phase for $\xi \ll \lambda$ (left figure), resulting in a negative surface energy. (b) The figure shows the ideal situation when $\xi \ll \lambda$	40
2.5	Schematic diagram of a periodic array of defect blobs. The array has a periodicity d which controls the density of blobs. Each distorted region is of length $\sim \lambda$ with an unzipped core of size $\sim \xi$	41
3.1	A DNA hairpin of total length $P = 32$ in (a) a zipped (Z) and (b) an unzipped (U) state. The stem (solid lines) of length $p = 10$ consists of complementary nucleotides with native interaction (dotted lines) for base pairing, whereas the loop (dashed line) is made up of non-complementary nucleotides.	46
3.2	DNA hysteresis for different g_m and ν as indicated. Each plot contains the loops for 10 different initial conformations. These are at $T = 0.10$, for which $g_c \sim 0.20$ (see Ref. [72]).	48
3.3	One cycle of magnetic field with time.	50
3.4	Plot shows the time sequence of Q with cycles ($h_m = 0.6$, $\nu = 1/70$). Three bands indicate that the states with different Q values occur randomly.	52
3.5	The distribution of Q is plotted for three different frequencies and same set of h_m . For a frequency, the distribution $P(Q)$ shifts as h_m increases. It goes from Z-state to U-state through D-state. The corresponding states/phases in Q are identified observing the distribution. (a) frequency $\nu = 1/70$. Phases: $Z \rightarrow Z+D \rightarrow Z+D+U \rightarrow D+U \rightarrow U$. (b) frequency $\nu = 1/250$. Phases: $Z \rightarrow Z+D \rightarrow D \rightarrow D+U \rightarrow U$ (c) frequency $\nu = 1/1000$. Phases: $Z \rightarrow Z+D \rightarrow D \rightarrow U$. 53	53
3.6	Dynamical phase diagram of a periodically driven Ising ferromagnet in the h_m - ν plane. The lines are boundaries for various phases U, D and Z. Here Z corresponds to the negatively magnetized state, U corresponds to the positively magnetized state and D is the dynamical state. The points are from the simulation and the lines are guide to eye.	54

3.7	Dynamical phase diagram of a periodically driven DNA hairpin in the g_m - ν plane. The lines are boundaries for various phases U, D and Z. The points are from the simulation and the lines are guide to eye (see Ref. [72]).	56
4.1	Schematic representation of two replicas of same paths, each starting from $\Lambda = 0$ and ending at $\Lambda = \lambda$ in replica 1 and at $\Lambda = \lambda - \delta$ in replica 2. Label i denotes the step number as Λ is changed in steps of λ/n . Lines of different styles (dashed, dotted etc) represent different realizations of paths starting from different values of x . The vertical portion of a path is an instantaneous process (no change in x) and the horizontal part is under interaction with the surrounding (x evolves at a constant Λ). Identically shaded lines in the two replicas have the same evolution.	66
4.2	Plot of the weighted distribution (a) $P_{J,h}(E)$ vs. E and (b) $P_{J,h}(M)$ vs. M (dotted line with circles) for varying J and h with $n = 20$ and equilibrium distributions $P_{eq}(E)$ and $P_{eq}(M)$ (crosses) with $J = 1$, $h = 1$ and $\beta = 0.2$ for a 8×8 lattice, showing that $P_{J,h}(E) = P_{eq}(E)$ and $P_{J,h}(M) = P_{eq}(M)$	76
4.3	Plot of weighted average $M(h)$ vs. h and the corresponding hysteresis loop (simple averaged M vs. h) for a 8×8 lattice. The magnetic field varies from $-h_0$ to $+h_0$ in 100 steps. (a) $h_0 = 0.1$. The weighted loop and the hysteresis loops are represented by the black solid line and the green and blue dashed lines. The inset shows the hysteresis loop for the small (green and blues lines) field with respect to the large field (red double dash-dotted line) and the weight averaged magnetization for small field. (b) $h_0 = 2$. The weighted loop and the hysteresis loops are represented by the dashed lines and the red solid line respectively.	78
4.4	Plot of the equilibrium distribution $P_{eq}(M)$ vs. M (boxes with dotted line) and normalized principal eigen-vector $P_h(M)$ (dashed line with circles) with $J = 1$, $h = 1$, $\beta = 0.2$ and $n = 1000$ for (a) 4×4 lattice and (b) 8×8 lattice, showing that $P_h(M) = P_{eq}(M)$, i.e., eigenfunction is indeed an equilibrium distribution.	79

- 5.1 (a) Gap Δ in the energy spectrum. The shaded region is the continuum of energy. (b) The graph shows how energy gap goes to zero. The continuous line describes a second order or continuous transition (critical) and the dashed line shows the first order transition. The two are distinguished by the behaviour of the slope at $u = u_c$ 83
- 5.2 Path integral representation in the $x-t$ plane. (a) A relative coordinate path for two particles in one-dimension. The solid portions represent the classical bound state, i.e., inside the well (B), and the dashed portions represent the unbound (U) state in the classically forbidden region. (b) Corresponding path representation of two quantum particles with time, though intersections of paths are not shown explicitly. It is also a configuration of two classical Gaussian polymers interacting at the same contour length as for DNA base pairing, the t -axis representing the contour length (z) of the polymers. The dotted lines are the melted bubbles whose partition functions are characterized by the reunion exponent Ψ . This description holds for any general d 85
- 5.3 Plot of S^{vN} vs. $\ln \kappa$ with $a = 1$. The circles are the numerical values and the straight line is the predicted line $S^{vN} = 3 \ln \kappa + 7.06$, Eq.(5.22). 89
- 6.1 g vs. u phase diagram. The plot shows the phases and the RG fixed points in the $g-u$ plane ($u = -V_0 a^2$). The red curve below $g = 1/4$ and $u = -0.5$ show the binding-unbinding transitions governed by a line of unstable real fixed points. The transition is first order for $g < -3/4$ and second order for $-3/4 < g < 1/4$. This line is the transition line in the limit of zero range potential ($a \rightarrow 0, V_0 \rightarrow \infty$, with $u = \text{constant}$) The black continuous curve for $u > -0.5$ shows the locus of stable fixed points representing the unbound phase. The dashed-dotted line at $g = 1/4$ is the boundary beyond which the fixed points are complex. 99

6.2	S^{vN} vs. λ for various κ . In the plot $S = S^{vN} + 8 \ln \frac{2}{\pi}$. The plot shows that the entropy diverges for $\lambda \leq 0$ as $\kappa \rightarrow 0$. The dashed line marked as $\kappa \rightarrow 0$ is the expected behavior of the entropy for $\lambda > 1$	106
6.3	S^{vN} vs. $\ln \kappa$ for various λ . Here, as in Fig. 6.2, $S = S^{vN} + 8 \ln \frac{2}{\pi}$. For comparison, $3 \ln \kappa$ and $\frac{3}{2} \ln \kappa$ are shown by black lines with the symbols $+$ and \times . The inset shows that the entropy is κ -independent for $\lambda > 1$	107
6.4	The plot of c_λ vs. λ , showing a divergence at $\lambda = 1$	108
6.5	Data collapse: $(S_\lambda^{vN} - S_1^{vN}) / \frac{3}{2} \ln \kappa$ vs $(1 - \lambda) \ln \kappa$	109
6.6	Renyi entropy: plot of S_n against λ for various n	110
6.7	$S_{n,\lambda}$ vs. $\log \kappa$ for (a) $\lambda < 1$ and (b) $\lambda = 1$. For the both, $S_{n,\lambda}$ is linear in $\log \kappa$. For (a), slope is 3 and for (b) slope varies with n . . .	111
6.8	$S_{n,\lambda}$ vs. $\ln \kappa$ for $\lambda > 1$, for (a) $n = 1.025$ and (b) $n = 1.400$. $S_{n,\lambda}$ is independent of λ below some n_c	112
6.9	The plots show (a) $c_{n,\lambda}$ vs. n , and (b) $f_1(n)$ (coefficient of $\ln \kappa$, see Eq.(6.33)) vs. n , both for $\lambda = 1$	112
6.10	Plot of S_n vs. n for different λ values, (a) $\lambda < 1$, (b) $\lambda = 1$ and (c) $\lambda > 1$. For (a) and (c), $\kappa = 10^{-10}$, while for (b) $\kappa = 10^{-13}$ and $\kappa = 10^{-14}$	113
6.11	(a) The plot shows $f_\lambda(n)$ vs. n (coefficient of $\ln \kappa$, see Eq.(6.33)). It shows the existence of a special value of n , below which the Renyi entropy S_n is independent of κ . (b) The variation of n_c with λ . . .	114
6.12	The path dependence of entropy. Two different limits of approaching $\{\lambda = 1, \kappa \rightarrow 0\}$. (a) First $\kappa \rightarrow 0$ and then $\lambda = 1$ (red line). The entropy diverges like $1/(1 - \lambda)$. (b) First $\lambda \rightarrow 1$ and then $\kappa \rightarrow 0$ (blue line). The entropy diverges like $\ln \kappa$ Thick line along x -axis for $\lambda \leq 1$ denotes divergent entropy. (c) For $\lambda < 1$, taking the limit $\kappa \rightarrow 0$ (black vertical line with arrow) leads to divergent entropy and S^{vN} remains so along the horizontal stretch.	115
7.1	The bond disorder or random barrier model. In this model the hopping rate $W_{i,i-1} = W_{i-1,i}$	120

7.2	The site disorder or random trap model. In this model the hopping rate $W_{i,i-1} = W_{i,i+1}$	121
7.3	The waiting time distribution $\omega(\tau)$ vs. τ for (a) annealed site disorder and (b) annealed bond disorder for different α	123
7.4	The waiting time distribution $\omega(\tau)$ vs. τ for (a) quenched site disorder and (b) quenched bond disorder for different α	123
7.5	(a) Plot of $C(t_1, t_2)$ vs. $ t_1 - t_2 $ for quenched bond disorder. Here H denotes the Hurst exponent. (b) Plot of $C(t_1, t_2)$ vs. t_1 for quenched site disorder. Here t_2 is kept fixed and region of interest in $t_1 \gg t_2$	124
7.6	Persistence probability $P(t)$ vs. t for (a) annealed site disorder and (b) annealed bond disorder for different α	126
7.7	Persistence probability $P(t)$ vs. t for (a) quenched site disorder and (b) quenched bond disorder for different α	126
7.8	Persistence exponent θ vs. α for different models of disorder.	128
7.9	The survival probability for the quenched bond disorder. (a) The plot shows the survival probability with time in log-log plot. (b) This is the plot of the survival exponent γ for different α . Here, x -axis is the value of α and the y -axis is the survival exponent γ . The red curve shows the variation of β with α	130

1

Introduction

Among all disciplines in physics, statistical physics occupies a privileged position as the natural framework to understand the behaviour of the biological systems at the molecular level by using the concepts of stochasticity, fluctuations, metastability and thermal activation. In this thesis, we discuss some biological phenomena that occur inside living cells. Our main focus is to study the phases and the phase transition of DNA. The behaviour of DNA is found to have very nice similarities with other non-biological systems like superconductors. It finds applicability in much wider general topics like random walks. The behaviour of the complex structure of DNA under certain circumstances resembles that of a much simpler system like a two-state Ising spin system. These connections are explored in this thesis along with some results of relevance in biology, obtained for DNA and polymers by using thermodynamic and statistical tools of Physics.

1.1 DNA

DNA (Deoxyribonucleic acid) is an essential molecule that encodes the genetic instructions used in the development of living organisms. Genetic information is encoded as a sequence of four types of nucleotides: Guanine (G), Adenine(A), Thymine(T), and Cytosine(C). Most DNA molecules are double-stranded helices, consisting of two long polymers of simple units called nucleotides. This arrangement of two nucleotides binding together across the double helix is called a base pair. This binding is created by hydrogen bonds, which can be broken and re-joined. The two strands of a DNA in a double helix can therefore be pulled apart

into two single stranded DNA (ssDNA) either by a mechanical force or at high temperature. These are called unzipping phase transition and melting of DNA.

1.1.1 Phase transition of DNA

The phase transition can happen by various means like (i) temperature induced melting or denaturation, (ii) force induced unzipping, or (iii) pH induced unzipping or chemical unzipping.

Force induced unzipping:

The theoretical models for the separation of a double stranded DNA (dsDNA) are based on a simple extension of the Poland Scheraga model [1], in which the two DNA strands are homogeneous ideal polymer chains interacting with each other only at the same contour length. A constant force applied at one end pulls apart the two strands of the DNA. Consider two polymers each of length N under the influence of an applied pulling force g at one end ($z = N$). The Hamiltonian of dsDNA in the continuum can be written as [2],

$$H = \int_0^N dz \left[\frac{1}{2}K \left(\frac{d\mathbf{r}_1}{dz} \right)^2 + \frac{1}{2}K \left(\frac{d\mathbf{r}_2}{dz} \right)^2 + V(\mathbf{r}_1(z), \mathbf{r}_2(z)) \right] - \int_0^N dz \mathbf{g} \cdot \left(\frac{\partial \mathbf{r}}{\partial z} \right), \quad (1.1)$$

where $\mathbf{r}_i(z)$ is the d -dimensional position vector of a monomer at a length z along the contour of the i th strand, $V(\mathbf{r}_1, \mathbf{r}_2)$ is the binding potential, and $\mathbf{r}(z) = \mathbf{r}_1(z) - \mathbf{r}_2(z)$ is the relative coordinate. The dsDNA unzips to two single strands if the pulling force exceeds a critical value g_c [2]. This unzipping is a first order phase transition as the separation between the strands increases discontinuously as g approaches g_c . The unzipping of dsDNA can be studied in two ensembles.

- *Fixed force ensemble:* A constant pulling force g is applied on the DNA. The relevant free energy is the Gibbs free energy $G(T, g)$.
- *Fixed distance ensemble:* The separation x between the strands is kept constant. The relevant free energy is the Helmholtz free energy $F(T, x)$.

The phase diagram in the force(g)-temperature(T) plane contains two phases, namely the *zipped* phase, in which the DNA is a double stranded chain, and the

unzipped phase, in which the strands of the DNA get separated from each other. It is known that a dsDNA can be converted to two single strands by increasing the temperature to 80C-100C. Unzipping is an initial step in biological processes like DNA replication and RNA transcription which requires the aid of some enzymes like helicases, polymerases etc. However, to account for the unzipping in the cellular medium, where it takes place at physiological conditions 37C and at neutral pH, one needs to consider the unzipping by force which comes from the mechanical force exerted on the dsDNA by the enzymes to open it up.

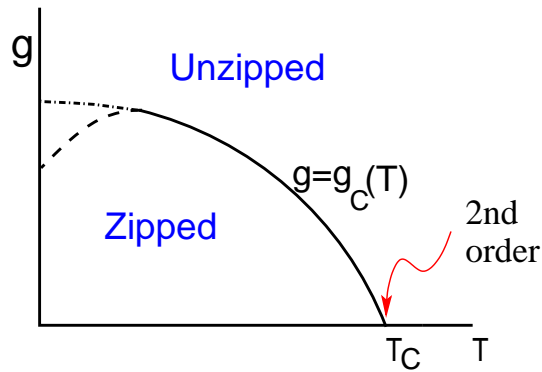


Figure 1.1: Phase diagram of the force induced unzipping transition. Here $g_c(T)$ is the critical force for unzipping and T_c is the critical temperature for melting when no force is applied.

Fig. 1.1 shows the phase diagram of DNA unzipping by a force in the force-temperature plane. The line $g_c(T)$ separates the two phases. Here g_c is the critical force required for unzipping and is dependent on temperature. To get a force-induced transition one must stay below a critical temperature T_c , which is the melting temperature when no force is applied. DNA in its double helical form shows a resilience against an external pulling force. The bound state does not allow a force g applied at an end to penetrate up to a critical force $g = g_c$, above which the DNA gets unzipped [2, 3, 4, 5, 6, 7]. The transition is first order for temperatures $T < T_c$ where T_c is the denaturation(melting) temperature in the absence of any force [8]. In some models there happens a re-entrance phenomenon, as shown by the dashed line in Fig. 1.1, where at low temperatures, the critical force decreases with the temperature. The re-entrance is due to the low temperature entropy of the double stranded DNA.

Temperature induced melting:

When a solution of DNA is heated above some temperature, the dsDNA gets denatured. The melting starts at the ends of the DNA, and at region which is rich in AT. This subsequently destabilizes adjacent regions of helix, leading to a progressive melting of the whole structure at a well defined temperature known as the melting temperature (T_m). The thermal denaturation of DNA is reversible. When the heated solutions of denatured DNA are slowly cooled, single strands often meet their complementary strands and reform regular double helix. The DNA denaturation has been studied extensively by various models which are mainly based on the Poland Scheraga model [1], or on the Peyrard Bishop model [9]. All these models agree that the thermal denaturation of the DNA is a phase transition, but the order of the transition depends on the model used. Some models [10, 11, 1, 12, 9] show it is a continuous transition while others [10, 13, 14] show it is discontinuous. Ref. [15] reviews on thermal denaturation of DNA.

Chemical denaturation:

The dsDNA also denatures by extreme pH conditions. The unzipping by using chemical agents in neutral pH is known as chemical denaturation [16]. The pH of melting depends on the mole fraction of GC pairs on the DNA. Larger the mole fraction of GC pairs, the higher the pH of melting. The denaturation of DNA at neutral pH is caused by a number of chemical agents, such as urea and formamide, by disrupting the hydrophobic forces between the stacked bases.

Exact solution of the DNA unzipping problem

Let us consider a dsDNA as two directed polymers on a $1 + 1$ dimensional square lattice. It starts walking from the origin ($z = 0$). Two polymers are not allowed to cross each other. The base pairing is put in by considering a contact energy $-\epsilon_b$ ($\epsilon_b > 0$) for each contact when separation (x) between the two strands is zero. One end of the DNA is anchored and the force is applied at the other end. Fig. 1.2 shows a schematic picture.

Let $d_t(x)$ be the partition function in the fixed distance ensemble. Then one

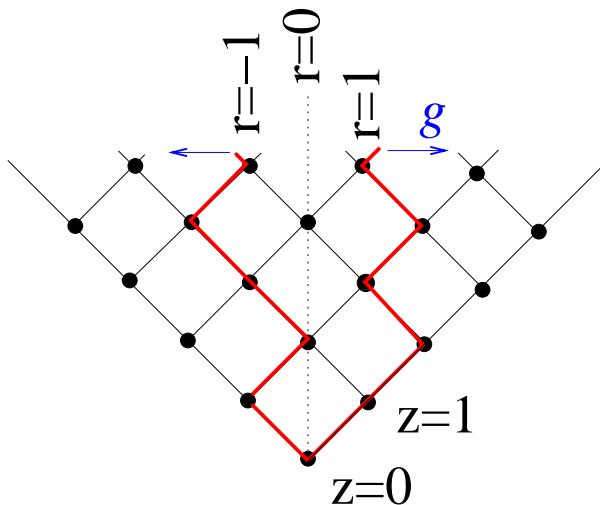


Figure 1.2: An oriented square lattice. Two polymers (red lines) starts from $r = 0$ and moves along the bonds connecting two crossing points without crossing each other in upward direction. An external force g is applied at one end.

can write the recursion relation as,

$$d_{t+1}(x) = [d_t(x+1) + 2d_t(x) + d_t(x-1)] [1 + (e^{\beta\epsilon_b} - 1) \delta_{x,0}], \quad (1.2)$$

where β is the inverse temperature. As an initial condition of polymers held fixed and joined at one end, one has, $d_0(x) = e^{\beta\epsilon_b} \delta_{x,0}$. To solve, one can take a generating function for the partition function as,

$$\bar{d}(z, x) = \sum_t z^t d_t(x) = \lambda^x(z) A(z), \quad (1.3)$$

where λ and A are to be determined. Using this ansatz, one gets,

$$\lambda = \frac{1 - 2z - \sqrt{1 - 4z}}{2z}, \quad (1.4)$$

and

$$A = \frac{1}{1 - z(2 + \lambda)e^{\beta\epsilon_b}}. \quad (1.5)$$

The singularities of the generating functions are then,

$$z_1 = 1/4, \quad (1.6)$$

and

$$z_2 = \sqrt{1 - e^{-\beta\epsilon_b}} - 1 + e^{-\beta\epsilon_b}. \quad (1.7)$$

The zero force melting takes place when $z_1 = z_2$, i.e. at $T_c = 1/\ln(4/3)$.

Fixed force ensemble: In the fixed force ensemble, the generating function is written as,

$$\mathcal{D}(z, \beta, g) = \sum_x e^{\beta g x} \sum_t z^t d_t(x) = \sum_x e^{\beta g x} \lambda^x(z) A(z) = \frac{A(z)}{1 - \lambda(z)e^{\beta g}}, \quad (1.8)$$

which has the g -dependent singularity at

$$z_3 = \frac{1}{2 + 2 \cosh \beta g}. \quad (1.9)$$

Note here that Eqs.(1.6), (1.7) and (1.9), correspond to the free energies of the unzipped state at zero force, of the zipped state which is independent of force, and of the unzipped but stretched (by g) state, respectively. More explicitly, the free energies per monomer are,

$$G_u(T, 0) = \frac{1}{\beta} \ln z_1 = -\frac{1}{\beta} \ln 4, \quad (1.10)$$

$$G_z(T, g) = \frac{1}{\beta} \ln z_2 = \frac{1}{\beta} \ln \sqrt{1 - e^{-\beta\epsilon_b}} + 1 - e^{-\beta\epsilon_b}, \quad (1.11)$$

$$G_u(T, g) = \frac{1}{\beta} \ln z_3 = -\frac{1}{\beta} \ln 2 - \frac{1}{\beta} \ln(1 + \cosh g), \quad (1.12)$$

which will be mentioned in Chapter 2. Here the subscripts u and z refer to the unzipped and the zipped phases respectively.

1.1.2 Interacting polymers

Necklace model

The necklace model captures the features of the phase transition of interacting polymers in any dimensions [17] provided the configurations have predominantly a one-dimensional structure, though they may spread in transverse directions indefinitely.

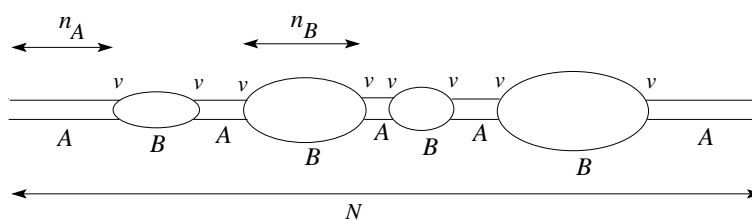


Figure 1.3: A necklace of bubble (B), of length n_B , and bound (A), of length n_A segments.

Any configuration of this model consists of alternating segments of microstates labeled A, consisting of a bound part of length n_A , and B, consisting of an open part or bubble of length n_B (see Fig. 1.3). The free energy per unit length of the whole configuration is $f(T)$, at temperature T , where

$$\beta f(T) = - \lim_{N \rightarrow \infty} \frac{1}{N} \ln Z_N(T), \quad (1.13)$$

with Z_N as the partition function. To calculate the free energy it is convenient to consider a generating function,

$$G(z, T) = \sum_{N=0}^{\infty} z^N Z_N(T). \quad (1.14)$$

If z_0 is the singularity of $G(z)$ closest to the origin of the complex z -plane, then the limiting free energy would be,

$$\beta f(T) = \ln z_0(T). \quad (1.15)$$

In a similar way, the generating functions for the A state and the B state can be

constructed,

$$G_A(z) = \sum_n Q_n^A z^n, \quad G_B(z) = \sum_n Q_n^B z^n, \quad (1.16)$$

where Q^A and Q^B are corresponding canonical partition functions. Often the bubble partition function Q_n^B is taken as

$$Q_n^B \approx e^{-n\sigma_0}/n^\Psi, \quad (1.17)$$

with σ_0 as the bubble entropy per monomer and Ψ as the reunion exponent (discussed in the next subsection).

Now if a Boltzmann factor v is associated for the junctions AB or BA, and one puts the condition that the polymers start and end with configuration A, then $G(z)$ can be written as,

$$G(z) = G_A(z) / [1 - v^2 G_A(z) G_B(z)]. \quad (1.18)$$

The singularity of $G_A(z)$ and $G_B(z)$ will give the corresponding phases, but the smallest root of the equation

$$v^2 G_B(z) = 1/G_A(z), \quad (1.19)$$

will correspond to a new bound phase. A transition takes place if the necklace goes from this new state to the open B-type phase. An analysis of Eq.(1.19) shows [17] that below the transition temperature T_c , with $t = (T_c - T)/T_c$,

$$f = \sigma_0(T) - A_s t^{1/(\Psi-1)} + \dots, \quad \text{for } 1 < \Psi < 2, \quad (1.20)$$

$$f = \sigma_0(T) - A_1 t + A_s t^{\Psi-1} + \dots, \quad \text{for } \Psi > 2, \quad (1.21)$$

where Eq.(1.20) shows a critical behaviour and Eq.(1.21) has a first order transition. There is no phase transition for $\Psi < 1$ and the system remains in the bound state. Note here the change of the order of the phase transition with the value of Ψ , which will later be connected to the interaction strength of the inverse square potential in the context of quantum entanglement entropy near dissociation.

Reunion of two polymers

Let us consider two Gaussian polymers, joined at one end ($z = 0$), doing random walks. The elastic energy for each chain is given by $H = \int_0^N dz (d\mathbf{r}/dz)^2$, where \mathbf{r} is the d -dimensional vector of monomer at z . The partition function, or the total weight of all possible walks to reach \mathbf{r} , starting from $\mathbf{r} = 0$, is then,

$$Z(\mathbf{r}, 0) \approx \frac{e^{-\sigma' N} e^{-r^2/(2b^2 N)}}{(b^2 N)^{d/2}}, \quad (1.22)$$

where $e^{-\sigma' N}$ is the total partition function of all possible walks of N steps obtained by integrating $Z(\mathbf{r}, 0)$ over \mathbf{r} . Now the probability that the walker reaches \mathbf{r} after N steps is,

$$R(\mathbf{r}, 0) = \frac{Z(\mathbf{r}, 0)}{Z_{total}} \approx n^{-d/2}. \quad (1.23)$$

Then from Eq.(1.22), by putting $r = 0$, one gets the bubble partition function, that two walkers start from $r_1 = r_2 = 0$ and meet at \mathbf{r} after N steps, as the product of two individual partition functions,

$$Z_2(\mathbf{r}, 0) \approx \frac{e^{-\sigma N} e^{-r^2/N}}{N^\psi}, \quad \text{with } \psi = d, \quad (1.24)$$

where we have put $b = 1$ for brevity. The reunion exponent for meeting at particular point is denoted by ψ and reunion anywhere is denoted by Ψ . For the reunion anywhere, one has to integrate over r , in which case it becomes,

$$Z_2 = \int d^d r Z_2(\mathbf{r}, 0) \approx \frac{e^{-\sigma N}}{N^\Psi}, \quad \text{with } \Psi = d/2. \quad (1.25)$$

Hence the reunion exponents for two noninteracting Gaussian polymers are [18],

$$\psi = d \quad \text{for noninteracting walkers, reunion at a particular point,} \quad (1.26)$$

$$\Psi = d/2 \quad \text{for noninteracting walkers, reunion anywhere.} \quad (1.27)$$

In the case of interacting polymers the Hamiltonian looks like Eq.(1.31) given below. For a long range g/r^2 potential, the reunion exponent (for reunion any-

where) for two walkers are [107],

$$\Psi = 1 + \frac{\sqrt{4 + d^2 - 4d + 4g}}{2}, \quad \text{general } d, \quad (1.28)$$

$$= 1 + \frac{\sqrt{1 + 4g}}{2}, \quad \text{for } d = 3. \quad (1.29)$$

These are the exponents alluded to in the context of the necklace model discussed in the previous subsection and will also appear in the context of quantum entanglement entropy in Chapters 4 and 5.

This lays the background of our study related to the phases and phase transition of DNA and interacting polymers. At this point, we want to make a connection of classical polymers to an equivalent quantum system which will be utilized later.

1.1.3 Path integral correspondence

The correspondence between the path integral in classical statistical mechanics and the path integral in quantum mechanics is very well-known. The following example shows how the path integral formulation of quantum mechanics is related to statistical mechanics. The partition function of two classical polymers interacting via a potential V reads,

$$Z = \int \mathcal{DR} \exp[-\beta H[r_1, r_2]]. \quad (1.30)$$

Here $\int \mathcal{DR}$ denotes the integration over all possible paths or polymer configurations, and $H[r_1, r_2]$ is the energy,

$$H[r_1(z), r_2(z)] = \int_0^N dz \left[\frac{1}{2}K \left(\frac{dr_1}{dz} \right)^2 + \frac{1}{2}K \left(\frac{dr_2}{dz} \right)^2 + V(r_1, r_2) \right], \quad (1.31)$$

where K is the elastic constant of a polymer, z is the contour length along the polymer of total length N and r_i is the coordinate of the monomer of i -th polymer at length z . Then by using the imaginary time transformation, $z \rightarrow it$ one gets,

$$H[r(t)] = -i \int_0^T dt \left[\frac{1}{2}K \left(\frac{dr_1}{dt} \right)^2 + \frac{1}{2}K \left(\frac{dr_2}{dt} \right)^2 - V(r_1, r_2) \right], \quad (1.32)$$

writing $T = iN$. Identifying $\beta \rightarrow 1/\hbar$, $K \rightarrow m$ (mass) and

$$S[r_1, r_2] = \int_0^T dt \left[\frac{1}{2}m \left(\frac{dr_1}{dt} \right)^2 + \frac{1}{2}m \left(\frac{dr_2}{dt} \right)^2 - V(r_1, r_2) \right] = \int_0^T \mathcal{L} dt. \quad (1.33)$$

one gets the Green's function or the propagator of the quantum problem of two interacting particles with the classical action $S[r_1, r_2]$ with Lagrangian \mathcal{L} as,

$$\mathcal{G} = \int \mathcal{D}\mathcal{R} \exp \left[\frac{i}{\hbar} S[r_1, r_2] \right]. \quad (1.34)$$

To be noted that the Hamiltonian in the polymer problem now becomes the Lagrangian after the transformation. Here \mathcal{G} denotes the path integral over all possible trajectories in time going from one coordinate state to another. This transformation thus relates the classical statistical mechanical problem of polymers with the quantum problem where mapping are as follows: the length of the polymer maps onto the time of the quantum problem, the partition function maps onto the Green's function. Therefore, the problem of two interacting polymer becomes a quantum problem of two interacting particles. The noninteracting part, separated by a distance larger than the range of the interaction, which forms bubbles, corresponds to the excursion of quantum particles beyond the potential well. The same- z base pair interaction is the same time interaction in the quantum problem. We utilize this mapping to explain the behaviours of the quantum entanglement near the quantum dissociation of two particles with the known results of polymer unbinding transition.

To avoid any confusion, we mention that the above transformation is different from the conventional quantum to thermal mapping, where time (it/\hbar) in the quantum problem maps to the inverse temperature ($\beta = 1/k_B T$) in the classical thermal problem. The operator $\exp[-iHt/\hbar]$ in quantum mechanics then becomes $\exp[-\beta H]$, in both of which H is the corresponding Hamiltonian.

The polymer-quantum mapping has been used in our study of Chapters 4 and 5.

1.2 Connection of equilibrium and nonequilibrium measurements

Now we move our attention from the equilibrium properties to the nonequilibrium ones. For example, let us suppose one tries to observe the same system of polymers or DNA under time-dependent force, and do not allow the system to equilibrate. Obviously, the equilibrium phase diagram will not be obtained. Then the question comes whether one can get the equilibrium quantities from the nonequilibrium measurements. That one will not get it can be understood as follows. A system in thermodynamic equilibrium has no memory of its past. Consequently there is no leading role for time in the ensemble based statistical mechanics except the subservient one to maintain equilibrium among the internal degrees of freedom and with external sources. This wisdom gets exploited in the dynamics based algorithms like Monte Carlo, molecular dynamics, stochastic quantization, to attain equilibrium from any arbitrary state albeit in infinite time. Even a thermodynamic process involving changes in parameters is an infinite sequence of equilibrium states, and is therefore infinitely slow. A finite duration process, not destined to equilibrate at every instant of time, remains outside the realm of statistical mechanics and thermodynamics. A work theorem [19, 20, 21, 22, 25] attempts to bridge the gap by providing a scheme for getting the thermodynamic free energy difference from a properly weighted nonequilibrium path integral [21, 22].

1.2.1 Work theorem

The estimation of a quantity like the energy or the magnetization of a macroscopic system can be done by averaging over a reasonably large sample of microstates drawn from an equilibrium ensemble. But an estimation of the entropy or the free energy from simulations or experimental data is a tricky problem as to do that we have to necessarily consider all the microstates accessible to the equilibrium system and this number is indeed very large. There are useful Monte Carlo techniques viz., the umbrella sampling and its variants, the entropic sampling, the multicanonical sampling, the Wang-Landau algorithm, etc, that can be used for computation of the entropy and the free energy.

Consider a classical macroscopic system in thermal contact with a heat bath at

temperature T . Let λ denote a parameter that can change some degree of freedom of the system and can be controlled from outside. For example, the system can be a gas contained in a cylinder and λ can be its pressure (changing the volume) which can be controlled from outside by moving a piston; the system can be a spin lattice and the parameter can be an external magnetic field whose strength can be changed. To begin with, at time $t = 0$, let $\lambda = \lambda_1$ and let the system be in equilibrium with the heat bath. Then switch the value of λ from λ_1 to λ_2 . Also assume that the switching of λ from λ_1 to λ_2 is carried out over a time duration t .

To estimate the change in free energy let's consider two cases. One in which the switching is carried out infinitely slowly, in other words $t = \infty$, and the second one in which the switching process takes place over a finite time duration, i.e. $t < \infty$. In the first case, the system passes through equilibrium states while in the second case the system is never in equilibrium during the change. The first case corresponds to a quasi-static reversible equilibrium process so that the change in the free energy $\Delta F = F(\lambda_2) - F(\lambda_1)$ is the reversible work done on the system. In the second case, the work done will depend both on the particular microstate at the starting point and on the trajectory. The work done is defined as,

$$W = - \int_0^\tau \frac{d\lambda}{dt} \frac{\partial H}{\partial \lambda} dt, \quad (1.35)$$

where H is the Hamiltonian of the system. Therefore, for $t < \infty$, W is not unique and it is to be described by a distribution $P_t(W)$. If $\langle W \rangle$ denote the average work done on the system, then

$$\langle W \rangle = \int W P_t(W) dW.$$

In the ideal quasi-static equilibrium limit of $t \rightarrow \infty$, we have $P_{t \rightarrow \infty}(W) = \delta(W - W_R)$; W does not change from one experiment to another and it is equal to W_R , the work done in the reversible process, which also happens to be the change in the free energy.

The work theorem relates the equilibrium free energy differences to the statistics of work done on a system to reach from the initial equilibrium state to the final state through nonequilibrium paths. Consider at $t = 0$, we start from an equilibrium state of the Hamiltonian $H(x, \Lambda)$ at temperature $T = \beta^{-1}$ and $\Lambda = \lambda_A$. Now

chosen a finite time τ , it is discretized in n steps. In time τ , we reach to a final state having $\Lambda = \lambda_B$, varying Λ in small n steps, i.e., at each step Λ is increased by $\Delta\Lambda = (\lambda_B - \lambda_A)/n$. At each small step, we let the system relax for a while, but do not allow it to equilibrate. The paths connecting the initial and the final states are thus nonequilibrium paths. This process is repeated many times and

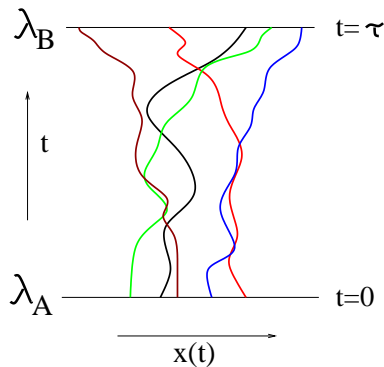


Figure 1.4: Paths connecting an initial equilibrium state having an external parameter value λ_A to a final nonequilibrium state having a parameter value λ_B . The final state is reached in a time τ .

for each path, the work done W along the path, is noted. Then according to the work theorem the equilibrium free energy difference, $\Delta F = F_{\lambda_B} - F_{\lambda_A}$, between the two states can be obtained from the nonequilibrium work done W by using the relation,

$$\Delta F = -\frac{1}{\beta} \ln \langle e^{-\beta W} \rangle. \quad (1.36)$$

Here $F_\lambda = -k_B T \ln Z_\lambda$, $Z_\lambda = \int \mathcal{D}X e^{-\beta H(x,\lambda)}$, and $\langle \dots \rangle$ denotes an average over all possible trajectories (or realizations). This relation is used in many simulations and experiments to get equilibrium free energy differences.

As already mentioned, away from equilibrium, one gets a distribution $P_n(W)$ of work along the trajectories connecting the two states. The peak of the distribution shifts with the closeness to the equilibrium [23]. For an arbitrarily slow process, one gets a sharp peak at W_{eq} . For the nonequilibrium process, there are trajectories which has $W < \Delta F$ (see Fig. 1.5). These are the second law violating paths. Various issues related to the distribution are explained in Ref. [24] by using the cumulant expansion.

One may note that the definition of work used above is different from the

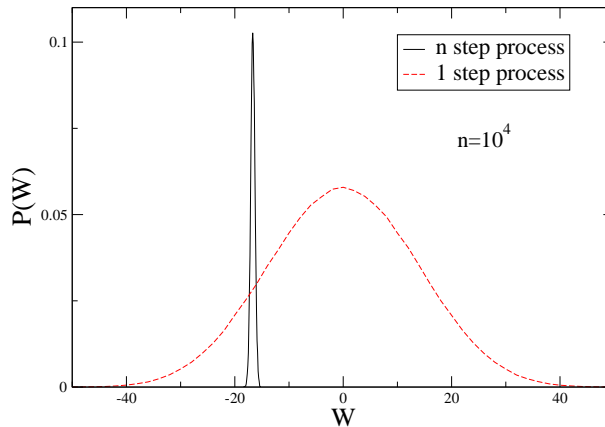


Figure 1.5: A comparison of the work done between a 1-step process and an n -step process. For large n , the work distribution shows a peak at W_{eq} .

definition used in mechanics which would have required

$$W_0 = \int_0^\tau \dot{X} \frac{\partial H}{\partial X} dt, \quad (1.37)$$

as the definition of work. This difference stems from the fact that since we are changing an “intensive” variable that does not scale with the size of the system, the relevant ensemble in equilibrium statistical mechanics is the constant- λ ensemble. The work done in this ensemble is given by the definition of W with an additional $-\lambda X$ in the Hamiltonian, a term generally associated with the Legendre transformation for a change of variables or ensembles. Another issue of importance is the temperature to be used. Temperature is a strictly equilibrium concept and therefore it is not possible to define temperature at any point along the finite time trajectory. However, the averaging is done over the equilibrium initial state which has a well defined temperature. The averaging over trajectories is done with this temperature with the assumption that the final temperature in equilibrium would remain the same. See Ref. [25, 26] for more elaborate discussions and controversies on these issues.

The derivation of the work theorem has been done by various means. In Ref. [27] the proof is obtained from a deterministic dynamics in the full phase space by using the Hamilton’s equation assuming weak coupling between the system and the reservoir. Later it was derived from a stochastic dynamics of the system governed

by the master equation under the assumption of a Markovian evolution and detailed balance [28] which is valid only for a particular class of models of physical reality. Ref. [29] derives the results for a microscopically reversible stochastic process. The validity of the work theorem for nonequilibrium trajectories generated with large time steps is shown in Ref. [30]. The derivation from the Feynman-Kac theorem is also well-documented in Ref. [21]. In this thesis we presented a dynamics independent general proof of the work theorem.

In our work, the work theorem is proved to be a generalized version of an old technique known as histogram method. The details of it is discussed here in detail. Only the single histogram method is illustrated here.

1.2.2 Histogram method

The histogram method is a widely used technique in Monte Carlo simulations. This method allows us to take a quantity obtained by Monte Carlo simulation at some intensive parameter value and extrapolate the results to other nearby values. This saves the computation time for other values. The idea was first given by Valleau and Card [31] and then used by Falcioni *et. al* [32] and Ferrenberg and Swendsen [33].

Histogram transformation

Let us consider the Hamiltonian:

$$H = H_0 - \lambda X. \quad (1.38)$$

The joint probability distribution of E (contribution from H_0 only) and X (contribution from the second part only) at a point (β, λ) in the parameter space is given by

$$P_\lambda(E, X) = \frac{1}{Z(\lambda)} \Omega(E, X) \exp(-\beta E + \beta \lambda X), \quad (1.39)$$

where $\Omega(E, X)$ is the degeneracy or the number of states and Z_λ is the canonical partition function given by

$$Z_\lambda = \sum_{X, E} \Omega(E, X) \exp(-\beta E + \beta \lambda X). \quad (1.40)$$

Suppose we want to find the average of a quantity $A(E, X)$. The histogram of the pair (E, X) generated by the MC simulation is proportional to $P_\lambda(E, X)$. The normalized probability distribution can be used to extrapolate the same to other parameter values. If one has the average of that quantity, $\langle A \rangle$, then

$$\langle A \rangle_\lambda = \sum_{E, X} A(E, X) P_\lambda(E, X) \quad (1.41)$$

$$= \frac{\sum_{E, X} A(E, X) \Omega(E, X) e^{-\beta E + \beta \lambda X}}{\sum_{E, X} \Omega(E, X) e^{-\beta E + \beta \lambda X}}. \quad (1.42)$$

Similarly, for another value of the parameter λ' , we can write the average of the same quantity A as

$$\langle A \rangle_{\lambda'} = \frac{\sum_{E, X} A(E, X) \Omega(E, X) e^{-\beta E + \beta \lambda' X}}{\sum_{E, X} \Omega(E, X) e^{-\beta E + \beta \lambda' X}} \quad (1.43)$$

$$= \frac{\sum_{E, X} A(E, X) \Omega(E, X) e^{-\beta E + \beta \lambda' X} \frac{e^{\beta \lambda X} e^{-\beta \lambda X}}{\sum_{E, X} \Omega(E, X) e^{-\beta E + \beta \lambda X}}}{\sum_{E, X} \Omega(E, X) e^{-\beta E + \beta \lambda' X} \frac{e^{\beta \lambda X} e^{-\beta \lambda X}}{\sum_{E, X} \Omega(E, X) e^{-\beta E + \beta \lambda X}}} \quad (1.44)$$

$$= \frac{\sum_{E, X} A(E, X) P_\lambda(E, X) e^{\beta(\lambda' - \lambda)X}}{\sum_{E, X} P_\lambda(E, X) e^{\beta(\lambda' - \lambda)X}}. \quad (1.45)$$

Hence, by using the histogram, $P_\lambda(E, X)$, at λ one can get $\langle A \rangle_{\lambda'}$, at λ' , and, the normalized probability distribution with new parameter λ' can be expressed in terms of the distribution with λ as:

$$P_{\lambda'}(E, X) = \frac{P_\lambda(E, X) \exp[\beta(\lambda' - \lambda)X]}{\sum_{E, X} P_\lambda(E, X) \exp[\beta(\lambda' - \lambda)X]}. \quad (1.46)$$

Again we can write from the above equation as,

$$\frac{\Omega(E, X) e^{-\beta E + \beta \lambda' X}}{Z_{\beta, \lambda'}} = \frac{\frac{\Omega(E, X) e^{-\beta E + \beta \lambda X}}{Z_{\beta, \lambda}} \exp[\beta(\lambda' - \lambda)X]}{\sum_{E, X} \frac{\Omega(E, X) e^{-\beta E + \beta \lambda X}}{Z_{\beta, \lambda}} \exp[\beta(\lambda' - \lambda)X]}, \quad (1.47)$$

$$\Rightarrow Z_{\beta, \lambda'} = Z_{\beta, \lambda} \sum_{E, X} P_\lambda(E, X) \exp[\beta(\lambda' - \lambda)X]. \quad (1.48)$$

This can be extrapolated to an arbitrary number of variables in the following way. If the Hamiltonian is now, $H = H_0 - \sum_k \lambda_k X_k$, then the probability distribution

at $\{\lambda^i\}$ can be related to that at $\{\lambda^f\}$ as,

$$P_{\{\lambda^f\}}(X) = \frac{P_{\{\lambda^i\}}(X) \exp[\beta \sum_k (\lambda_k^f - \lambda_k^i) X]}{\sum_X P_{\{\lambda^i\}}(X) \exp[\beta \sum_k (\lambda_k^f - \lambda_k^i) X]}. \quad (1.49)$$

Monte Carlo implementation

The Monte Carlo approach is a fundamental tool to study the thermodynamic properties of model systems. The thermal averages are performed by taking a finite set of judiciously chosen states instead of taking into account all possible states of the system. These states form the canonical Boltzmann probability distribution

$$P_T(E) = \frac{1}{Z_T} \Omega(E) \exp(-E/T), \quad (1.50)$$

for each possible (total) energy value E , where T is the fixed temperature (in unit of k_B , or, $k_B = 1$), $\Omega(E)$ is the degeneracy of energy level E , and

$$Z_T = \sum_E \Omega(E) \exp(-E/T), \quad (1.51)$$

is the partition function. In the Monte Carlo technique some random movements, for instance, through one-spin flip, starting from the current state of the system, are made in the phase space according to some dynamic rule which produces this probability distribution. By repeating the process many times one forms an ensemble of states. The thermal average $\langle A \rangle_T$ of some quantity A (magnetization, susceptibility, specific heat, etc.) is then simply the average of this quantity over the generated ensemble of states. To get an accurate value of the thermal averaged quantity one must take care of statistical correlations and fluctuations through any of the standard procedures. Normally one needs to calculate $\langle A \rangle_T$ as a function of some parameter, e.g., T . So, one has to repeat the entire process for each different value of T . In order to save computer time, an appealing strategy consists in extracting out the T dependence from Eqs.((1.50)) and ((1.51)). First, the distribution $P_T(E)$ itself is measured by keeping a histogram, the number of occurrence of each value of E , during the sequence of simulated states. Then, one can infer another distribution $P_{T'}(E)$ corresponding to a different value T' *without* performing any further computer run, simply by reweighting Eqs.((1.50)) and ((1.51)).

This approach is known as the histogram method [34, 35]. The thermal average at temperature T is then

$$\langle A \rangle_T = \sum_E A(E) P_T(E), \quad (1.52)$$

where $A(E)$ is the value of A obtained at fixed energy E . Once one has the reweighted distribution $P_{T'}(E)$ from Eq.(1.46), Eq.(1.52) can be applied to obtain $\langle A \rangle_{T'}$ for other temperatures T' without doing any simulation. The probability distribution $P_T(E)$ presents a sharp peak at $\langle E \rangle_T$ and decays exponentially on both sides. The larger the system size, the narrower is this peak. Thus, the computer measured $P_T(E)$ is only reliable around the peak, the statistics being poor in the exponential tails. The reweighting procedure corresponds to replacing the Boltzmann factors appearing in Eqs.(1.50) and (1.51) by other Boltzmann factors corresponding to the new value T' , transforming the whole function $P_T(E)$ into $P_{T'}(E)$. In particular, the probability values are reduced near the former peak, and enhanced near the new peak position $\langle E \rangle_{T'}$. However, since the statistics is poor near this new peak position, the inferred $P_{T'}(E)$ is not accurate. That is why this simple histogram method (known as the single histogram method), in spite of its elegant reasoning, had difficulties in practice which later has been improved by introducing new methods: broad histogram method and multi-histogram method, to avoid the exponential tails responsible for the drawback of the single histogram method.

1.3 An equivalent quantum system: two interacting particles and quantum phase transition

Previously we have mentioned in Sec. 1.1.3 that the classical problem of unbinding transition of two interacting polymers, like DNA, can be mapped onto an equivalent quantum problem of dissociation of two interacting quantum particles. Then the concepts and results of the classical phase transition can be borrowed to analyze quantum entanglement and the entanglement entropy. This section discusses the problem of quantum entanglement, its measures and the connection to polymer entropy as a prerequisite of the Chapters 4 and 5.

1.3.1 What is quantum entanglement?

Quantum entanglement [36, 37, 38, 39] is a fundamental feature of quantum mechanics that tells us about the quantum correlation of two particles or subsystems spatially apart. It says that performing a local measurement may instantaneously affect the outcome of local measurements far away. When a composite quantum system is in a pure state, then even if the subsystems are spatially far apart and non-interacting, the measurement on one subsystem affects that on the other instantaneously. This “spooky action at a distance” later gave birth to the term “entanglement”. This phenomenon was first marked by Einstein, Podolsky and Rosen in a gedanken experiment [40], known as the EPR paradox. In their paper, they considered two particles which interacted for some time and showed that it is possible to measure the conjugate non-commutating quantities, like position and momentum, simultaneously, which violated the quantum theory. For example, one may take a pair of particles in the zero total momentum state. Then, when they are far apart, one may measure the momentum of one particle with arbitrary precision to predict the momentum of the other one. At the same time the position of the second particle can be measured precisely so that both position and momentum are determined with arbitrary precision. Later it was resolved and came the idea of the quantum entanglement which indicates the presence of the inherent quantum correlation between the two particles or any two subsystems. We define an entangled pair as follows:

Definition: When a bipartite pure state can not be written in terms of a product of two states of individual parts, then the two parts are entangled.

This notion can be made more quantitative with the help of density matrices.

A quantum state can be pure or mixed. A pure state can be described by a single wave-function or by a linear superposition of other states. On the other hand, a mixed state is a statistical mixture of pure states. For example, interacting particles like an EPR pair, or more specifically in the two-particle energy eigenstate are examples of pure states. On the other hand, a quantum system in thermal equilibrium is described by the probabilities of the various energy eigen-states but it is not describable by a wave function. Such states, called mixed states, are

described by a density matrix which is represented by an operator

$$\rho(1,2) = \sum_{ij} c_{ij} |\phi_i\rangle\langle\phi_j|, \quad (1.53)$$

where $|\phi_i\rangle$'s form a set of wave-functions of the system. For a pure state of two parts 1 and 2,

$$\rho(1,2) = |\phi(1,2)\rangle\langle\phi(1,2)|.$$

A pure state satisfies $\rho^2 = \rho$. Consequently, for a normalized density matrix $\text{Tr}\rho^2 = 1$ but for a mixed state, $\text{Tr}\rho^2 < 1$.

A reduced density matrix for one part is defined by

$$\rho = \text{Tr}_2 \rho(1,2),$$

by tracing over part 2. This trace operation indicates the absence of any information about the second part. If the reduced density matrix is not pure, i.e. $\rho^2 \neq \rho$, then the two parts are defined as entangled. Necessarily, the reduced density matrix is not separable in this situation. Needless to say, if the reduced density matrix for part 1 is not pure, it will not be for part 2 either.

Signature of quantum phase transition

There is another feature of quantum mechanics where the zero-point fluctuations in the ground state may coherently add up to produce long-range correlations of local observables. This happens at quantum critical points (QCP), a point where the spectrum becomes gapless, obtained by tuning some parameter, say g , of the Hamiltonian. A QPT occurs at zero temperature and at the QPT the ground state energy is non-analytic with respect to some parameter in the Hamiltonian. The ground-state energy E_0 remains continuous through the quantum phase transition (QPT) point at $g = g_c$. If there is a slope discontinuity of E_0 as $g \rightarrow g_c \pm$, the QPT is called a first order transition otherwise it is a continuous transition or a quantum critical point (QCP).

For particle dynamics, one may use a dimensional argument to characterize the phase transition. The gap in the spectrum Δ , defined as the separation of the

ground state from the rest of the spectrum, gives a length scale

$$\xi \sim \frac{\hbar}{\sqrt{2m\Delta}},$$

where m is the relevant mass scale. A time scale for the quantum dynamics may also be defined as

$$\tau = \frac{\hbar}{\Delta}.$$

The significance of these scales become clear in a path integral formulation where one considers trajectories in space and time. As the gap closes, $\Delta \rightarrow 0$, both the scales $\xi, \tau \rightarrow \infty$ signaling a transition because diverging length and time scales are the hallmarks of any phase transition.

For the two particle problem, when the ground state energy approaches zero, the bottom of the continuum, the width of the wave-function becomes large. This is an indication of correlations between the two particles even if they are far apart, beyond the range of interaction. With diverging scales, the composite wave function is not expressible as a product of individual wave functions. Simply stated, critical states are necessarily entangled, but the converse is not necessarily true. There are states that are entangled but not critical.

The wave function encodes not only the non-analyticity associated with a QPT, but also the special quantum entanglement intrinsic to the state. A QPT is fully governed by the quantum fluctuation and hence one would expect that the quantum entanglement would show special signatures at the QPT.

1.3.2 Quantification of entanglement

Depending on the number of partitions of a quantum many body system, quantum entanglement can be of different types, such as bipartite (entanglement between two subsystems), multipartite (entanglement between multiple subsystems).

To quantify the entanglement, various definitions of entanglement entropy are explored [38, 37, 41], though a few can be used for exact computation. The conditions to be satisfied by the measure of the entanglement are: (i) it should be zero for a product state, and (ii) it should not change under local unitary operations or choice of bases. A much studied measure is in terms of an “entropy”. The most common among these measures are the von Neumann entropy and the Renyi

entropy. As discussed later, the problem we consider involves a gapless entanglement spectrum. The usual proof of the positivity of entanglement entropy is not applicable in case of continuous eigenvalues of the reduced density matrix.

von Neumann entropy

The von Neumann entropy is the widely used measure of entanglement. If ρ is the reduced density matrix obtained from a two particle density matrix, as described above, then the von Neumann entropy is defined as

$$S^{vN} = -\text{Tr } \rho \ln \rho \begin{cases} = 0 & \text{for a product state (no entanglement),} \\ \neq 0 & \text{for a nonproduct state (entangled).} \end{cases} \quad (1.54)$$

It is maximum for a completely mixed state. The von Neumann entropy is the quantum generalization of the Shannon entropy. It maps a density matrix to a number, its von Neumann entropy. It is generally considered as a canonical measure of the entanglement for a pure bipartite state. For mixed states it is more complicated to evaluate.

Renyi entropy

The Renyi entropy was first proposed by Renyi [42] in 1960 from the perspective of information theory. The idea is to look for the most general function that quantifies the uncertainty in a system. The Renyi entropy of the combined system of A and B is defined as

$$S_n = \frac{1}{1-n} \ln[\text{Tr } \rho_{AB}^n]. \quad (1.55)$$

The von Neumann is obtained from the Renyi entropy in the limit $n \rightarrow 1$. The Renyi entropy of order two, called the extension entropy [43], is closely related to the inverse participation ratio. In the case of $n = 0$, the Renyi entropy is a function of the number m of positive components of the vector ρ , $S_0 = \ln m$. In the limit $n \rightarrow \infty$, we obtain a quantity analogous to the Chebyshev norm, $S_\infty = -\ln \rho_{\max}$, where ρ_{\max} is the largest value of ρ .

It is found that the entanglement entropy behaves in different ways for a first order and a continuous QPT. The critical behaviour of the entanglement entropy has drawn much attention now-a-days [44] and has been investigated for different

spin models [39, 45, 36] as well as in continuum systems [46].

1.4 Random walk in disordered media

In the last chapter we view the polymer as a random walker. A Gaussian polymer can be modeled as a random walker on a lattice. Time in the random walk problem corresponds to the contour length of the polymer. For a polymer of length N , the mean square of the end-to-end distance R is given by $\langle R^2 \rangle \sim N$. With R corresponding to the displacement $X(t)$ of the walker after time $t = N$, this result is expressed in the random walk analogy, as $\langle X(t)^2 \rangle = 2Dt$, which is the well-known diffusion law, D being the diffusion coefficient.

Further, disorder plays an important role in the case of polymers, e.g., to model spatially varying stiffness, interaction to the wall for adsorbed polymers etc. It is thus interesting to study the problem of random walk itself, which finds applications in many other systems whose underlying dynamics have a direct correspondence. Thus, for the random walker, disorder is introduced in the microscopic transition rates. Random walk in disordered media, which often gives rise to anomalous diffusion, is an extensively studied topic. In this chapter, we concentrate on certain commonly encountered forms of randomness in the hopping rates and study the effect of such disorder on the diffusion and persistence property of the random walk.

1.4.1 Persistence probability $P(t)$

An important quantity for a polymer is the reunion probability or the probability of loop formation for a single chain discussed in Sec. 1.1.2. The reunion probability of the polymer corresponds to *persistence* probability $P(t)$ in the random walk analogy. For the 1D random walk, if the walker starts at x_0 , $P(t)$ is the probability that $x(t) - x_0$ does not change sign upto time t . It is known that, for a Gaussian stationary process, persistence probability has the form, $P(t) \sim e^{-\theta t}$, where θ is called the persistence exponent [47]. A process $X(T)$ is stationary if the two-time correlation function has the form

$$C(T_1, T_2) = \langle X(T_1) X(T_2) \rangle = f(|T_1 - T_2|).$$

For a normal random walk in 1D, $\langle x(t_1)x(t_2) \rangle \propto \min(t_1, t_2)$, and thus defining $T = \ln t$ and $X(T) = x(t)/\langle x^2(t) \rangle$, we immediately see that, $X(T)$ is a stationary process in the logarithmic time T ;

$$\langle X(T_1)X(T_2) \rangle = \frac{\langle x(t_1)x(t_2) \rangle}{\sqrt{\langle x^2(t_1) \rangle \langle x^2(t_2) \rangle}} = \frac{\min(t_1, t_2)}{\sqrt{t_1 t_2}} = e^{-\frac{1}{2}|T_1 - T_2|}. \quad (1.56)$$

Hence, for the process $X(T)$, the persistence probability decays exponentially, $P(T) \sim e^{-\theta T}$ with $\theta = 1/2$ and therefore, in real time t , persistence probability for the original random walk process $x(t)$ has a power-law decay,

$$P(t) \sim t^{-\theta_0}, \quad \theta_0 = \frac{1}{2}. \quad (1.57)$$

In a large number of stochastic processes, persistence exponent is found to be a new nontrivial exponent and is apparently unrelated to the usual dynamical exponents. This quantity probes high order temporal correlations in dynamics and depends on the whole history of the time evolution of the system and further characterize a given stochastic process. It is difficult to determine analytically as it depends on the full functional form of the two-time correlator, not only on its asymptotic form. Thus, in this work we study the persistence of random walkers in a disordered systems in order to understand better the complexity of anomalous diffusion processes in these systems.

1.4.2 Diffusion in disordered media

Diffusion in disordered media is an extensively studied topic within the general problem of transport in disordered media [48] with wide ranging physical interest and applicability. The classic theories of transport valid for crystals do not apply in non-crystalline, disordered materials, and the physics of transport, and in particular diffusion, is anomalous in these disordered systems. Some examples are: the problem of transport in fractured [49, 50] and in porous [51] rocks, anomalous density of states in randomly diluted magnetic systems [52], in silica aerogels [53] and in glassy ionic conductors [54], anomalous relaxation phenomena in spin glasses [55] and in macromolecules [56], conductivity of superionic conduc-

tors such as hollandite [57] and of percolation cluster of Pb on thin films of Ge or Au [58, 59, 60], diffusion controlled fusion of excitation in porous membrane films, polymeric glasses and isotropic mixed crystals [61] etc. Most of the above mentioned systems, the density of the basic dynamical entities are so small that the problem can be treated as a non-interacting one, i.e., basic dynamical quantities performing the random walk are essentially independent of each other. Thus, solving the single walker problem is sufficient in determining the transport properties of these system.

The effects of disorder in these systems may be classified into three qualitatively different regimes based on the diffusion properties.

1. Normal diffusion with renormalization of D : If the strength of disorder is weak (to be quantified in the context of the specific systems) the asymptotic form of diffusion, $\langle x^2 \rangle = 2Dt$, remains unaltered, only the numerical value of diffusion coefficient D changes.
2. Anomalous diffusion: Above a certain strength of disorder, the diffusion law itself is modified, $\langle x^2 \rangle = K_\beta t^{2\beta}$, where the wandering or spreading exponent $\beta \neq \frac{1}{2}$ is usually a function of the strength of the disorder as well.
3. Extreme effect of disorder: In some rare systems, disorder may lead to extremely anomalous transport properties, e.g., in the Sinai model [62, 48], $\langle x^2 \rangle \sim (\ln t)^4$.

In most systems, disorder distribution has a narrow spread around a finite mean value, and these fall in to the first category. In the present work we make a detailed study of the second category of systems with relatively strong disorder. We will see that in the case of our interest, anomalous diffusion results due to effective long-range correlations in disorder or a broad waiting time distribution or both. Further, we will consider diffusion on regular lattices. Anomalous diffusion resulting from fractal properties of the underlying lattice is of some physical interest and has been studied in a number of earlier works [48, 113].

1.4.3 Modeling disordered media

The motion of a single random walker in a disordered system is described by a master equation for the probability distribution of the walker on a lattice. The

transition rates between neighbouring sites are random, and their distribution chosen defines the specific model studied. In particular, one dimensional systems have been studied extensively [63]-[69]. These systems are most generally described by the master equations

$$\frac{dP_n}{dt} = \sum_j [W_{j,n}P_j - W_{n,j}P_n], \quad (1.58)$$

where $n(n = 0, \pm 1, \pm 2, \dots)$ denotes the lattice sites, $P_n(t)$ is the probability of finding the walker or the amplitude of excitation at site n at time t , and the transfer rates (or coupling constants) $W_{i,j} \geq 0$ are assumed to be independent random variables, distributed according to a given probability density $\rho(W)$. In the most commonly studied systems, W 's are nonzero only for nearest neighbours (i.e., $W_{i,j} = 0$ unless $|i - j| = 1$) and they are chosen such that there is no local or global bias on the random walker.

The following classes of distributions $\rho(W)$ for transition rates $W_{n,n+1}$, essentially cover most physical systems of interest.

Class (a). $\rho(W)$ is such that

$$\left\langle \frac{1}{W} \right\rangle \equiv \int_0^\infty dW W^{-1} \rho(W) < \infty. \quad (1.59)$$

Class (b). $\rho(W)$ is such that $\langle \frac{1}{W} \rangle = \infty$. A single parameter choice of such a distribution is,

$$\rho(W) = (1 - \alpha) W^{-\alpha}, \quad W \rightarrow 0, \quad 0 \leq \alpha < 1. \quad (1.60)$$

1.4.4 Anomalous diffusion due to broad waiting time distributions

In all the models of disorder we consider, it is known that the mean square displacement $\langle x^2 \rangle \sim t^{2\beta}$, where the wandering or spreading exponent β depends on the exponent α of Eq.(1.60). Consider a random walk on a regular lattice where a particle has to wait on an average a time τ before performing the next jump¹.

¹The actual waiting time is Poisson distributed as $p(\tau') = \tau e^{-\tau'/\tau}$

Let this mean waiting time is a random variable and changes with each jump to a value which is chosen from a distribution: $w(\tau)$. One can think of this problem as diffusion among traps where fixed mean waiting time is not associated forever with a given site but changes with each new visit and thus the disorder is introduced in an *annealed* way. If the distribution of mean waiting times is broad enough then anomalous diffusion results. E.g., for a power law distribution of mean waiting times,

$$\omega(\tau) \sim \tau^{-\mu}, \quad (1.61)$$

one obtains,

- for $1 < \mu < 2$, subdiffusive behaviour with $\langle x^2(t) \rangle \sim t^{\mu-1}$,
- for $\mu = 2$, $\langle x^2(t) \rangle \sim \frac{t/\tau_0}{\ln(t/\tau_0)}$,
- for $\mu > 2$, finite τ and normal diffusion, $\langle x^2(t) \rangle = 2Dt$.

1.5 Organization

The above-discussed topics are the main issues of concern in this thesis. The thesis is organized as follows.

In Chapter 2, we analyze by using thermodynamics the equilibrium phase transition of DNA by force. The thermodynamics is developed at the critical force. Here, instead of looking at the phases, we observe the interface between the two coexisting phases at the transition force. The helical order is considered in our study along with the penetration of the external force inside the zipped phase. In two extreme regimes of these two competitive phenomena, the surface energy has opposite signs. The positive surface energy being normal, we emphasize on the discussion of the effect of a negative surface energy on the phase diagram. In analogy to superconductors, when the interfacial energy becomes negative, one gets a *mixed* phase of DNA and the zipped-mixed phase transition becomes continuous. Based on the sign of the zipped-unzipped interfacial energy we classify DNA into two types: Type II has a negative interfacial energy whereas Type I is the conventional case with a positive interfacial energy. This classification is not related to the existing classification based on DNA conformation.

In the next chapter, Chapter 3, the phase transition of a DNA hairpin under a periodic force is considered. A two-state model provides phenomenological descriptions of systems that can exist in two different forms. In fact, the two-state model is shown to provide a good description of the folding-unfolding dynamics of small DNA or RNA hairpins that display a strong cooperativity [70, 71] as well as structural transitions. On the basis of the results obtained by Mishra et. al. [72], in Chapter 3, we show that similar results can be obtained by any two-state system. We use an Ising ferromagnet to study the dynamical phase transition under a periodic force. Both the system shows hysteresis near the critical force. A dynamical phase diagram, in magnetic field *vs.* frequency (of the applied field) plane, is proposed which is qualitatively similar to that of DNA hairpin in force *vs.* frequency plane.

In Chapter 4, for the same two state Ising ferromagnet system, we then try to get back the equilibrium magnetization curve from the nonequilibrium measurements. As a tool, we exploit the work theorem. We present here a generalized, dynamics independent proof of the work theorem. The work theorem is shown to be a consequence of the exact histogram transformation. Combining these two, the work theorem and the histogram transformation, we show that any equilibrium probability distribution can be obtained from the principal eigen-value of a specially constructed matrix, whose elements are obtained from the nonequilibrium measurements of work done along the path connecting the states having initial and final magnetic field. These results indeed gives a good equilibrium magnetization curve, These are verified by Monte Carlo simulations and applications to Barkhausen-type noises are done.

Chapter 5 and Chapter 6 look at a different aspect of the DNA phase transition. The equivalent quantum problem of two interacting particles, obtained from the imaginary time transformation of the classical problem of two interacting polymers, is discussed. As the interaction, we consider both a short range square well (in Chapter 5) and a long range inverse square potential (in Chapter 6). The relevant quantity to observe the signature of the quantum dissociation is the quantum entanglement entropy. In the short range case, the von Neumann entropy is found to be negatively divergent near the unbinding transition, which is a quantum critical point. For the long range one, there is an adjustable quantity, the strength of the $1/r^2$ potential, which can be controlled to get either a first order or

a continuous unbinding transition. It is found that for the second order transition the entanglement entropy diverges negatively, but for the first order it is finite. A scaling relation is found from a data collapse. The negative entropy, though counterintuitive, is actually essential for the phase transition. The connection to the equivalent polymer problem shows the correspondence between the quantum entropy and the polymer bubble entropy (discussed in Sec.1.2), and explains the importance and genuinity of the negative entropy. This study is extended to the Renyi entropy and some results are mentioned.

In Chapter 7, we go back to the classical problem. Here we view a polymer as a stochastic path, like a Gaussian polymer maps on to a random walker, with the same space-time scaling. In this picture, the reunion probability of the polymer becomes the persistence probability of a random walker. We study a random walker in a disordered lattice, where the disorder is modeled through the randomness in the hopping rates. In our model, both site and bond disorders are considered. The annealed disorder averaging and quenched disorder averaging give different results of various quantities, though all the models have same hopping rate distribution. The usual quantities in this context like mean squared displacement, two point incremental correlations, waiting time distributions are verified with known results. Our main interest is to study the persistence behaviour in all these four cases, which is found to have a power law behaviour with new exponent called the persistence exponent. We find that though the persistence exponents in the annealed bond, annealed site, and quenched site disorder is same, the quenched bond disorder case is qualitatively different. It does not show a monotonic change with the disorder strength. The behaviour of the persistence probability is explained using the first passage time distribution and using properties of fractional Brownian motion.

We summarize our findings of the thesis in Chapter 8.

2

TYPE II DNA: when the interfacial energy becomes negative

DNA in its double helical form shows a resilience against an external pulling force. The bound state does not allow a force g applied at an end to penetrate up to a critical force $g = g_c$, above which the DNA gets unzipped [2, 3, 4]. The transition is first order for temperatures $T < T_c$ where T_c is the denaturation (melting) temperature in the absence of any force [8]. In this chapter, we study the thermodynamics of the unzipping transition. The phase transition is looked from another aspect, by observing the surface energy. The surface energy is quantified from a free energy functional in the linear response regime. We propose a new classification of existing DNAs into two types, Type-I and Type-II, like superconductors, depending on the sign of the energy of the interface separating the zipped and the unzipped phases.

2.1 Introduction

The force-induced unzipping transition of DNA is due to a competition between the bond orientation by force and ordering by base pairing. The formation of a helically ordered dsDNA from denatured strands is a symmetry breaking transition. At a coarse-grained level, the ordered state can be described by an order parameter ψ , with $\psi = 0$ for the denatured state. The external force does not couple directly to this order parameter. Consequently, at a junction of a bound and an unzipped DNA, there is a need to define two length scales: one scale ξ that gives the length

over which the DNA ordering is damaged on the bound side of the interface, while the other scale λ gives the distance over which the force penetrates the bound state. The existence of the second scale λ was pointed out by de Gennes in a model involving stretching of the backbone and the hydrogen bonds [73]. Generally one expects interfaces separating phases to be energetically costly (e.g. surface tension), but here we show that if $\lambda \gg \xi$, then the interfacial energy, or surface energy, between bound and unzipped DNA can become negative. There can then be a penetration of force in the form of distorted regions or “defect blobs” of length λ enclosing a denatured bubble of size ξ . In analogy to superconductors, when the interfacial energy becomes negative, one gets a mixed phase of DNA and the zipped-mixed phase transition becomes continuous. Based on the sign of the zipped-unzipped interfacial energy we classify DNA into two types: Type II has negative interfacial energy whereas Type I is the conventional case with positive interfacial energy. This classification is not related to the existing classification based on DNA conformation.

A Type II DNA has novel features which are of considerable biological and physical implications. To be noted that the defect blobs are different from thermally created bubbles. This is because the bubbles of the latter type would consist of random configurations of denatured strands generated by thermal fluctuations and may have positive interfacial energy. The distinctness of the defect blobs can be a signature for their identification in biological processes. Let us consider the transcription process where the genetic code, determined by the base sequence, is transferred to the amino acid sequence of a protein. For correct transcription, the sequence must be read from the correct starting point on DNA. These starting non-coding regions are called promoter regions and their identification is the first and vital step in transcription [74]. A pulling force or a forced separation in a homogeneous Type II DNA produces a finite density of the defect blobs [75] (discussed later). The non-coding sequences or the promoter regions may act as inhomogeneities on a DNA and could play the role of pinning centers for the defect blobs. The advantage of physical identification of pinned defect blobs could facilitate recognition of the promoter regions for gene expression (e.g. see Ref. [76, 77]). So far as physical properties are concerned, Type I and Type II DNA will have different phase diagram and phase transition as discussed later.

Recently, both in experiment [78] and simulation [79], a continuous transition

has been observed if the topology is preserved in a stretching experiment by pulling both the strands either at both ends or at one end of an anchored DNA. We also note that a detailed molecular dynamics study [80] of under- or over-wound DNA without writhe, observed the formation of localized sequence-dependent defects which allow the rest of the dsDNA to be in the relaxed normal state. It is known that topoisomerase II may bind anywhere on the DNA but its topology changing activity is restricted to specific sequences (cleavage sites) indicating that geometric distortions get localized around certain sequences [81]. These are consistent with our general predictions, though we like to add that interfacial information in any of these cases are not available.

2.1.1 Outline

The outline of the chapter is as follows. In Sec.2.2, we develop the thermodynamics of the phase transition. A qualitative discussion is done on the behaviour of the interface, followed by a quantitative calculation of the surface energy at the critical force by constructing the free energy functional. The phase transition is then explained in view of the sign of the surface energy. In Sec.2.4, we summarize our result.

2.2 Theory and results

2.2.1 Thermodynamics

The thermodynamic description of unzipping of DNA requires three variables, ψ describing the helical ordering (i.e., broken symmetry) and a force-displacement (g, x) conjugate pair, where x is the scaled separation between the two strands at the point of application of force g . On the bound side x can be taken as the response to an internal induced force \tilde{g} , so that,

$$x(\tilde{g}) = \chi\tilde{g}, \tag{2.1}$$

where χ , the stretchability or the response function, is independent of g in the linear response regime. Though we restrict to linear response regime here, the final results can be reproduced for a general force-dependent χ . The variables are

chosen such that $\psi = 0$ for the unzipped state, and $\psi \neq 0$ for the ordered state, while $\tilde{g} = 0$ in the bulk of the ordered state. At this point it is to be noted that the order parameter ψ represents helical ordering which is not directly coupled to the external pulling force. As a result we get two independent length scales in the problem. This makes the present treatment different from other existing models.

For a homogeneous state, the Gibbs free energy $G(T, g)$ per unit length at temperature T and a pulling force g is given by

$$G(T, g) = G(T, 0) - W(g), \quad (2.2)$$

where $W(g) = \int_0^g x(g') dg'$ is the work for stretching. The conditions of phase coexistence at $g = g_c$ is

$$G_z(T, g_c) = G_u(T, g_c). \quad (2.3)$$

Here the subscripts z and u represents the zipped and the unzipped phases. Another condition needed is for the non-penetration of force in the bound state for $g \leq g_c$. This is given by,

$$G_z(T, g) = G_z(T, 0). \quad (2.4)$$

Substituting Eq.(2.3) and (2.4) in Eq.(2.2), we get a relation for the free energies as,

$$G_z(T, g) = G_u(T, g) + W(g) - W(g_c). \quad (2.5)$$

Eq.(2.5) agrees with the known exact results discussed in Sec. 1.1.1 when appropriate $x(g)$ from the exact solution is used. In particular one verifies that

$$G_z - G_u = \frac{1}{2}\chi(g^2 - g_c^2), \quad (2.6)$$

in the linear response regime (near melting).

Compared to the stretched unzipped state, the zipped phase has to pay a cost $W(g)$ for force expulsion for not following the force-diktat, but gains energy $W(g_c)$ due to binding or ordering. The phase coexistence requires a perfect compensation of one by the other. This compensation may be used to obtain the binding energy of the zipped phase as,

$$E_z(T) = W(g_c). \quad (2.7)$$

This equation may also be used to define g_c from the binding energy.

2.2.2 Surface energy

Let us now consider an inhomogeneous situation of a dsDNA at $T < T_c$ by pulling at one end by a force $g = g_c(T)$ so that there is an interface separating the coexisting zipped and unzipped phases. The interfacial energy is obtained by comparing this mixed state free energy with that of a fully unzipped homogeneous state at $g = g_c$. Needless to say that an interface can be created spontaneously if there is a gain in energy in doing so.

Since far from the interface, the Gibbs free energy density is the same in the two phases, the total free energy \mathcal{G} can be written as

$$\mathcal{G} = \int_{-\infty}^{\infty} G_u(T, g_c) dz + \sigma, \quad (2.8)$$

where σ is the “surface tension”, and z is a contour length measured along the DNA or the strands, the $z = 0$ point being chosen at the point of interface with $z < 0$ as the unzipped phase.

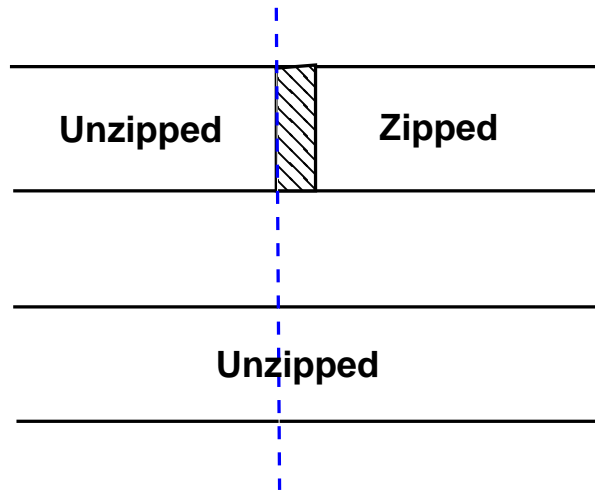


Figure 2.1: Schematic representation of two configurations, fully zipped (above) and a configuration of coexisting phases separated by an interface (below) at $g = g_c$. The difference in the free energies of this two configuration gives the interfacial energy.

A practical way to define the surface energy is to force an interface by choosing

appropriate boundary conditions as shown in Fig. 2.1. Let us consider a DNA maintained in the zipped (z) state at $z = +\infty$ but in the unzipped (u) state at $z = -\infty$. This guarantees at least one interface. At phase coexistence, we compare its free energy with the case for which the DNA is maintained in the u state at both $z = \pm\infty$. The difference of the total free energy is the surface energy. Therefore,

$$\sigma = \int_0^\infty dz [G(g_c) - G_u(g_c)]. \quad (2.9)$$

We start with the free energy functional

$$F_{\text{tot}} = \int_{-\infty}^\infty dz \mathcal{F}\{\psi, x\}, \quad (2.10)$$

whose minimum gives the equilibrium free energy in a fixed distance ensemble. The functional $\mathcal{F}\{\psi, x\}$ can be taken as

$$\mathcal{F}\{\psi, x\} = F_u + F\{\psi\} + \frac{K_\psi}{2} \left(\frac{\partial\psi}{\partial z} \right)^2 + \frac{K_x}{2} \left(\frac{\partial x}{\partial z} \right)^2 + \int_0^x g(\tilde{x}) d\tilde{x}. \quad (2.11)$$

where $F\{\psi\}$ is the free energy of the homogeneous bulk zipped phase with reference to the unzipped state free energy F_u . In the unzipped state $F\{\psi\} = 0$. K_ψ and K_x are additional “elastic” constants for distortions in ψ and x . The elastic part of the free energy can be extended to torques. The order parameter ψ and force \tilde{g} are not coupled in the free energy in the form taken in Eq.(2.11) and consequently, this form is valid only in extreme limits. Further generalizations are not needed for this chapter. The Gibbs free energy is obtained from Eq.(2.11) by using the equilibrium values of ψ and x , followed by a Legendre transformation from x to g .

The equilibrium conditions, obtained by minimizing F_{tot} , are

$$\frac{\delta F}{\delta\psi} - K_\psi \frac{\partial^2\psi}{\partial z^2} = 0, \quad (2.12)$$

$$-K_x \frac{\partial^2 x}{\partial z^2} + \frac{x}{\chi} = 0, \quad (2.13)$$

with the condition that

$$\psi = 0, \quad x = x_c = \chi g_c \quad \text{at} \quad z = 0, \quad (2.14)$$

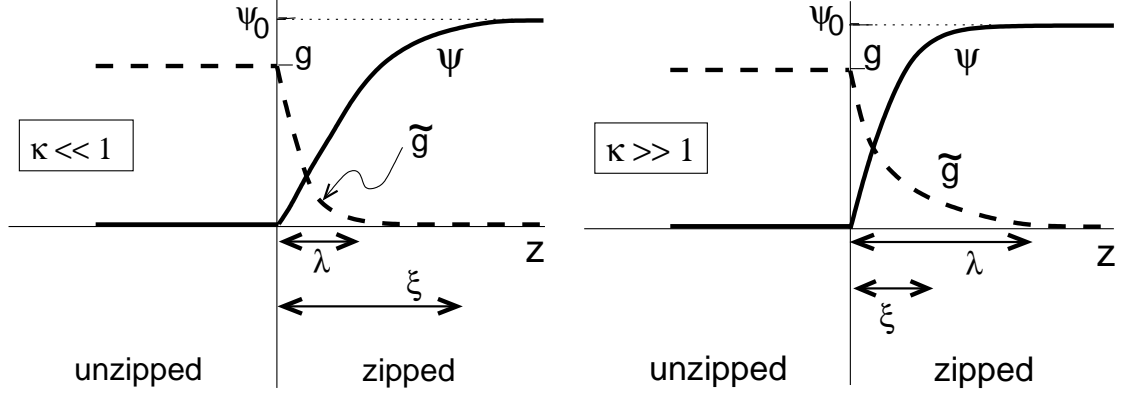


Figure 2.2: Schematic diagram of variation of zipping-unzipping order parameter ψ (continuous line) and applied force g (dashed line) inside unzipped and zipped phases. ξ is the length scale of variation of ψ inside the zipped phase and λ is the scale for g . For Type I (left figure), $\kappa = \lambda/\xi \ll 1$ and for Type II (right figure), $\kappa \gg 1$.

and

$$\psi = \psi_0, \quad x = 0 \quad \text{at} \quad z \rightarrow \infty, \quad (2.15)$$

ψ_0 being the solution of

$$\frac{\delta F}{\delta \psi} = 0$$

to maximize the interfacial energy. The length scales ξ and λ , giving how fast ψ or \tilde{g} grow or decay inside the zipped phase (see Fig. 2.2), come from Eqs. (2.12) and (2.13), as

$$\xi^{-2} = \frac{1}{K_\psi} \left(\frac{1}{\psi} \frac{\partial F}{\partial \psi} \right) \Big|_{\psi \rightarrow 0}, \quad \text{and} \quad \lambda^2 = K_x \chi. \quad (2.16)$$

The equation for λ reduces to the form derived by de Gennes [73] if the elastic constants of his model are used for K_x and χ . The dimensionless ratio

$$\kappa = \lambda/\xi \quad (2.17)$$

is expected to be different for different sequences of DNA.

By using Eqs.(2.11), (2.12) and (2.13), the surface energy can be written in

terms of the free energy as,

$$\begin{aligned}\sigma &= \int_{-\infty}^{\infty} dz [G(g_c) - G_u(g_c)] \\ &= \int_0^{\infty} dz \left[F_{z\tilde{g}}(x) - x \cdot g_c - F_u + \frac{\chi}{2} g_c^2 \right],\end{aligned}\quad (2.18)$$

where we use the fact that

$$G_u(g_c) = G_u(0) - \frac{1}{2}\chi g_c^2 = F_u - \frac{1}{2}\chi g_c^2, \quad (2.19)$$

and

$$G(\psi, g) = F\{\psi_{min}, x_{min}\} - x_{min} \cdot g_c. \quad (2.20)$$

Extreme limit I: $\kappa \ll 1$

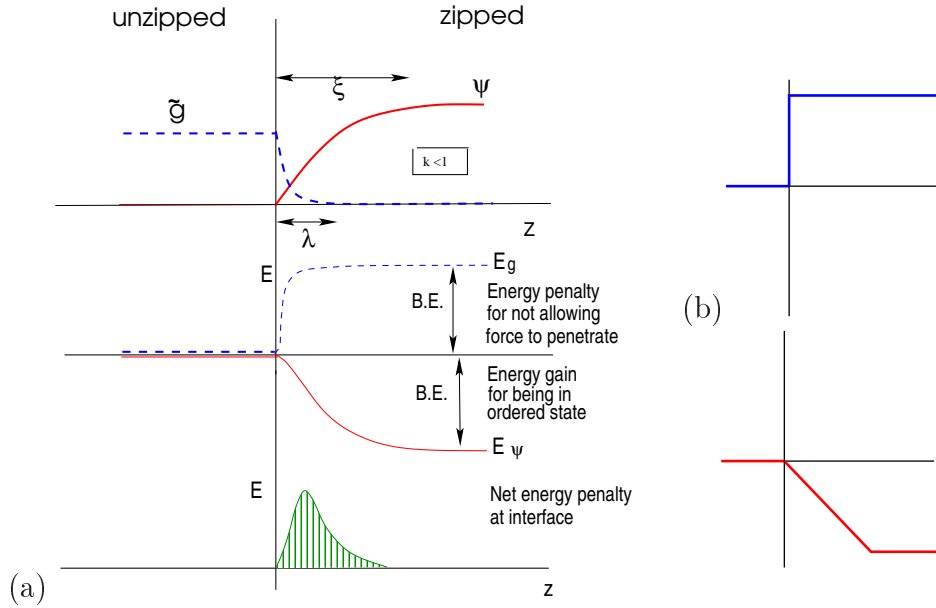


Figure 2.3: (a) Schematic diagram of the variation of the force and the helical order inside the zipped phase for $\xi \gg \lambda$ (left figure), resulting in a positive surface energy. (b) The figure shows the ideal situation of $\xi \gg \lambda$.

For $\kappa \ll 1$, the external force penetrates only a short distance λ into the zipped region. In contrast the order parameter rises to its asymptotic value ψ_0 in a much larger length ξ . One has to pay the energy cost for the damage in ordering

Chapter 2. TYPE II DNA: when the interfacial energy becomes negative

over a length scale ξ . Therefore, in the extreme limit, when the variation can be approximated as in Fig. 2.3b, one gets,

$$\sigma \sim E_z \xi = \frac{1}{2} \chi g_c^2 \xi \quad (2.21)$$

which is positive. This can be understood from a pictorial representation of the variation of the energy, with respect to the unzipped phase and inside the zipped phase shown in Fig. 2.3a. This is the conventional scenario of force expulsion of various models on the zipping-unzipping phase transition and this scenario gives the well-known behavior of the unzipping transition.

The surface energy can be calculated using Eq.(2.18) for any κ more accurately. As we are more interested in the sign of the surface energy, we concentrate in the said extreme limit, which simplifies the expression of surface energy and the result comes out easily. In the said limit, one can ignore the variation of x inside the zipped phase. So the term with $(\partial x / \partial z)^2$ can be neglected. Also $x \approx 0$ for $z > 0$. Putting these in Eq.(2.18) yields,

$$\sigma = \int_0^\infty dz \left[F\{\psi\} + \frac{K_\psi}{2} \left(\frac{\partial \psi}{\partial z} \right)^2 + \frac{1}{2} \chi g_c^2 \right], \quad (2.22)$$

which under the condition that $F\{\psi\} \geq -\frac{1}{2} \chi g_c^2$ gives $\sigma > 0$.

Extreme limit II: $\kappa \gg 1$

When $\kappa \gg 1$, the force penetrates a greater distance λ into the sample, so that there is an obvious gain in the stretching energy (i.e. reduction of the “positive energy” for force expulsion) over the interval of penetration, over and above the gain by ordering. From the diagram shown in Fig. 2.4a, it can be understood qualitatively that the surface energy becomes negative, and in the ideal case, as shown in Fig. 2.4b, it becomes

$$\sigma = -\frac{\chi g_c^2}{2} \lambda, \quad (2.23)$$

which is negative. The sign of the surface energy can be confirmed by calculating it from Eq.(2.18). In this limit, we neglect the term with $(\frac{\partial \psi}{\partial z})^2$ and write the surface

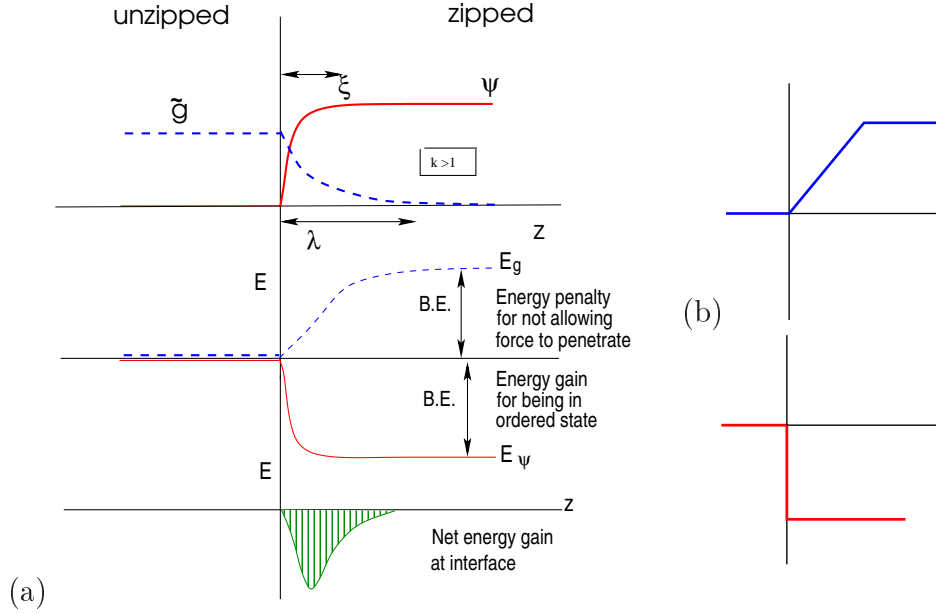


Figure 2.4: (a) Schematic diagram of the variation of the force and the helical order inside the zipped phase for $\xi \ll \lambda$ (left figure), resulting in a negative surface energy. (b) The figure shows the ideal situation when $\xi \ll \lambda$.

energy as,

$$\sigma = \int_0^\infty dz \left[\frac{K_x}{2} \left(\frac{\partial x}{\partial z} \right)^2 + \frac{1}{2\chi} x^2 - x \cdot g_c \right]. \quad (2.24)$$

Then by using the condition that $F_z^{min}\{\psi\} = -\frac{\chi g_c^2}{2}$ and Eq.(2.13), one can easily derive that $\sigma < 0$ in the limit $\kappa \gg 1$. Hence, it is possible to lower the free energy of the DNA by creating the interface.

The value of κ for transition from Type I to Type II depends on the form of χ which, in turn, depends on the DNA sequence and the secondary structure. It is therefore primarily the sequence but also the secondary structure that determine whether a DNA would behave like Type I or II.

2.3 Discussion

If we now consider the bulk zipped state with a force g , then force penetration may be possible in the form of many isolated distorted regions or blobs. For $\lambda \gg \xi$, with the unzipped core of size ξ costing an energy $E_z \xi$, and the x part of the free

energy $\mathcal{F}\{\psi, x\}$ in Eq.(2.11), one finds for a homogeneous chain that a periodic structure of the blobs [75], as in Fig. 2.5, is possible energetically, if $g > g_c/\sqrt{\kappa}$. The initial penetration of force is at $g_{c1} = g_c/\sqrt{\kappa}$ with periodicity $d \rightarrow \infty$. The unzipping transition therefore becomes continuous in contrast to the first order nature for Type I.

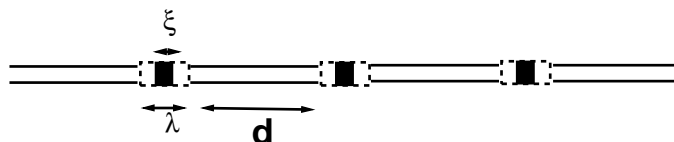


Figure 2.5: Schematic diagram of a periodic array of defect blobs. The array has a periodicity d which controls the density of blobs. Each distorted region is of length $\sim \lambda$ with an unzipped core of size $\sim \xi$.

The negative interfacial energy is found in Type II superconductor [82] too. Our formulation is similar to that of Type II superconductivity in a one-dimensional geometry. As there is indeed a phase transition in DNA, the Landau theory is justified here. It suffices for a one dimensional case to consider a scalar order parameter.

We may point out a few additional implications of a negative interfacial energy. The penetration of the force is not possible in the conventional polymer models. For any helical or twisted pairs of strings, a pulling force produces over-winding. We expect this over-winding in DNA to be present at the interface, distorting but not vitiating the ordered state. The resulting distortion plays a role in determining the interfacial energy. The penetration of force is via a denatured core of size ξ , surrounded by such a distorted region of size λ . These defect blobs could be pinned by certain sequences, thereby localizing them in specific regions of the DNA. We speculate that the regions which localize the defect blobs are the non-coding promoter regions. This gives a topological interpretation of the defect blob and it would also be applicable to torque. The existence of the mixed or Type II phase with pinned defect blobs will affect the melting profile under a force, and the force-distance isotherm will show steps originating from the blobs, especially for finite chains. Our analysis shows that the relation between ordering and unzipping is needed to get a negative interfacial energy. The helical ordering is not just base-pairing – it involves stacking and other distant neighbor interactions. Any

microscopic model for Type II DNA would have to take these into account. On the experimental front, it is time for a second generation single molecular experiments that would explore the interfaces on DNA.

2.4 Summary

To summarize, in this chapter we showed that different types of phenomena happen for two regimes of the ratio $\kappa = \frac{\lambda}{\xi}$ of the independent length scales ξ and λ , of DNA order parameter (ψ) and internal force (\tilde{g}) respectively. For $\kappa \ll 1$, the interfacial energy is positive, and the unzipping or melting under a force is first order. The external force has no effect inside the ordered, or, zipped phase, i.e., there is no internal force (\tilde{g}) inside as λ is small. This is named Type I. On the contrary, for $\kappa \gg 1$, the interfacial energy becomes negative and the force penetrates the zipped phase in the form of defect blobs. The creation of interfaces are energetically favored, so that interfaces are formed spontaneously. Thus defect blobs are formed inside the ordered phase. Above a force threshold $g > g_{c1}$, there will be a finite density of these defect blobs. The melting under tension of unzipping is second order. This case is named Type II.

What next: In the next chapter, we consider a time-dependent force on DNA instead of a static one. The molecular dynamics simulation of a DNA hairpin shows that there is a possibility of a dynamical phase transition. We obtain the similar dynamical phase transition from a simpler two-phase system like Ising magnet under the periodic force. We infer that some basic features of these two systems are responsible for the behaviour under time-varying force, not the details of the dynamics.

List of symbols

\mathcal{F}	Free energy functional
χ	Proportionality constant for response to applied force
E_z	Binding energy of z phase
F	Helmholtz free energy
g	Applied force on DNA
g_c	Critical force for force-induced unzipping
$G_{z,u}(T, g)$	Gibbs free energy of z or u phase at temperature T under force g
κ	Ratio of length scales, λ/ξ
K_ψ	Elastic constant for ψ
K_x	Elastic constant for x
λ	Length scale of penetration of force inside zipped phase
σ	Surface energy
T_c	Critical temperature for DNA melting
\tilde{g}	Induced force inside the zipped phase
T	Temperature
W	Work done for stretching
ξ	Length scale of damage in helical order
x	Separation of two strands of DNA at the point of application of force
ψ	Helical order parameter
z	Axis along the length of DNA

3

Dynamical phase transition of a driven Ising magnet

During biological processes like, replication, transcription, etc., DNA is opened by helicases, which are motors that move along the DNA [74]. Both the motion and the opening processes require constant supply of energy. A few examples are DNA-B, a ring like hexameric helicase that pushes through the DNA like a wedge [83], PcrA that goes through cycles of pulling the ds part of the DNA and then moving on the ss part [84], viral RNA helicase NPH-II that hops cyclically from the ds to the ss part of DNA and back [85]. Such cycles of action and rest, with periodic ATP consumption, indicates exertion of a periodic force on the DNA. It drives us to study the DNA phase transition under a periodic drive in an experimentally realizable situation. This dynamics is studied by using a molecular dynamics (MD) simulation. In this chapter, we show that the results for DNA actually resembles that obtained from a much simpler system, namely, an Ising ferromagnet under a periodic field. The reason that the two systems behave in the similar way is very fundamental.

3.1 Introduction

The equilibrium unzipping transition is described by the two thermodynamic conjugate variables, force g and separation x of the pulled base pair (see Sec. 1.1.1). If one thinks of a quasi-static thermal equilibrium process where the force is changed from zero to a maximum g_m and then back to zero, keeping other intensive quan-

ties fixed, then one would retrace the thermodynamic isotherm, ending at the initial state. In other words, there is no role of history in thermodynamics; this is ensured by ergodicity in statistical mechanics. However the situation is different under a periodic force. The external timescale for change of force may not match the relaxation time for DNA which then explores a smaller region of the phase space. This creates a difference in the response to an increasing or a decreasing force. The deviation from the thermodynamic path looks prominent near a phase transition when the typical time scales of dynamics become large. This leads to hysteresis in DNA unzipping [86]. More recently Kapri [87] showed how the work theorem can be used *via* a multi-histogram method to extract the equilibrium isotherm from hysteresis curves

The study of hysteresis is an old topic mainly in the context of magnetic and structural systems [88, 89] because of their practical importance, but all these studies involve the time-averaged loop. In the case of DNA, Mishra *et al* showed that there are situations, depending on the force amplitude and the frequency, where sample to sample variations are too large to ignore. With the advent of single-molecule experiments on short DNA chains (oligomers), it might be possible to probe the time-resolved loops, not just averages. Motivated by the biological relevance and the experimental feasibility, the behavior of DNA under a periodic force, called a *periodically driven DNA*, was studied. The results show that without changing the physiological conditions (*e.g.* the temperature or pH of the solvent), a DNA chain may be brought from the unzipped state to the zipped state and *vice versa* by varying the frequency (ν) alone.

A well-studied example of a similar dynamic symmetry breaking transition is in magnets [89]. As a two phase system, we make use of the magnetic Ising model to corroborate the behavior of DNA. This study is prompted by the often-used description of the unzipping transition by a two state Landau type free energy functional [90, 91, 92] similar to the Ising model. We establish that the observed features and the phase diagram in both the cases are robust and generic, even though they are different models with different types of dynamics.

3.1.1 Outline

The chapter is organized as follows. In Sec. 3.2 we recapitulate the results of a driven DNA hairpin. In Sec. 3.3 we introduce our magnetic model and discuss the numerical method to get the desired quantities. The results are analyzed in terms of time resolved loops in Sec. 3.4. It contains the explanation on why the standard quantity fails and one needs to think in terms of a more finer quantity. Finally, in Sec. 3.5 we summarize our main content of this chapter.

3.2 Driven DNA and results

A DNA hairpin consists of a stem of pair of complementary bases and a loop of non-complementary bases (see Fig. 3.1). It is chosen not only because of its occurrence *in vivo* and its use in *in-vitro* experiments but also because of the extra entropic effect coming from the loop. The non-paired bases of the loop is a source of entropy which in turn controls the dynamics of hysteresis. Langevin dynamics (LD) simulations of a DNA hairpin were performed in Ref [86] to simulate the hysteresis behaviour of DNA. The separation x of the terminal base pairs pulled by a periodic force $g(t)$ of time period $\tau(= 1/\nu)$ was monitored. The force is applied at one end of the hairpin keeping the other end fixed. The simulation is performed in reduced unit as discussed in [72].

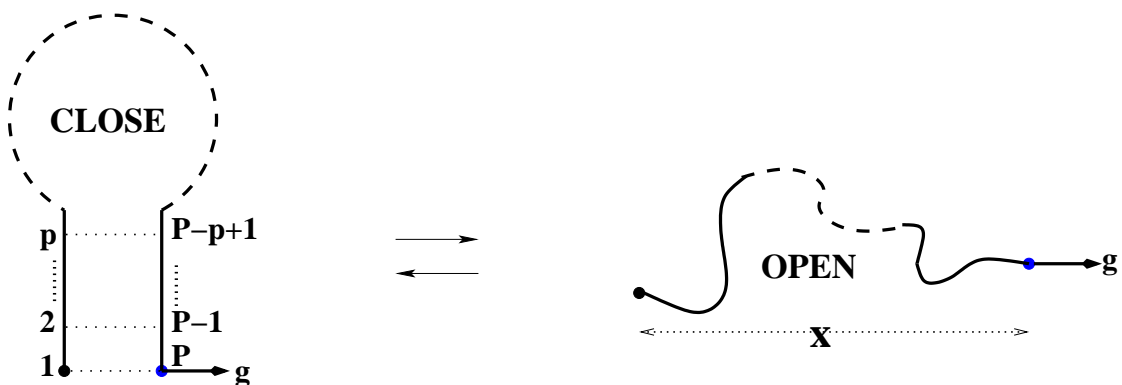


Figure 3.1: A DNA hairpin of total length $P = 32$ in (a) a zipped (Z) and (b) an unzipped (U) state. The stem (solid lines) of length $p = 10$ consists of complementary nucleotides with native interaction (dotted lines) for base pairing, whereas the loop (dashed line) is made up of non-complementary nucleotides.

The configurational energy [86] of the DNA hairpin is written as sum of harmonic terms for the bonds and the Lennard-Jones potential between complementary nucleotides [86]. The effect of a periodic force is taken into account by adding an extra energy $-g(t).x(t)$ to the total energy of the system. With this energy, the zero force melting temperature in reduced units is $T = 0.21$, while the critical force at $T = 0.1$ is $g_c \sim 0.20$ [93]. During the simulation, g is changed from 0 to the chosen maximum, g_m , and then back to 0. This one period is to be referred to as *a cycle* and g_m as the amplitude. By changing g_m or ν , it was found in Ref. [72] that it is possible to induce a dynamical transition between a state of time averaged zipped (Z) or unzipped (U) to a dynamical state (D) oscillating between Z and U. The operational definition adopted in Ref. [72] is the following. If $\langle x \rangle$ is less than 5, the system is in the zipped state and larger than 5 it is in the unzipped state.

In Fig. 3.2, the plots of the average value of $x(g)$ over \mathcal{C} ($= 1000$) cycles vs g , for different values of g_m and ν are shown. We point out the salient features of these loops.

1. One notes a large variation in the size and shape of the loops which remain almost the same (except (23)) for different samples or starting condition.
2. Like other hysteresis loops, DNA hysteresis also shows the phase lag between the force and the extension, e.g., $x(g)$ increases even when the applied force decreases from g_m (Fig. 3.2 (32 & 33)). If the system could approach equilibrium, the lag disappears, as one sees in Fig. 3.2(21 & 31).
3. At a high frequency, the DNA remains in Z or in U depending on whether $g_m < 2g_c$ or not, (Fig. 3.2(13)&(43)), irrespective of the initial conformation. For a relatively smaller ν , a different sequence (Fig. 3.2 (11,21 & 31)) is observed. The DNA starts with $x = 0$ at the start of the cycle, *i.e.*, in the Z phase and comes back to the Z phase but via the U-phase with $x = 30$.
4. In the case of intermediate forces there is a significant change in the x -values at $g = 0$ and $g = g_m$ (Fig. 3.2 (21, 22 & 23)). Most striking here is the wide sample to sample fluctuations in the loop which could not be reduced.

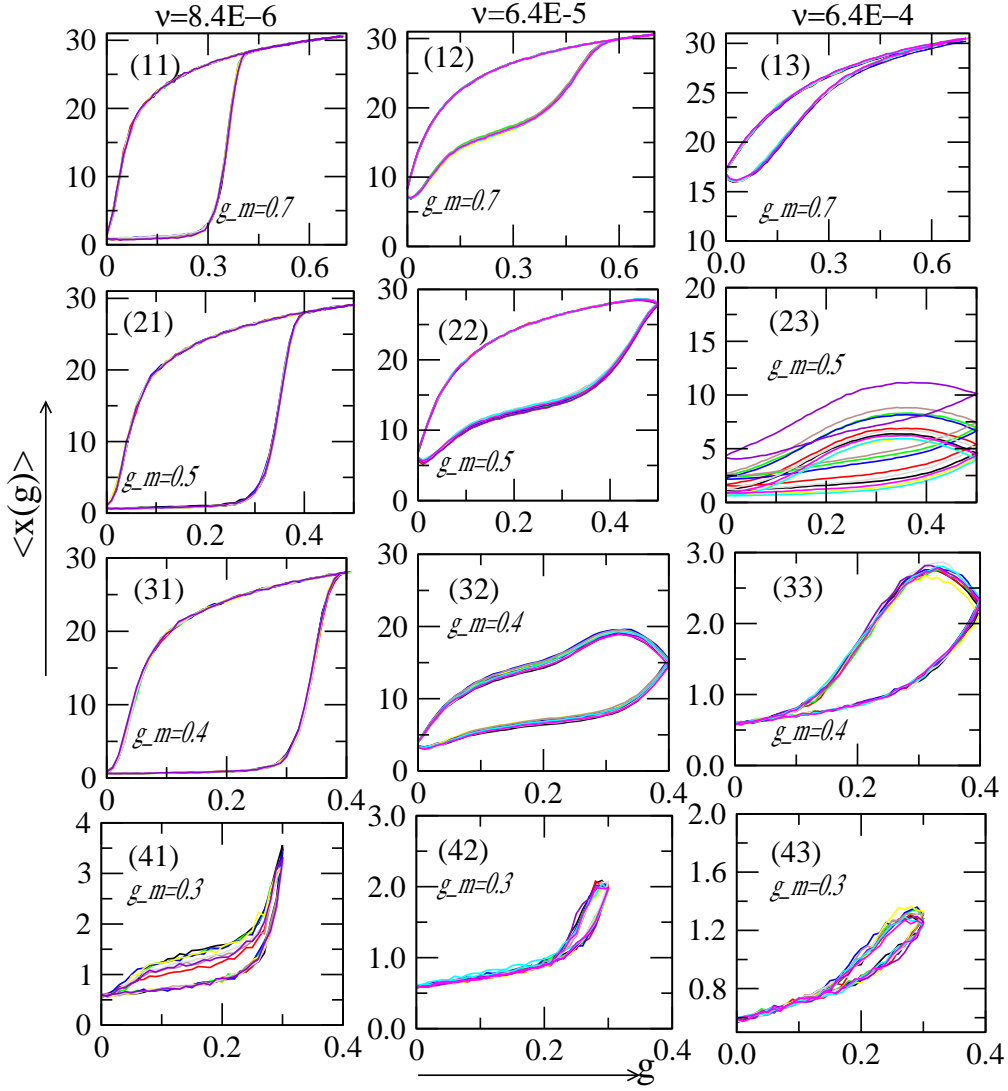


Figure 3.2: DNA hysteresis for different g_m and ν as indicated. Each plot contains the loops for 10 different initial conformations. These are at $T = 0.10$, for which $g_c \sim 0.20$ (see Ref. [72]).

The failure of the average response to provide a description of the steady state dynamic behavior prompts us to analyze the distribution of paths over the different cycles in terms of a new quantity which can probe the states over one cycle. This is elaborated in the following sections.

3.3 Magnetic model and method

As mentioned already, an Ising system is a two phase system (up magnet and down magnet) undergoing a field-induced first order transition below the critical temperature. We study the dynamic response under an asymmetric magnetic field. Our aim is to look at the time-resolved response to compare with the DNA-hysteresis behaviour.

3.3.1 Model

Let us consider a two-dimensional Ising spin system ($\{s_i = \pm 1\}$) with nearest neighbor interaction and under a magnetic field h ,

$$H = -J \sum_{\langle i,j \rangle} s_i s_j - h \sum_i s_i, \quad (J > 0), \quad (3.1)$$

with i labeling the sites of an 8×8 square lattice with periodic boundary conditions. The infinite lattice critical temperature is $T_c \approx 2.269J/k_B$ in zero field. The magnetization is defined as the thermal average

$$m = N^{-1} \sum_i \langle s_i \rangle, \quad (3.2)$$

of $N (= 64)$ spins. For the above Hamiltonian, we choose $J = 1$ and $k_B T = 2$ with $k_B = 1$, so that $T < T_c$. Below the critical temperature T_c , the magnetization, $m = \sum_i s_i$ takes the sign of the applied field, and the magnitude depends on the strength of the field due to finite size effect. There is a first order phase transition at $h = 0$ with a jump in the magnetization. The hysteresis is the signature of that phase transition away from equilibrium. The hysteresis loop is the curve in the $m-h$ plane for a complete cycle of variation of the magnetic field from h_l to h_m and back. The area of the hysteresis loop depends on how fast or slow the magnetic field is varied.

3.3.2 Procedure

The Monte Carlo procedure used is as follows. We choose a spin, calculate the change in energy ΔE of the system if the spin gets flipped. Whether this spin would

be flipped or not is determined by using the standard Metropolis algorithm, which gives the probability of acceptance of an attempted flip by $P_{\text{accept}} = \min(1, e^{-\beta\Delta E})$. In this way, we sequentially consider all the N spins, one at a time, to attempt a flip. The time taken to attempt N spin flips constitutes one MC sweep.

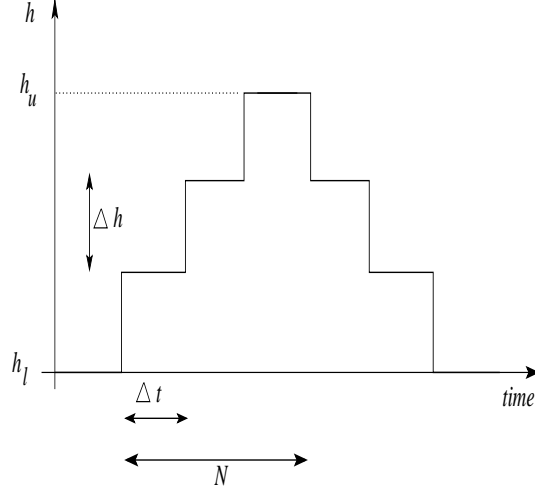


Figure 3.3: One cycle of magnetic field with time.

Suppose the system is subjected to a periodic magnetic field with the field at the j th step as

$$h_j = h_l - \sum_{i=-N}^{j-N} n \text{sign}(i) = h_l + \Delta h(N - |j - N|), \quad (j = 0, \dots, 2N), \quad (3.3)$$

where $h_l (< 0)$ is the starting value or the lowest value of magnetic field over a cycle, N is the number of steps to reach upper value or the highest value of the magnetic field over a cycle, after which field is decreased, Δh is the change in magnetic field in each step, $\Delta h = (h_m - h_l)/N$. As per our notation, $h_0 = h_{2N} = h_l, h_N = h_m$. Initially system is equilibrated at $h_l = -0.6$ and $k_B T = 2$. Then the periodic magnetic field is switched on. At each step, (i) the magnetic field is increased by $\Delta h = (h_m - h_l)/N$ and (ii) the system is relaxed towards equilibrium by $n = 5$ MC sweeps, which is much less than the equilibration time. The magnetization m is calculated at each of such $2N$ steps. The average of magnetization calculated over a cycle then gives the quantity Q . The above process is repeated for 10^4 cycles. Below T_c , the steady state depends on both the frequency, $\nu = 1/(2N\Delta t)$,

where Δt is the number of Monte Carlo sweeps at that temperature and magnetic field to relax the system for a while, and the amplitude h_l and h_m of the periodic field. Because of the up-down symmetry of the system, we see different behaviour of the state for two cases: one where the field is symmetrically varied around zero with $h_m = -h_l$ and the other where it is asymmetric. In order to compare with the force-frequency (g - ν) diagram of the DNA hairpin we take the case of an asymmetric variation of the magnetic field with time. The lower amplitude (h_l) is kept fixed at a negative value while the upper one (h_m) is varied. We simulate the system for various frequencies (by controlling \mathcal{N}) and different values of h_m , keeping h_l fixed.

3.4 Numerical results

Like the case of DNA, the hysteresis of the Ising ferromagnet also shows large sample to sample fluctuations and different kinds of shapes. Therefore, we look at a finer level. We define a quantity, the average magnetization over a cycle, as

$$Q = \frac{1}{\tau} \int_0^\tau m(t) dt. \quad (3.4)$$

It is the dynamical order parameter studied in the context of magnetic systems [89]. The time sequence of Q seems not to indicate any regular pattern (see Fig. 3.4), and, therefore, we assume that the allowed states occur randomly. The time sequence can then be interpreted in terms of a probability of getting a particular value of Q . We find that the steady state is described by a stationary probability distribution ($P(Q)$) which are also shown in Fig. 3.5.

At equilibrium, for a symmetric cycle, i.e., with $h_l = -h_m$, we expect $Q = 0$. But if h_m is varied from a value a little higher than h_l to a value which is well above $-h_l$ then away from equilibrium Q should vary from a value close to equilibrium value of magnetization at h_l to that of $-h_l$, which in our case will be any value from -8^2 to 8^2 . An asymmetric field in the Ising model enables us to distinguish the two differently ordered phases, the counterparts of the zipped and the unzipped states and, in addition, a *hysteretic state*, to be called the *dynamic state* D. For easy comparison, the negatively magnetized state is named Z while the positively magnetized state is U. The operational definition adopted is

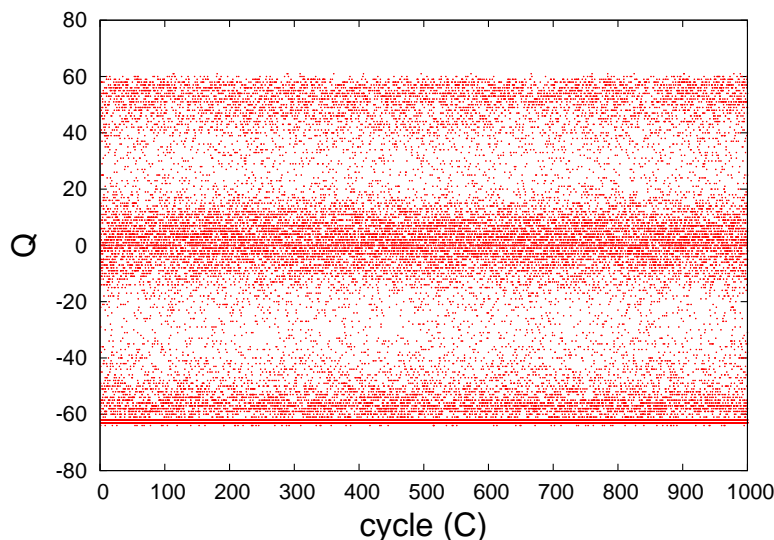


Figure 3.4: Plot shows the time sequence of Q with cycles ($h_m = 0.6$, $\nu = 1/70$). Three bands indicate that the states with different Q values occur randomly.

- (i) $Q_Z \equiv \{-64 \leq Q \leq -40\}$,
- (ii) $Q_U \equiv \{55 \leq Q \leq 64\}$, and
- (iii) the rest is Q_D .

Cases (i) and (ii) occur when the paths in the m - h diagram remain on one side throughout the cycle, and case (iii), the dynamical state, D, occurs either if there are paths connecting the positive and the negative values of the magnetization or if the paths remain more or less near zero of magnetization. The division of the three intervals or regions are independent of h_m .

As we find the Q values of consecutive cycles are random and has no indication to stabilize, we plot the distribution $P(Q)$ to find out the phases. To be noted that the division of three intervals or regions are independent of h_U and cut-off values are chosen suitably by observing the distribution of Q 's such that two regions do not overlap in $P(Q)$ vs Q plot. Below is the plot of $P(Q)$ vs Q (Fig. 3.5) for different frequencies for fixed h_l and same set of h_m .

3.4.1 Dynamical phase diagram

From the peak locations of $P(Q)$, we map out the phase diagram of the Ising magnet in the h_m - ν plane (Fig 3.6). A line in Fig. 3.6 represents a boundary

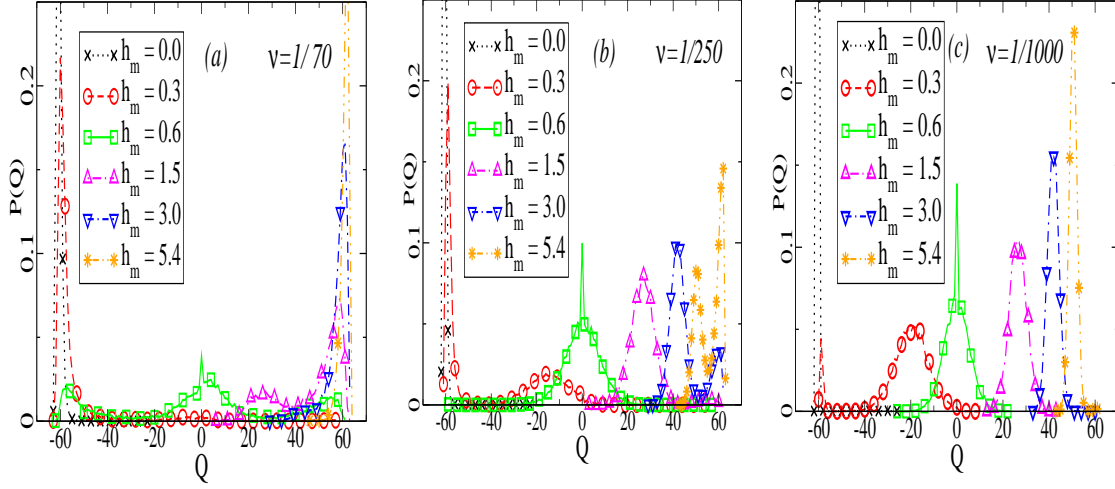


Figure 3.5: The distribution of Q is plotted for three different frequencies and same set of h_m . For a frequency, the distribution $P(Q)$ shifts as h_m increases. It goes from Z-state to U-state through D-state. The corresponding states/phases in Q are identified observing the distribution. (a) frequency $\nu = 1/70$. Phases: $Z \rightarrow Z+D \rightarrow Z+D+U \rightarrow D+U \rightarrow U$. (b) frequency $\nu = 1/250$. Phases: $Z \rightarrow Z+D \rightarrow D \rightarrow D+U \rightarrow U$ (c) frequency $\nu = 1/1000$. Phases: $Z \rightarrow Z+D \rightarrow D \rightarrow U$.

beyond which a particular peak appears or disappears and resembles a first-order line.

We start at the equilibrium of h_l .

- Now set an h_m which is negative or zero. The loop connecting h_l and h_m will naturally give Q_Z . The probability distribution $P(Q)$ will show a peak near equilibrium magnetization value of h_l , for any frequency, as shown by the black dotted curve in Fig. 3.5.
- As h_m is increased to positive values, a second peak in Q_D appears. The value of h_U where the second peak appears has a very weak dependence on the frequency and has a small positive slope in the $h-\nu$ phase diagram (Fig. 3.6).
- As h_m is increased further the peak height of Q_Z decreases and that of Q_D increases with a shift in the peak position. This shift seems to be independent of frequency.
- There is a range of magnetic field for which two peaks, at Q_Z and Q_D , coexist.

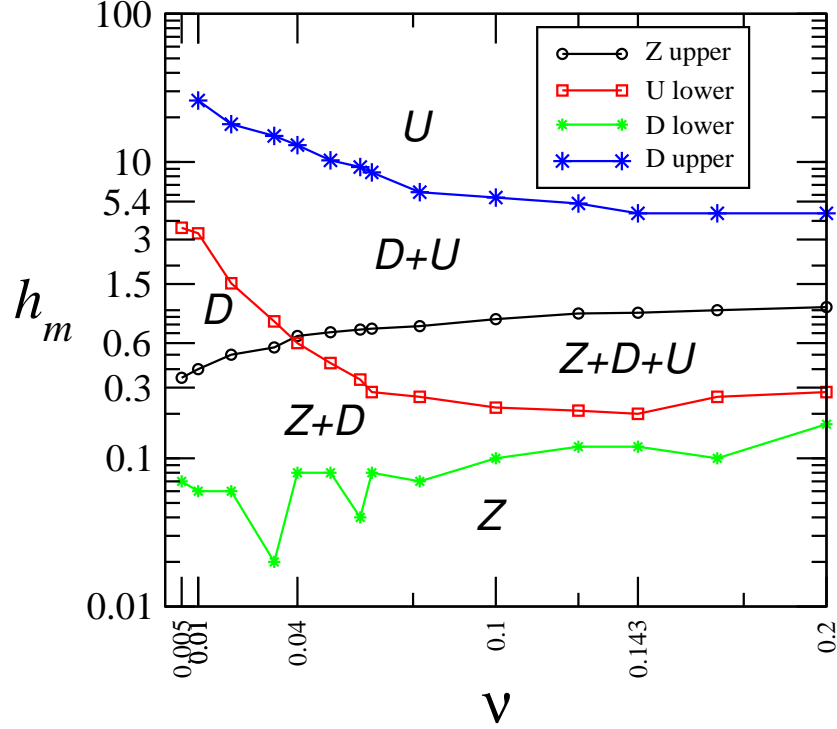


Figure 3.6: Dynamical phase diagram of a periodically driven Ising ferromagnet in the h_m - ν plane. The lines are boundaries for various phases U , D and Z . Here Z corresponds to the negatively magnetized state, U corresponds to the positively magnetized state and D is the dynamical state. The points are from the simulation and the lines are guide to eye.

This phase is shown as $Z+D$ in the phase diagram.

- At some h_m , the peak at Q_Z vanishes. This threshold h_m depends on the frequency and the dependence is shown in the h - ν diagram by the black dashed curve with circles. Now, at this h_m two things can happen. Either Z phase vanishes leaving alone the D phase, or, by that time the U phase (the peak at Q_U in Fig. 3.5) appears and the system shows the coexistence of three phases, $Z+D+U$. In the latter case, as Z vanishes, the system remains in a mixed state of $D+U$. When the peak in Q_U or U phase will reappear again depends on the frequency. This dependence is shown by red dash-dotted curve with squares.
- We see there is an intersection of the two curves, boundaries of Z and U in the phase diagram of Fig. 3.6. This is a special point exactly at $h_m = -h_l$

where Z disappears and U appears at a same time. If one goes along the horizontal line through $h_m = h_l$ in phase diagram, i.e. keeping h_m fixed at $-h_l$ but varying the frequency, then at very low frequencies one would see only the D phase for some range, and then as the frequency increases two other peaks at Z and U will appear. If the frequency is increased further, the peak at Q_D vanishes leaving the coexisting phase of $Z+U$. The span of the three phase coexistence region depends on the value of h_l . The $Z+D+U$ region may even become very small.

- Going back to the previous cases, after having the two possibilities that the system is either in D only or in $Z+D+U$, if the upper magnetic field is increased then one gets the phase $D+U$. Once this phase appears, with a shifting Q_D -peak, any increase of h_m beyond the blue starred line in the phase diagram of Fig. 3.6 vanishes the intermediate peak; only one peak at U survives.
- The vanishing or decaying of the intermediate peak has different natures at different frequencies.
 - The intermediate peak first grows from zero when the green line is crossed. With increasing h_m , the peak increases first and then decreases. While the intermediate peak is decreasing, another peak at Q_U appears.
 - But for low frequencies, the peak height keeps increasing upto a very high field, even though the peak position becomes very close to the boundary of Q_D and Q_U . At very high magnetic field the peak at Q_U appears. This indicates that the phase D and U physically give two different types of loops in the m - h plane.

The U -peak shows the paths which remain in the positively magnetized states. This is similar to the Z -peak with the whole cycle in negatively magnetized states. In contrast, the D -peak appears where there are connecting paths between positively and negatively magnetized states.

See Fig. 3.7 to compare Fig. 3.6 with the dynamical phase diagram of a driven DNA. One can easily find the correspondence between the states of the two above-mentioned system.

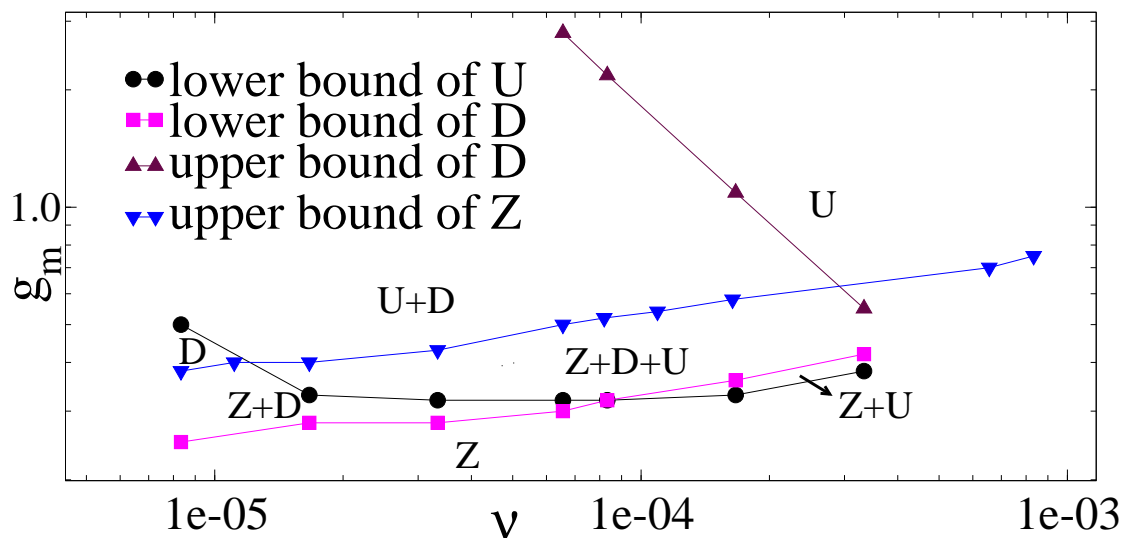


Figure 3.7: Dynamical phase diagram of a periodically driven DNA hairpin in the g_m - ν plane. The lines are boundaries for various phases U, D and Z. The points are from the simulation and the lines are guide to eye (see Ref. [72]).

3.5 Summary

In this chapter, we studied a driven magnetic system. The motivation comes from the realizable phenomenon of a DNA during transcription and replication. Both the systems, DNA and the Ising ferromagnet, are two state systems, undergoing a first order phase transition. This fundamental similarity produces qualitatively similar behaviour under a periodic drive, though the detailed dynamics are different. The results are obtained using Monte Carlo simulation of the Ising system. We emphasize here that the one should rather look at the time-resolved loops to get an exact picture of the states. A dynamical phase diagram is found in magnetic field (h) *vs.* frequency (ν) plane. The phase diagram shows the possibility of various mixed states depending on the frequency and the amplitude of the periodic field. The important outcome is that there is a possibility of going from one phase to the other just by varying frequency alone, keeping the amplitude of the external drive fixed. The same observations apply for the driven DNA.

What next: In order to get an equilibrium curve from a hysteresis loop, we develop a technique by using the work theorem and the histogram method. The results are verified again by using Monte Carlo simulation of Ising model, and can be applied to the hysteresis of driven DNA.

List of symbols

β	Inverse temperature
C	No. of cycles
Δh	Field increment
Δt	MC cycle
g	Force in DNA hairpin
H	Hamiltonian
h	Magnetic field
h_m	Upper amp. of mag.
h_l	Lower amp. of mag.
J	Nearest Neighbour interaction strength
L	Size of spin array
m	Magnetization
N	No. of steps
ν	Frequency
$P(Q)$	Prob. of Q
Q	Average response over one cycle
Q_D	Q -value for D (Dynamic) state
Q_U	Q -value for U (or +ve magnetization) state
Q_Z	Q -value for Z (or -ve magnetization) state
s	Ising spin
T_c	Critical temperature for DNA melting

4

Equilibrium probability distribution from nonequilibrium path integral

Near a phase transitions, a system under consideration has a very large relaxation time. Under an periodic drive, one observes hysteresis when the transition is first order. In such a situating, it is almost impossible to get the equilibrium or the thermodynamic curve. For example, if one wants to get, numerically or experimentally, the critical force for the unzipping phase transition of a DNA under force, one ends up with a hysteresis loop in the force-distance plane, from which it is difficult to find out the critical force accurately. We propose a different but efficient method to get the equilibrium curve from nonequilibrium measurements. In doing that, we exploit the work theorem and the histogram technique. In this chapter, we discuss this fundamental connection between equilibrium properties and nonequilibrium work done.

4.1 Introduction

A system in thermodynamic equilibrium has no memory of its past. Consequently there is no leading role for time in the ensemble based statistical mechanics except the subservient one to maintain equilibrium among the internal degrees of freedom and with external sources. This wisdom gets exploited in the dynamics based algorithms like Monte Carlo, molecular dynamics, stochastic quantization, to name a few, to attain equilibrium from any arbitrary state albeit in infinite time. Even a thermodynamic process involving changes in parameters is an infinite sequence

of equilibrium states, and is therefore infinitely slow. A finite duration process, not destined to equilibrate at every instant of time, maintains a memory of the initial conditions or a short time correlation of states. The biased sampling of the phase space keeps these processes outside the realm of statistical mechanics and thermodynamics. In this equilibrium-nonequilibrium dichotomy, a work theorem [19, 20, 22, 21, 25] attempts to bridge the gap by providing a scheme for getting the thermodynamic free energy difference from a properly weighted nonequilibrium path integral [22, 21].

We show in this chapter that purely nonequilibrium measurements of work gives an operator \mathcal{S} , defined on the phase or configuration space, whose normalized principal right eigenvector is the equilibrium probability distribution. Our result is valid for any number of parameters including temperature and interaction. With this extension we can get the equilibrium distribution by constructing a matrix \mathcal{S} connecting any two allowed states of the system without any reference to equilibrium anywhere, thereby completely blurring the boundary between equilibrium and nonequilibrium. This finds direct application in out-of-equilibrium phenomena like hysteresis.

Barkhausen noise is an example of nonequilibrium response of a ferromagnet as the magnetic field is changed at a given rate [94, 95]. By measuring the voltage induced in a secondary coil as the current in the primary coil wound around a ferromagnet is changed, one gets the time variation of the magnetization. The noisy signal one gets is not unique but stochastic in nature, reflecting the fluctuating microscopic response to the external field. Such signals have been analyzed in the past to extract information like avalanche statistics, material characteristics etc. Our results find a different use of the Barkhausen noise to construct the \mathcal{S} matrix. Similar constructions for other cases like protein or DNA dynamics in vivo, pulling of polymers in single-molecule experiments, etc, call for new class of experiments to monitor the noise signals during these events.

4.1.1 Outline

This chapter is organized as follows: In Sec. 4.2, we recapitulate the work theorem, introduce the paths and discuss the connection between the work theorem and the histogram transformation of equilibrium statistical mechanics. In Sec. 4.3 we give

a simple and general, dynamics independent proof of the relation between the equilibrium probability distribution and the work done in nonequilibrium paths. This relation in some form is already known [21, 22] but our derivation allows us in generalizing the result to other cases involving temperature, interactions, etc. Sec. 4.4 deals with the main result of this chapter. There we prove the eigenvalue equation for \mathcal{S} . A few examples are also given there. How to get the operator \mathcal{S} directly from experimental measurements of Barkhausen noise is also discussed here. Numerical verifications of some of the results are presented in Sec. 4.5 by taking the $2D$ Ising model as an example. We summarize in Sec. 4.6.

4.2 Work theorem and path integral

4.2.1 Work theorem

Consider a classical system described by a Hamiltonian $H(\Lambda, x)$ where Λ is an external field that couples to its conjugate, a microscopically defined quantity, x . The thermodynamic state is specified by temperature T and field Λ . Let us start with the system at $\Lambda = 0$ in thermal equilibrium at temperature T . External field Λ is changed in some given way from 0 to a final value λ in a finite time τ or in a finite number of steps n , letting the system evolve in contact with the heat reservoir. No attempt is made to ensure equilibrium during the process. The variation of x along the nonequilibrium path ($x(t)$ vs t) and the instantaneous final (boundary of the path) value of x , x_b , when the field reaches λ , are noted. The work done along a nonequilibrium path by the external source (as in Ref. [20]) is

$$W = \int_0^\tau \frac{\partial H}{\partial \Lambda} \frac{d\Lambda}{dt} dt, \quad (4.1)$$

in time τ , and it varies from path to path. The difference between two definitions of work in the context of work theorem, one used in Ref. [19] and the other in Ref. [20], is discussed in Ref. [37]. For the sake of notational simplicity we choose,

$$H = H_0 + H_1(\Lambda, x) = H_0 - \Lambda x, \quad (4.2)$$

where H_0 is the energy for $\Lambda = 0$. There is not much loss of generality in choosing the form of Eq.(4.2) because Λ and x refer to any pair of conjugate variables so that x itself need not be a linear function of the internal coordinates. As an example, in an interacting spin problem in a magnetic field h ($\equiv \Lambda$), $H = H_0 - h \sum_k s_k$ where s_k is the spin variable at a site denoted by k , with $x = \sum_k s_k$. Often Λ can be taken as the switching parameter to turn on a perturbation or interaction in a Hamiltonian $H = H_0 - H'$ with $H_\Lambda = H_0 - \Lambda H'$.

The work theorem [19, 20] provides the equilibrium free energy difference ΔF between the two states with $\Lambda = 0$ and $\Lambda = \lambda$, both at inverse temperature $\beta = 1/k_B T$ (k_B is the Boltzmann constant), from the nonequilibrium work done as

$$\Delta F = -\frac{1}{\beta} \ln \langle e^{-\beta W} \rangle, \quad (4.3)$$

where $\langle \dots \rangle$ denotes the average over all possible paths.

4.2.2 Paths: equilibrium and nonequilibrium

We are using here a description of a state by the intensive parameters which actually characterize the surroundings. In equilibrium any system is expected to have the values of the intensive parameters same as that of the environment. A change in any of the parameters, say Λ , from λ_0 to λ , would require heat and/or energy transfer. The work done on or by the system is determined by the change in the free energies, independent of the path of variation of the intensive parameters. This is expressed as

$$\Delta F = W_{\text{eq}} = - \int_{\lambda_0}^{\lambda} x_{\text{eq}}(\Lambda) d\Lambda, \quad (4.4)$$

where $\Delta F = F(\beta, \lambda) - F(\beta, \lambda_0)$. Here $x_{\text{eq}}(\Lambda) = \int x P_\Lambda(x) dx$ is the equilibrium average at the instantaneous values of the intensive parameters and $P_\Lambda(x)$ is the corresponding equilibrium probability distribution of x . This follows from the identification of the equilibrium value of x as $x_{\text{eq}} = -\partial F / \partial \Lambda$, in contrast to the conjugate ensemble definition $\Lambda = \partial \mathcal{F} / \partial x$ where $\mathcal{F}(\beta, x)$ is the fixed- x ensemble free energy.

For convenience, let us discretize the integrals. For example, for $\Lambda \in [\lambda_0, \lambda]$, we have a sequence $(\Lambda_0, \Lambda_1, \dots, \Lambda_n = \lambda)$ and the continuum is recovered by taking the usual limit of $n \rightarrow \infty$ with $\max\{\Delta\Lambda_i = \Lambda_{i+1} - \Lambda_i\} \rightarrow 0$. The work done can be

rewritten as

$$W_{eq} = - \sum_{i=0}^{n-1} \Delta\Lambda_i \left\{ \sum_x P_{\Lambda_i}(x)x \right\}. \quad (4.5)$$

By interchanging the sums over x and Λ , we define (i) a sequence $\{x_i|i = 0, \dots, n\}$ as instantaneous values, and (ii) a sequence-dependent work done as $W = \sum_i x_i \Delta\Lambda_i$, to reinterpret Eq. (4.5) as an average over these x_i 's. Therefore,

$$W_{eq} = - \sum_{\{x_i\}} \mathcal{P}\{x_i\} \sum_i x_i \Delta\Lambda_i, \quad (4.6)$$

where $\mathcal{P}\{x_i\} = \prod_i P_{\Lambda_i}(x_i)$ is the joint probability of getting the particular $\{x_i\}$ sequence, because, for a thermodynamic process, there is no memory. Going over to the continuum limit, the thermodynamic process of varying Λ is now seen as equivalent to choosing a path in the configuration space and re-weight the paths according to the probability of its occurrence in the Λ -ensemble. The relation between the free energy change and work, Eq. (4.4), now gets a path integral meaning where the process takes the system over the microstates and one averages the work over individual paths.

This thermodynamic connection is valid only in equilibrium. The work theorem generalizes this idea by replacing $\mathcal{P}\{x_i\}$ by the nonequilibrium probability of getting a path and asserting

$$e^{-\beta\Delta F} \equiv \frac{Z_\lambda}{Z_0} = \int \mathcal{D}\mathcal{X} e^{-\beta W}, \quad (4.7)$$

where $\int \mathcal{D}\mathcal{X}$ stands for the normalized sum over paths, i.e., sum over intermediate x 's with appropriate probabilities.

4.2.3 Histogram transformation and infinitely fast process

There is a fundamental transformation rule obeyed by the partition function, often used in numerical simulations as the histogram method [32]. This transformation connects the equilibrium probability distributions at two parameter values, $\Lambda = \lambda_0$ and $\Lambda = \lambda$ as

$$P_\lambda(x) = \frac{P_{\lambda_0}(x) e^{\beta(\lambda-\lambda_0)x}}{\sum_x P_{\lambda_0}(x) e^{\beta(\lambda-\lambda_0)x}}, \quad (4.8)$$

where the sum in the denominator is over the allowed values of x . The denominator of the right hand side of Eq.4.8 is Z_λ/Z_{λ_0} where Z_λ is the partition function at inverse temperature β ,

$$Z_\Lambda = \sum_{states} e^{-\beta H_0} e^{\beta \Lambda x}. \quad (4.9)$$

From Eq.(4.1), $(\lambda - \lambda_0)x$ can be taken as the work done in an instantaneous process that changes Λ from λ_0 to λ without changing x . The probability of getting x for equilibrium at λ_0 is $P_{\lambda_0}(x)$ and therefore the sum in the denominator of Eq.(4.8) is the path integral of Eq.(4.7), because x does not change. This gives the work theorem.

4.2.4 Work theorem and histogram method

Above the equivalence of the work theorem and a one step histogram transformation where the magnetic field has been changed from 0 to h in one step, has been shown. Similarly one can write the n -step histogram transformation which is representative of the actual process of doing the MC simulation to find out the free energy difference of initial and final states. Suppose initially we have zero magnetic field initially and at the final state magnetic field is h .

One step process: If the final state is reached from the initial state in one step, then change in magnetic field is, $\Delta h = h$. Hence the partition function at the magnetic field h is

$$Z_{\beta,h} = Z_{\beta,0} \sum_{E_0, M_0} P(E_0, M_0) e^{\beta \Delta h M_0}, \quad (4.10)$$

where E_0 and M_0 are the initial state energy and magnetization.

Two step process: The change in magnetic field while going from one state to the next is $\Delta h = h/2$ and hence $Z_{\beta,h}$ is

$$Z_{\beta,h} = Z_{\beta,h/2} \sum_{E_1, M_1} P_1(E_1, M_1) e^{\beta \Delta h M_1} \quad (4.11)$$

$$= Z_{\beta,0} \sum_{E_0, M_0} P_0(E_0, M_0) e^{\beta \Delta h M_0} \sum_{E_1, M_1} P_1(E_1, M_1) e^{\beta \Delta h M_1}. \quad (4.12)$$

Similarly for an n -step process $\Delta h = h/n$ and $Z_{\beta,h}$ is

$$Z_{\beta,h} = Z_{\beta,0} \sum_{E_0, M_0} P_0(E_0, M_0) e^{\beta \Delta h M_0} \times \sum_{E_1, M_1} P_1(E_1, M_1) e^{\beta \Delta h M_1} \dots \sum_{E_n, M_n} P_n(E_n, M_n) e^{\beta \Delta h M_n} \quad (4.13)$$

$$= Z_{\beta,0} \prod_{i=0}^{n-1} \sum_{E_i, M_i} P_i(E_i, M_i) e^{\beta \Delta h M_i}. \quad (4.14)$$

For the two extreme cases, the infinitely fast and the infinitely slow processes, it follows immediately that the histogram transformation gives back the work theorem. For a process which is infinitely fast, or with a strong memory, one can take the probability distribution of the intermediate i -th state, $P_i(E_i, M_i)$, as delta function, $\delta_{E_0, E_i} \delta_{M_0, M_i}$. This gives

$$Z_{\beta,h} = \sum_{E_0, M_0} P_0(E_0, M_0) e^{\beta n \Delta h M_0} = \sum_{E_0, M_0} P_0(E_0, M_0) e^{\beta h M_0}, \quad (4.15)$$

which is the same as that of the 1-step process. For an infinitely slow process, at each step $P_i(E_i, M_i)$ is the equilibrium distribution $P_i^{eq}(E_i, M_i)$ at the corresponding magnetic field, $h_i = i \Delta h$.

This connection of the work theorem with the histogram method can be used to make general constraints/comments on the probability distributions $P(E, M)$ which will be applicable to any problem, as the histogram method is independent of any specific problem.

We see that in the histogram transformation there is no need to keep track of energy E in the probability distribution, $P(M)$ is sufficient. Again the distribution of magnetization depends on the magnetization of the previous state if it is not an equilibrium state. So we replace $P(E_i, M_i)$ by $P(M_i | M_{i-1})$. Hence

$$Z_{\beta,h} = Z_{\beta,0} \prod_{i=0}^{n-1} \sum_{M_i} P_i(M_i | M_{i-1}) e^{\beta \Delta h M_i}. \quad (4.16)$$

According to this method, once the initial and final values of the switching parameter are decided, one gets the same free energy difference independent of the number of steps in between the initial and the final states. In other words, the re-

sult is the same for all n -step processes with any positive integer n . So, comparing a one step process and a two step process we can write,

$$\sum_{M_1} P(M_1|M_0)e^{\beta h M_1} = e^{\beta h M_0}. \quad (4.17)$$

4.3 Equilibrium probability distribution

We in this section use the discrete version of the process to re-derive the equilibrium probability distribution from the work theorem in a general and dynamics independent way. For the kind of nonequilibrium processes mentioned in Sec. 4.2.2 the equilibrium probability distribution of x at a parameter value λ can be obtained from a weighted path integral [22, 21]

$$P_\lambda(x) = \frac{\int \mathcal{D}\mathcal{X} e^{-\beta W} \delta(x_b - x)}{\int \mathcal{D}\mathcal{X} e^{-\beta W}}, \quad (4.18)$$

where x_b is the instantaneous boundary value at the end of the path, and the denominator is same as r.h.s. of Eq.(4.7). This is in the form of a path integral where the paths are weighted by a Boltzmann-like factor $\exp(-\beta W)$. The same was established previously in specific cases like, the Master equation approach [20], the Feynman-Kac formula [21] and Monte Carlo dynamics [22].

The equilibrium average x_{eq} is defined as

$$x_{\text{eq}} = \frac{1}{\beta} \frac{\partial}{\partial \Lambda} \ln Z_\Lambda = \lim_{\delta \rightarrow 0} \left(\beta \frac{Z_\Lambda}{Z_0} \right)^{-1} \frac{1}{\delta} \left(\frac{Z_\Lambda}{Z_0} - \frac{Z_{\Lambda-\delta}}{Z_0} \right), \quad (4.19)$$

where work theorem is to be used for the partition functions.

The system starts in equilibrium at temperature T and $\Lambda = 0$, and then Λ is built up at constant T as a sequence of infinitely fast jump of $\Delta\lambda = \lambda/n$, each jump followed by a finite time evolution in contact with the heat bath. Consider now two n -step processes, one process with final field λ and another one with $\lambda - \delta$ ($\delta \rightarrow 0$ at the end). In fact, the second process is just a copy (replica) of the first one in every respect except at the last stage (Fig. 4.1). For the last jump, the change in Λ for replica 1 is $\Delta\lambda$ while for replica 2 it is $\Delta\lambda - \delta$.

A path is specified or defined by the sequence $\{x_i \mid i = 0, \dots, n-1\}$. The

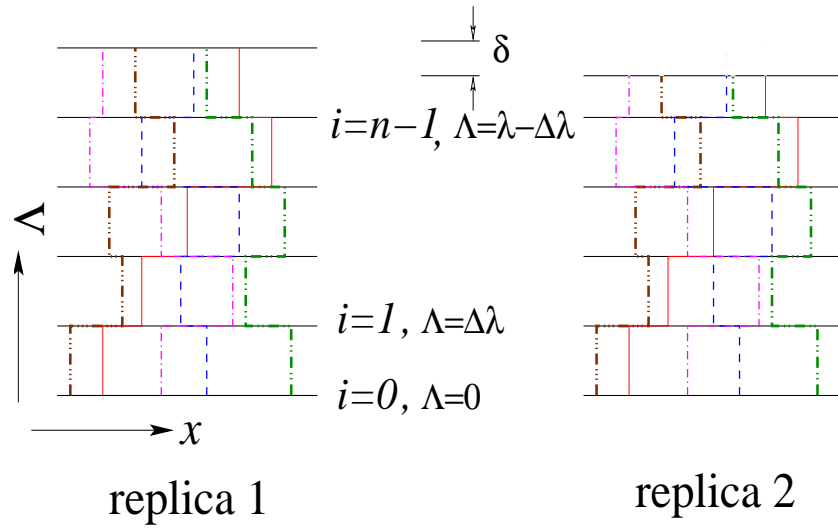


Figure 4.1: Schematic representation of two replicas of same paths, each starting from $\Lambda = 0$ and ending at $\Lambda = \lambda$ in replica 1 and at $\Lambda = \lambda - \delta$ in replica 2. Label i denotes the step number as Λ is changed in steps of λ/n . Lines of different styles (dashed, dotted etc) represent different realizations of paths starting from different values of x . The vertical portion of a path is an instantaneous process (no change in x) and the horizontal part is under interaction with the surrounding (x evolves at a constant Λ). Identically shaded lines in the two replicas have the same evolution.

changes in x_i at any step is because of internal dynamics or exchange of heat with the external reservoirs. We do not need to let the system evolve once the field reaches the final desired value. Therefore, the sequence $\{x_i \mid i = 0 \dots n - 1\}$ is the same for both the replicas. The work done W_1, W_2 along an n -step nonequilibrium path for replicas 1, 2 are related via

$$W_2 = W_1 + \delta x_{n-1}, \quad (4.20)$$

with W_1 is of the form given above Eq. (4.6). The work theorem of Eq. (4.7) when used in Eq.(4.19) yields

$$\begin{aligned} x_{\text{eq}} &= \lim_{\delta \rightarrow 0} \frac{1}{\beta \sum_{\text{paths}} e^{\beta \sum_{i=0}^{n-1} \Delta \Lambda_i x_i}} \frac{\sum_{\text{paths}} e^{\beta \sum_{i=0}^{n-1} \Delta \Lambda_i x_i} (1 - e^{-\beta \delta x_{n-1}})}{\delta} \\ &= \frac{\int \mathcal{D}\mathcal{X} x_b e^{-\beta W}}{\int \mathcal{D}\mathcal{X} e^{-\beta W}}, \quad (x_b \equiv x_{n-1}). \end{aligned} \quad (4.21)$$

This shows that the equilibrium average can be expressed in terms of the boundary value with proper weightage of the paths. The above proof can be generalized to any moments of x .

Now if $\mathcal{P}(x)$ is the distribution of x_b , that gives the average in Eq.(4.21)

$$x_{\text{eq}} = \langle x \rangle = \int x \mathcal{P}(x) dx, \quad (4.22)$$

then $\mathcal{P}(x)$ can be written as

$$\mathcal{P}(x) = \frac{\int \mathcal{D}\mathcal{X} e^{-\beta W} \delta(x_b - x)}{\int \mathcal{D}\mathcal{X} e^{-\beta W}}, \quad (4.23)$$

as quoted in Eq.(4.18). We now invoke the moment theorem [96] which, in our case, states that for a probability distribution without sufficiently long tails, the moments uniquely specify the distribution. Since these conditions are satisfied by the equilibrium probability distributions for any finite system, the moment theorem applies. Since the moments from the nonequilibrium path integral are the equilibrium moments, $\mathcal{P}(x)$ is the equilibrium distribution: $\mathcal{P}(x) = P_\lambda(x)$. This completes the proof.

4.3.1 Generalization

In general, for a Hamiltonian of the form $H = H(\{\Lambda_\alpha\}, \{X_\alpha\})$, the equilibrium distribution, $P(E, x_1, x_2, \dots)$, at some given parameter values, $\{\lambda_\alpha\}$ and temperature β^{-1} , can be obtained in the same way provided the paths start from an equilibrium state for $H = H_0$, where H_0 gives the energy for all $\Lambda_\alpha = 0$ and W is the total work done on the system along a nonequilibrium path, by each of the externally controlled parameters. E here corresponds to the energy from H_0 only. Our starting H_0 may be a free Hamiltonian for a mechanical system and *can as well be zero* for interacting spin-like systems.

Consider the Hamiltonian $H = \gamma H_0$ for a spin-like system (i.e. without any kinetic energy). In this case one of the $\{\Lambda_\alpha\}$ could be the strength of interaction. Let's start with $\gamma = 0$, i.e. the starting point is any random configuration of the free system or a non-interacting system, and then change γ in some given way from $\gamma = 0$ to $\gamma = 1$. We thus generate the equilibrium distribution of H_0 at a particular β , by doing a similar nonequilibrium path averaging. Note that everywhere we need the product βW . So, we can discretize temperature instead of Λ and the process can be reinterpreted as cooling down to a finite temperature from an initial infinite temperature. In the usual formulation of work theorem, Λ refers to mechanical parameters such as the pulling force in AFM, which are under direct control of the experimentalists. In contrast, other intensive parameters such as temperature may not be controlled with this level of precision in experiments. But this finds various applications in numerical experiments. Such thermal quenches are quite common in numerical simulations and our results show how these can be harnessed to extract equilibrium information as well. The ensemble of states obtained in the above discussed way at the end of the path is *not* a representative sample of the equilibrium ensemble at the concerned temperature and field. However, the history-averaged distribution is the equilibrium distribution. The boundary states would relax to reach equilibrium via energy transfer to the reservoirs but that part of the process is not required. This difference becomes important and visible in systems exhibiting hysteresis as e.g. for a ferromagnet.

4.3.2 Application to ferromagnet to get equilibrium magnetization curve

The above-mentioned scheme can be used to get the equilibrium probability distribution or thermodynamic quantity from a process which is arbitrarily away from equilibrium and at all temperatures including phase transition points. Now we apply our result to the case of hysteresis of a ferromagnet below the critical temperature (T_C). Consider a Hamiltonian: $H = H_0 - hM$. The external magnetic field is varied from $-h_0$ to $+h_0$ in a fixed manner and then reversed. $\langle M \rangle$ is calculated using Eq.(4.21). Below the critical temperature, magnetization (M) vs. magnetic field (h) curve shows a discontinuity at $h = 0$ for infinite system size. For a finite system there is no discontinuity, M - h curve is continuous passing through the origin, and the slope of M - h curve at $h = 0$ increases as system size increases. But, in reality, when experiments or simulations are done, instead of single retraceable curve passing through the origin we get a loop called hysteresis loop, no matter how slowly we vary the magnetic field. The common technique known to get the equilibrium curve is to connect the vertices of the sub-loops [95]. Here the weighted nonequilibrium path integral scheme is a way out to get the equilibrium magnetization curve. We verify this for Ising ferromagnet and discuss the observations about it in Sec. 4.5.

4.4 Equilibrium probability distribution from an eigenvalue equation: Operator \mathcal{S}

In this section we derive the main result of this chapter: equilibrium probability distribution as an eigenfunction of a nonequilibrium operator \mathcal{S} .

Using the discrete notation, we can write Eq.(4.18) as

$$P_\lambda(x) = \frac{Z_{\lambda_0}}{Z_\lambda} \sum_{\text{paths}} e^{-\beta W} \delta_{x_b, x} , \quad (4.24)$$

by using the work theorem, Eq.(4.3), that

$$\sum_{\text{paths}} e^{-\beta W} = \frac{Z_\lambda}{Z_{\lambda_0}}. \quad (4.25)$$

Again, writing $\sum_{\text{paths}} = \sum_{x_i} P_{\lambda_0}(x_i) \sum'_{\text{paths}}$, where the primed summation denotes the sum for fixed initial value of $x = x_i$ with appropriate probability and $P_{\lambda_0}(x_i)$ denotes the equilibrium distribution of x_i for $\Lambda = \lambda_0$, we get,

$$P_\lambda(x) = \frac{Z_{\lambda_0}}{Z_\lambda} \sum_{x_i} \sum'_{\text{paths}} P_{\lambda_0}(x_i) e^{-\beta W} \delta_{x_b, x}. \quad (4.26)$$

Use the transformation rule for the partition function (Sec. 4.2.3),

$$\frac{Z_\lambda}{Z_{\lambda_0}} = \sum_x P_{\lambda_0}(x) e^{\beta(\lambda - \lambda_0)x}, \quad (4.27)$$

to absorb Z_{λ_0}/Z_λ into the probability distribution. This transforms $P_{\lambda_0}(x_i)$ into $P_\lambda(x_i)$, in Eq.(4.26) as

$$P_\lambda(x) = \sum_{x_i} \sum'_{\text{paths}} e^{-\beta W - \beta(\lambda - \lambda_0)x_i} \delta_{x_b, x} P_\lambda(x_i) \quad (4.28)$$

$$= \sum_{x_i} \mathcal{S}_{x, x_i} P_\lambda(x_i), \quad (4.29)$$

$$\Rightarrow \mathcal{S} \mathbb{P}_\lambda = \mathbb{P}_\lambda, \quad (4.30)$$

with \mathbb{P}_λ as a column vector of $\{P_\lambda(x)\}$ and the matrix elements of \mathcal{S} as

$$\mathcal{S}_{x_f, x_i} = \sum'_{\text{paths}} e^{-\beta W - \beta(\lambda - \lambda_0)x_i}. \quad (4.31)$$

The summation in Eq.(4.31) is over all paths that start from an equilibrium distribution of $\Lambda = \lambda_0$ with value of x as x_i and end in a state with $\Lambda = \lambda$ and $x = x_f$, with proper normalization (denoted by prime).

Although we use the simple Hamiltonian: $H = H_0 - \Lambda x$ in the construction, Eq.4.31 can be generalized for a Hamiltonian $H = H + H_1(\Lambda, x)$, because Eq.(4.27)

has the general form,

$$\frac{Z_\lambda}{Z_{\lambda_0}} = \sum_x P_{\lambda_0}(x) e^{-\beta [H(\lambda,x) - H(\lambda_0,x)]}.$$

Now we address the remaining problem – the normalization of the primed summation over paths in Eq.(4.31). This problem is inherited from Eq.(4.25). Note that the l.h.s. of Eq. 4.25 should add up to 1 for $\lambda = \lambda_0$ with $W = 0$. So we choose the hidden factor *a posteriori* by demanding proper normalization of the final probability distribution. This condition can be ensured in a process- or system-independent way by choosing $\sum_x \mathcal{S}_{x,x_i} = f(x_i) = 1$, (Eq.(4.29)), i.e. by making the column sum of \mathcal{S} independent of x_i . By this normalization of the sum of each column to unity it is also guaranteed that the principal eigenvalue is 1. The corresponding right principal eigenvector has all the elements real and non-negative – a necessary condition to be a probability distribution and when normalized, such that sum of all elements is unity, this eigenvector gives the equilibrium probability distribution.

The number of rows and columns in \mathcal{S} is determined by the number of allowed values of x . For continuum of states, the matrix equation is to be replaced by an integral eigenvalue equation.

Hence, in brief, the scheme to get the equilibrium distribution at some parameter value λ and temperature β^{-1} is as follows: Pre-fix some arbitrary or convenient-to-start-with initial parameter value λ_0 which will be same for all paths/experiments. Choose a microstate from the equilibrium distribution at field λ_0 and call its value of x as x_i . Change the parameter value from λ_0 to λ in some predetermined way and measure the work done by the external parameter on the system according to Eq.(4.1). Repeat the experiments several times and construct the matrix \mathcal{S} using Eq.(4.31). Next, each column of the matrix is normalized to unity. The normalized principal eigen-vector is the equilibrium probability distribution, $P_\lambda(x)$, at the field λ .

Eq.(4.30) is the main result of this chapter and it is not restricted to one external parameter only and can be generalized to any parameter as mentioned above. The matrix \mathcal{S} connects any two allowed states of the system without any reference to equilibrium anywhere and yet its principal eigen-vector determines

the equilibrium distribution. Despite resemblance, there is no similarity either with the stochastic matrix of a Markov process or the adiabatic switching on of interaction in a quantum system because \mathcal{S} is constructed out of a finite process and needs global information about the work done.

Another issue that comes up in this approach via \mathcal{S} , is the question of ergodicity which connects the Gibbsian statistical mechanics with equilibrium thermodynamics. The nonequilibrium dynamics used to construct \mathcal{S} may not respect ergodicity but the starting points for the paths in principle span the whole phase space, even in the case when one starts with a free non-interacting system. It seems ergodicity of the free non-interacting system is sufficient to generate the equilibrium distribution.

4.4.1 Examples

Example 1: Extreme cases

Consider an extreme case: a completely equilibrium evolution of the system, where at each step the system reaches its equilibrium. Take a simple system: a single spin problem in magnetic field h and temperature β^{-1} : $\beta H = -Ks$, where $s = \pm 1$ and $K = \beta h$. For an n -step process, K varies from 0 to nk in steps of k , and the column normalized \mathcal{S} matrix can be calculated exactly where at each step the spin reaches the corresponding equilibrium state, as

$$\mathcal{S} = \begin{pmatrix} P_{nk}(+) & P_{nk}(+) \\ P_{nk}(-) & P_{nk}(-) \end{pmatrix}, \quad (4.32)$$

where $P_{nk}(\pm)$ is the equilibrium probability of finding ± 1 spin at the n -th step. Thus for a completely equilibrium evolution of the system the elements of the matrix \mathcal{S} are unique and, therefore, \mathcal{S} has only one and unique eigenvector. In that case principal eigenvalue is 1 and all other eigenvalues are zero. We may conclude that a complete reducibility of \mathcal{S} is the signature of a thermodynamic process.

Eq.(4.32) is to be compared with the extreme nonequilibrium process as embodied in Eq.(4.8). For this instantaneous change in λ , $\mathcal{S} = \mathbb{I}$, the identity matrix, with no zero eigenvalues.

If at each of these n steps, the system evolves for a time Δt in contact with the bath, then $\mathcal{S}_{n,\Delta t} \rightarrow \mathcal{S}_{eq}$ as $\Delta t \rightarrow \infty$. The smallness of the rest of the eigenvalues would indicate how close to equilibrium the system is.

The dynamics of a many body system might be compartmentalized into slow modes and fast modes, where the fast modes would equilibrate much more quickly than slow ones. How many such fast modes have actually equilibrated, can be gauged by the number of zero eigenvalues. The \mathcal{S} matrix is not necessarily symmetric, though real and there is a possibility of pairs of complex conjugate eigenvalues, with their magnitudes going to zero as equilibrium is reached.

Example 2: Barkhausen noise and matrix \mathcal{S}

We now show the practical feasibility of the operator method for a magnet by using the Barkhausen noise [94, 95] as recorded through the output voltage across a secondary coil wound around a ferromagnetic material. Though Barkhausen noise has seen many applications, its use for equilibrium properties has not been anticipated.

Consider the Hamiltonian

$$H = H_0 - h M. \quad (4.33)$$

Here magnetic field h and magnetization M correspond to Λ and x respectively. The field is varied from h_i to h_f in a time interval τ at a constant rate \dot{h} . The Barkhausen effect is a noisy signal proportional to the change in magnetization, $\eta(t) = \frac{dM(t)}{dt}$. So by integrating the Barkhausen noise up to time t one gets the nonequilibrium instantaneous magnetization of the material. Therefore, we can write the work related exponent in Eq.(4.31) as

$$W + [h(\tau) - h(0)] M_i = -\dot{h} \int_0^\tau dt \int_0^t \eta(t') dt', \quad (4.34)$$

which, in a discretized form, looks like

$$W + [h_f - h_i] M_i = -\Delta h \sum_{j=1}^{n-1} \sum_{k=1}^j \eta_k, \quad (4.35)$$

where the Barkhausen noise at k -th step is $\eta_k = M_k - M_{k-1}$. Hence the matrix elements \mathcal{S}_{M_f, M_i} takes the form

$$\mathcal{S}_{M_f, M_i} = \sum'_{\text{expts.}} \exp \left[\beta \Delta h \sum_{j=1}^{n-1} \sum_{k=1}^j \eta_k \right], \quad (4.36)$$

expressed entirely in terms of the Barkhausen noise along the nonequilibrium paths. The primed summation over paths that start with M_i and end at M_f includes proper normalization as mentioned earlier.

To go to other cases, e.g., for the case of a polymer pulled at a constant rate of change of force, one needs to monitor the time variation of the pulled point displacement dx/dt vs t . This information can then be used in Eq.(4.36) to get the corresponding \mathcal{S} .

4.5 Numerical verification of results

Our claims about the probability have been verified for the case of $2D$ Ising model on a square lattice, $L \times L$, where L is the size of the lattice with periodic boundary condition. Consider the Hamiltonian

$$H = -J \sum_{\langle k, l \rangle} s_k s_l - h \sum_k s_k, \quad (4.37)$$

where J is the interaction strength, h is the external magnetic field and $s_k = \pm 1$ is the spin at k -th site of a square lattice. Here $\sum_{\langle k, l \rangle}$ denotes the sum over nearest neighbor spins. Here J and h play the roles of external parameter (Λ) and $\sum_{\langle k, l \rangle} s_k s_l$ and $\sum_k s_k$ are the internal variables (x).

We find equilibrium probability distribution for given J and h using weighted nonequilibrium path integral, normalizing the eigenfunction of \mathcal{S} and compare those with the equilibrium probability distribution obtained from a usual Monte Carlo procedure. The overlap of the two distributions is determined by the Bhattacharyya coefficient [97] defined as

$$BC = \sum_{E, M} \sqrt{P_h(E, M) P_{eq}(E, M)} = 1 - \epsilon, \quad (4.38)$$

with $BC = 0$ for no overlap and $BC = 1$ for complete overlap.

The practical implementation is done as follows.

1. Consider an $L \times L$ square lattice with periodic boundary condition.
2. Start with $h = 0$. Take an arbitrary spin configuration. Let the Ising spin system evolve and equilibrate with the heat bath at $\beta = 1/T$, employing the Metropolis algorithm. In other words, this is a microstate, C_0 , randomly sampled from an equilibrium canonical ensemble. Let E_0 be its energy and M_0 be its magnetization. Then call the equilibrium distribution at temperature T for $h = 0$ as $P_{\beta,0}^{(0)}(E_0, M_0)$.
3. *Work step:* Switch the magnetic field: $h \rightarrow h + \Delta h$, keeping the the microstate same as C_0 . Calculate the energy of C_0 with field $h + \Delta h$ and let it be E_1 . Work done on the system equals $E_1 - E_0 = -M_0 \Delta h$.
4. *Heat step:* Carry out a few Monte Carlo sweeps with field $h + \Delta h$ on. It takes the system towards the equilibrium at field $h + \Delta h$ and temperature T . Let the system after the heat step be in microstate C_1 .
5. Next the work step and the heat step, (3) and (4) are continued alternately until the magnetic field reaches the predefined value. Thus alternate work step (in which the microstate does not change but the field changes) - and the heat step (in which system switches from one microstate to another in the presence of the increased external field) is the switching protocol. This whole process starting from step (2) constitutes one experiment.
6. The experiment of step (5) is carried out several times and an ensemble of work values are constructed. Thus one gets the work distribution $P(W)$.

4.5.1 Numerical verification of the equilibrium probability distribution starting from a uniform distribution

Let us take an 8×8 lattice and start from $H = 0$. Each time we start from a state chosen from a uniform distribution and reach the final state with $J = 1$ and $h = 1$ in n -steps. At each i -th step, J is switched from J_i to J_{i+1} and the external

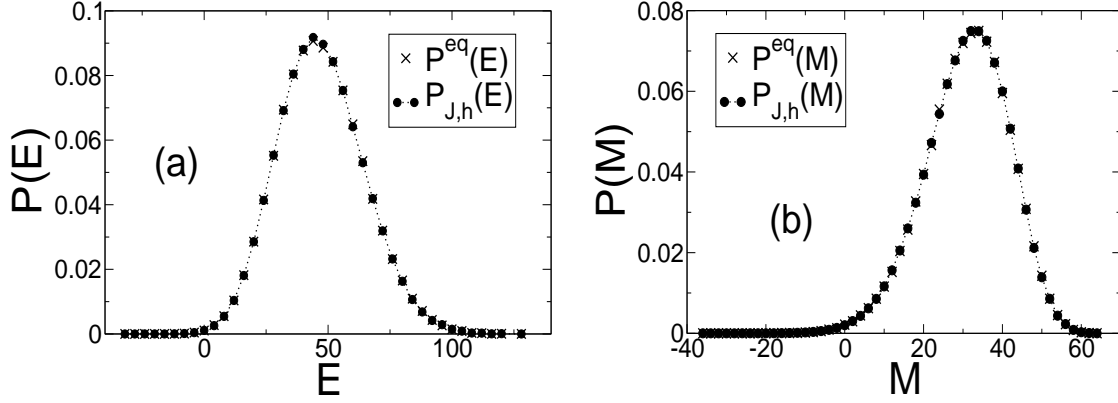


Figure 4.2: Plot of the weighted distribution (a) $P_{J,h}(E)$ vs. E and (b) $P_{J,h}(M)$ vs. M (dotted line with circles) for varying J and h with $n = 20$ and equilibrium distributions $P_{eq}(E)$ and $P_{eq}(M)$ (crosses) with $J = 1$, $h = 1$ and $\beta = 0.2$ for a 8×8 lattice, showing that $P_{J,h}(E) = P_{eq}(E)$ and $P_{J,h}(M) = P_{eq}(M)$.

magnetic field from h_i to h_{i+1} ,

$$\Delta J = J_{i+1} - J_i = J/n \quad \text{and} \quad \Delta h_i = h_{i+1} - h_i = h/n;$$

keeping the spin configuration unchanged, and the amount of work done on the system

$$W_i = -\Delta J_i E_i - \Delta h_i M_i,$$

is calculated where M_i is the magnetization and E_i is $\sum s_k s_l$ at the i -th step. Then we let the system relax at that field h_i , J_i and β for a while, but do not equilibrate. Thus the work along a path consisting of n steps is

$$W = -\sum_{i=0}^{n-1} \Delta J_i E_i + \Delta h_i M_i,$$

which is different for different paths. We find the weighted distribution

$$P_{J,h}(E, M) = \frac{\int \mathcal{D}\mathcal{X} e^{-\beta W} \delta(E_b - E) \delta(M_b - M)}{\int \mathcal{D}\mathcal{X} e^{-\beta W}}, \quad (4.39)$$

and then

$$P_{J,h}(M) = \sum_E P(E, M)$$

and

$$P_{J,h}(E) = \sum_M P(E, M).$$

It is observed that these distributions merge well with the corresponding equilibrium distributions and for $P_{J,h}(E)$ (Fig. 4.2(a)) and $P_{J,h}(M)$ (Fig. 4.2(b)) we get $\epsilon \sim 10^{-3}$ (Eq.(4.38)).

4.5.2 Equilibrium magnetization curve using nonequilibrium path integral

For this case lattice size is 8×8 and the interaction strength is kept fixed at $J = 1$. Each time we start from an equilibrium distribution of $h = -h_0$. The field is varied from $-h_0$ to $+h_0$ in n steps. $W(n)$ vs. n data are recorded and $\langle M \rangle(h)$ is calculated using Eq.(4.21).

We plot the weight averaged magnetization curve, $\langle M \rangle(h)$, along with the hysteresis loop, average magnetization over samples, against h for $h_0 = 0.2$ in Fig. 4.3(a) and $h_0 = 2$ in Fig. 4.3(b).

A retracable equilibrium curve is obtained as expected though the nominally averaged magnetization neither changes sign nor makes a complete loop (Fig. 4.3(a)) [89]. This reflects the fact that though in majority the magnetization does not reach the correct value, there are a few rare samples for which the spins do flip and these rare configurations, which are close to equilibrium, get more weight in the weighted path integral to give the correct equilibrium curve.

For the larger field, we obtain a curve which is much narrower than the hysteresis curve (Fig. 4.3b). The equilibrium curve obtained this way is still not a single curve. The width of the loop might be connected to the droplet time scale, and signals the need for a more careful sum over paths to take care of droplet fluctuations.

4.5.3 Numerical verification of the eigenvalue equation

We start from an equilibrium ensemble at inverse temperature $\beta = 0.2$ (kept fixed throughout the experiment), $J = 1$ and $h = 0$. Each time we start from a state chosen from its equilibrium distribution and reach the final state with $J = 1$ and

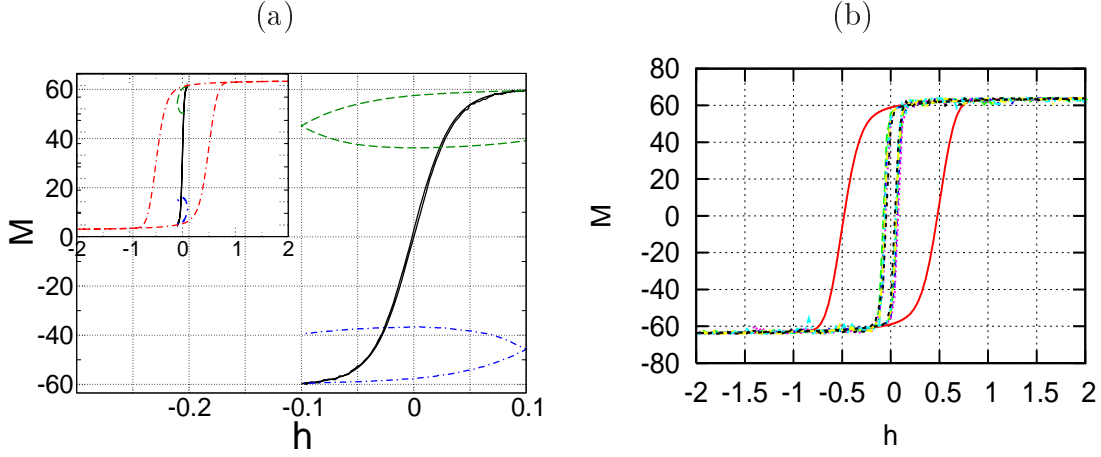


Figure 4.3: Plot of weighted average $M(h)$ vs. h and the corresponding hysteresis loop (simple averaged M vs. h) for a 8×8 lattice. The magnetic field varies from $-h_0$ to $+h_0$ in 100 steps. (a) $h_0 = 0.1$. The weighted loop and the hysteresis loops are represented by the black solid line and the green and blue dashed lines. The inset shows the hysteresis loop for the small (green and blue lines) field with respect to the large field (red double dash-dotted line) and the weight averaged magnetization for small field. (b) $h_0 = 2$. The weighted loop and the hysteresis loops are represented by the dashed lines and the red solid line respectively.

$h = 1$ in n -steps in the same way described above and calculate the amount of work on the system at i -th step: $W_i = -\Delta h_i M_i$. We find the matrix elements:

$$\mathcal{S}_{M_f, M_i} = \sum'_{\text{paths}} e^{-\beta W - \beta(h-h_0)M_i} \delta_{M_b, M_f}. \quad (4.40)$$

After the matrix is constructed, we normalize sum of each column to unity and find the normalized principal eigen-vector corresponding to the Principal eigenvalue 1, which is guaranteed. We compare the normalized eigenfunction with the actual equilibrium distribution for $L = 4$ and 8. We see that these distributions merge with the corresponding equilibrium distributions for $L = 4$ (Fig. 4.4(a)) and $L = 8$ (Fig. 4.4(b)) with $\epsilon \sim 10^{-4}$ (Eq.(4.38)).

4.6 Summary

In this chapter we show and verify numerically that the repeated nonequilibrium measurements of work done to connect any two microstates of a system can be used

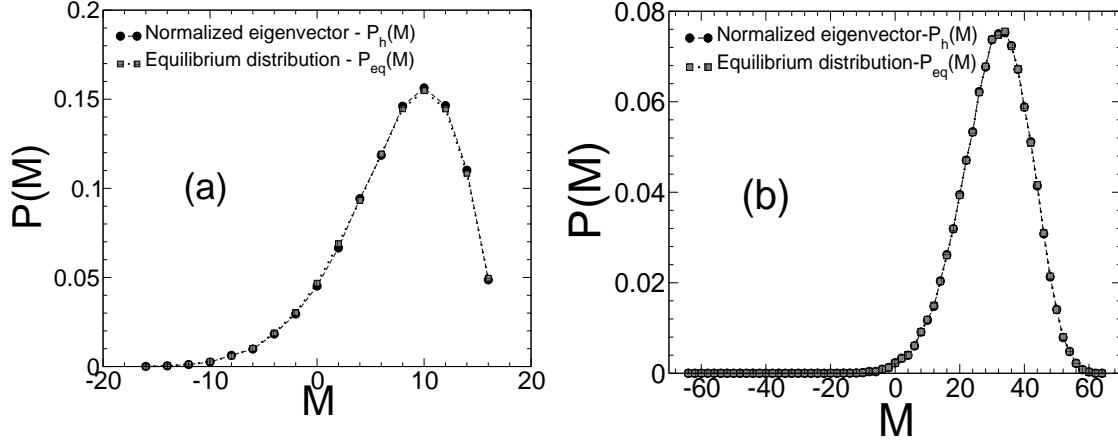


Figure 4.4: Plot of the equilibrium distribution $P_{eq}(M)$ vs. M (boxes with dotted line) and normalized principal eigen-vector $P_h(M)$ (dashed line with circles) with $J = 1$, $h = 1$, $\beta = 0.2$ and $n = 1000$ for (a) 4×4 lattice and (b) 8×8 lattice, showing that $P_h(M) = P_{eq}(M)$, i.e., eigenfunction is indeed an equilibrium distribution.

to construct a matrix \mathcal{S} whose principal eigenvector is the equilibrium distribution. The matrix elements of \mathcal{S} (Eq.(4.31)) for a Hamiltonian $H(\Lambda, x)$ with (Λ, x) as a conjugate pair are:

$$\mathcal{S}_{x_f, x_i} = \sum'_{\text{paths}} e^{-\beta W + \beta[H(\lambda, x_i) - H(\lambda_0, x_i)]} \quad (4.41)$$

where the summation is over all paths that start from an equilibrium distribution of externally controlled parameter $\Lambda = \lambda_0$ with value of conjugate variable x as x_i and end in a state with $\Lambda = \lambda$ and $x = x_f$, with proper normalization. The work done W is defined in Eq.(4.1). The values of the elements of \mathcal{S} depend on the details of the process and, therefore, there can be many different \mathcal{S} , but all will have the same invariant principal eigenvector. In this way the distribution of an interacting system can be obtained from a free, non-interacting one without any reference to equilibrium anywhere. In the process, we also provide a dynamics independent proof of the result that the equilibrium probability distribution can be obtained using the nonequilibrium path integral. Besides giving a new perspective of thermodynamics and statistical mechanics, our result has direct implications for new ways in numerical simulations and experiments.

What next: Now we study the equilibrium phase transition of a DNA by

mapping to an equivalent quantum problem. The phase transition is then observed through the problem of dissociation of two interacting quantum particles. To study the quantum phase transition we make use of the quantum entanglement entropy, mainly the von Neumann entropy. The special behaviours of the phase transition are shown to be same for the classical polymer problem and the problem of quantum dissociation.

List of symbols

β	Inverse temperature
E	Energy
\mathcal{F}	Fixed x ensemble free energy
ΔF	Free energy difference
H_0	Hamiltonian under no drive
H	Hamiltonian
h	Magnetic field
Λ	Intensive variable, control parameter
M	Magnetization
n	Number of steps to reach final state from the initial one
\mathcal{P}	Equilibrium probability distribution
$P_\Lambda(x)$	Equilibrium probability distribution of x at λ
P	Probability distribution
\mathcal{S}	Matrix constructed from nonequilibrium work done
W_{eq}	Equilibrium work done
W	Work done
x_b	Value of x at work step
x_{eq}	Equilibrium value of x
x	Extensive variable
Z_Λ	Partition function at Λ

5

Entanglement entropy of a quantum unbinding transition and entropy of DNA

In this chapter, we use the ideas and the results of DNA phase transition in a different way to study the dissociation of a quantum molecule. The quantum dissociation of a bound pair is a quantum phase transition characterized by diverging length scales. This QPT is traced by the quantum entanglement entropy, a measure of pure quantum correlation. We show that the quantum entanglement entropy captures the important features of the phase transition. Moreover, some interesting characteristics of the entanglement entropy is revealed, which is then justified from the known results of the DNA.

5.1 Introduction

At or near a QCP, the signatures of its universality can be found in the entanglement, a common measure of which is the von Neumann entropy (S^{vN}) [36, 39, 45, 44, 98, 99]. The exact results of this chapter show that for a class of critical points, viz., the dissociation of a pair of particles in the unitarity limit of infinite scattering length, there is the possibility of a negatively diverging S^{vN} . Although counter-intuitive, this is not an artifact. Analogous situation occurs in statistical mechanics for Gibbs entropy in canonical ensemble for a gapless spectrum. As discussed below, the problem in hand involves a gapless entanglement spectrum. The usual proof of the positivity of entanglement entropy is not applicable in case of continuous eigenvalues of the reduced density matrix. The negative

entropy is essential for the criticality itself. Its importance is brought out via the mapping of the quantum problem to the equivalent classical statistical mechanical problem, the melting of a double-stranded DNA [100, 101, 102, 107].

5.1.1 Outline

The outline of the chapter is as follows. We analytically find out the von Neumann entropy of two interacting particles in Sec. 5.2 and in the next section, Sec.5.3, we explain how the entanglement entropy is related to the entropy of bubbles in DNA melting.

5.2 Entanglement entropy

Recall the problem of a quantum particle of mass m in a three dimensional spherical potential well,

$$\begin{aligned} V(\mathbf{r}) &= -V_0 & \text{for } r < a, \\ &= 0 & \text{for } r > a, \end{aligned} \tag{5.1}$$

where r is the radial coordinate, a and V_0 are the width and the depth of the potential well. What is special is that $V_0 > 0$ does not guarantee the existence of a bound state, unlike in one or two dimensions, or in classical mechanics. No bound state exists for $u < u_c$ where $u = 2mV_0a^2/\hbar^2$ is the dimensionless parameter for the potential and u_c corresponds to a critical value of u . For simplicity, we take $u \approx u_c$ so that there is only one bound state. In this situation energy $|E|$ itself is the gap in the spectrum. If we tune u to get a state with zero energy ($E = 0$), then at that energy in $d = 3$ the wave function $\varphi(r) \sim 1/r$ which is like a non-normalizable critical state. Like a bound state the probability density does decay to zero but like an unbound state it is not normalizable. In higher dimensions, the condition for a minimal strength of the potential for a bound state remains true, but the state corresponding to $E = 0$ becomes normalizable as it should be for a bound state. So we see that this bound to unbound transition for a potential well has different nature in different dimensions. In general, (i) for $d \leq 2$ there is no such transition as $E = 0$ requires $V_0 = 0$, though there are remnants of the

transition as $V_0 \rightarrow 0$, (ii) for $2 < d < 4$, the transition is continuous (critical) — the bound state becomes unbound through a non-normalizable critical state as we change u , and, (iii) for $d > 4$, the bound state remains normalizable up to and including $E = 0$, and becomes unbound as u is decreased further, thus making the transition first-order. This depicts a QPT and the case of a potential well gives a simple example of a quantum critical point for $2 < d < 4$ with diverging length scales.

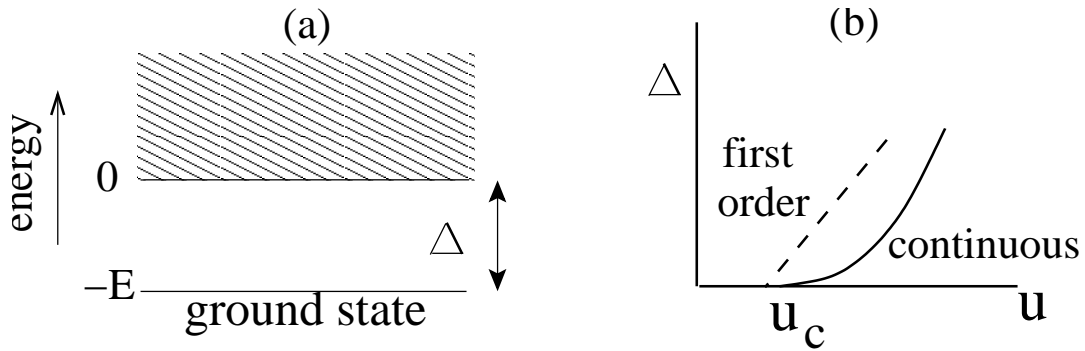


Figure 5.1: (a) Gap Δ in the energy spectrum. The shaded region is the continuum of energy. (b) The graph shows how energy gap goes to zero. The continuous line describes a second order or continuous transition (critical) and the dashed line shows the first order transition. The two are distinguished by the behaviour of the slope at $u = u_c$.

The ground state energy, for u close to u_c , is the gap Δ in the spectrum. A quantum phase transition is characterized by a vanishing gap. A discontinuity of the first derivative $d\Delta/du$ signals a first order transition, otherwise it is critical or continuous, as shown in Fig. 5.1. One may define characteristic time and length scales

$$\xi_{\parallel} = \hbar\Delta^{-1}, \text{ and } \xi_{\perp} = \hbar/\sqrt{2m\Delta}, \quad (5.2)$$

both of which diverge as $\Delta \rightarrow 0$, with $\xi_{\parallel} \sim \xi_{\perp}^z$, z ($= 2$ in this case) being the dynamic exponent. One may compare with the classical ground state to see the importance of quantum (zero-point) fluctuations and the importance of time or dynamics in quantum phase transitions. A path-integral interpretation of these scales, useful for the DNA mapping, is given below.

Let us now consider the ground state of two dissimilar particles interacting via a central potential $V(|\mathbf{r}_1 - \mathbf{r}_2|)$ of the type of Eq.(5.1), with \mathbf{r}_i denoting the co-

ordinate of the i -th particle. The existence of diverging length scales and scaling behavior around $u = u_c$ justifies the dissociation of the bound pair to be a QCP or a QPT depending on the dimensions they are in. The criticality is described by the exponents for the diverging length scales and the energy, as

$$|E| \sim \xi_{\parallel}^{-1} \sim |u - u_c|^{\nu_{\parallel}}, \text{ and } \xi_{\perp} \sim |u - u_c|^{-\nu_{\perp}}, \quad (5.3)$$

with

$$\nu_{\parallel} = z\nu_{\perp} = 1/(\Psi - 1), \text{ for } 1 < \Psi \leq 2, \quad (5.4)$$

$$= 1, \quad \text{for } \Psi \geq 2, \quad (5.5)$$

which involve (i) z the dynamic exponent, and (ii) a universal exponent Ψ , known as the reunion exponent for polymers [100, 101, 102]. For the short range interaction problem, $\Psi = d/2$, as for random walkers, from which the specialty of $d = 4$ is apparent.

In a quantum bound state a particle can tunnel through the potential. In a path integral approach the particle does a sizable excursion in the classically forbidden region outside the interaction well, sooner or later returning to the well (see Fig. 5.2). That the two particles will eventually be close-by to form a bound state is the source of entanglement while the excursions produce spreads of the trajectories in space and time. These spreads give the two relevant length scales $\xi_{\parallel}, \xi_{\perp}$. The large width of the bound state wave function near the QCP ensures the mutual influence of the particles even if far away from each other ($r \gg a$) so that the reduced density matrix for one particle still carries the signature of the entanglement and the criticality. For this bipartite system, we are interested in the ‘‘particle-partitioning entanglement’’ [103]. This makes the von Neumann entropy a valuable quantity for the transition which reads,

$$S^{vN} = -\text{Tr } \rho \ln \rho, \quad (5.6)$$

where ρ is the reduced density matrix for the ground state $|\psi\rangle$,

$$\rho(\mathbf{r}_1, \mathbf{r}'_1) = \text{Tr}_2 \varrho(1, 2) = \int d^d \mathbf{r}_2 \langle \mathbf{r}_1, \mathbf{r}_2 | \psi \rangle \langle \psi | \mathbf{r}'_1, \mathbf{r}_2 \rangle, \quad (5.7)$$

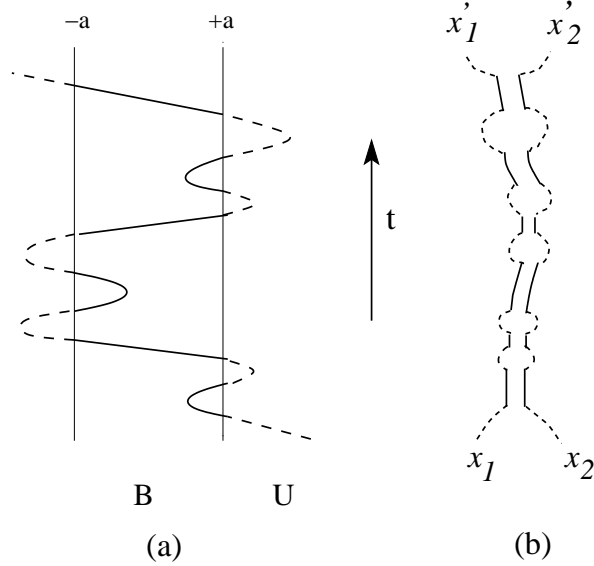


Figure 5.2: Path integral representation in the $x-t$ plane. (a) A relative coordinate path for two particles in one-dimension. The solid portions represent the classical bound state, i.e., inside the well (B), and the dashed portions represent the unbound (U) state in the classically forbidden region. (b) Corresponding path representation of two quantum particles with time, though intersections of paths are not shown explicitly. It is also a configuration of two classical Gaussian polymers interacting at the same contour length as for DNA base pairing, the t -axis representing the contour length (z) of the polymers. The dotted lines are the melted bubbles whose partition functions are characterized by the reunion exponent Ψ . This description holds for any general d .

obtained from the two particle density matrix $\rho(1, 2) = |\psi\rangle\langle\psi|$ by integrating out (or tracing out) particle 2. In Eq.(5.6), we shall introduce some pre-chosen length scale to make the argument of log dimensionless. If, with m_i, \mathbf{r}_i denoting the mass and the position of the i th particle, the full ground state wave-function (including the center of mass (CM)) is

$$\psi(\mathbf{r}_1, \mathbf{r}_2) = \Phi\left(\frac{m_1\mathbf{r}_1 + m_2\mathbf{r}_2}{m_1 + m_2}\right) \varphi(\mathbf{r}_1 - \mathbf{r}_2), \quad (5.8)$$

where Φ is CM wave function (plane waves) and φ is the wave function in relative

coordinate (the relative wave-function), then

$$\rho(\mathbf{r}_1, \mathbf{r}'_1) = \int d^d \mathbf{r}_2 \psi(\mathbf{r}_1, \mathbf{r}_2) \psi^*(\mathbf{r}'_1, \mathbf{r}_2). \quad (5.9)$$

Although the center of mass and the relative parts are not entangled, the two particles are entangled. The lack of knowledge of the state of one particle is the source of a nonzero entropy associated with the reduced density matrix [37, 38, 39].

The translational invariance of the interaction guarantees that the reduced density matrix $\rho(\mathbf{r}, \mathbf{r}') \equiv \rho(\mathbf{r} - \mathbf{r}')$ has $\exp(-i\mathbf{q} \cdot \mathbf{r})$ as the eigenvector,

$$\int d^d \mathbf{r}' \rho(\mathbf{r} - \mathbf{r}') e^{-i\mathbf{q} \cdot \mathbf{r}'} = \hat{\rho}(\mathbf{q}) e^{-i\mathbf{q} \cdot \mathbf{r}}, \quad (5.10)$$

with the eigenvalue

$$\hat{\rho}(\mathbf{q}) = \left| \phi \left(\mathbf{q} + \frac{\mathbf{K}\mu}{m_2} \right) \right|^2, \quad (5.11)$$

\mathbf{K} being CM wave vector and $\phi(\mathbf{q})$ the normalized momentum space wave function, the Fourier transform of the relative wave-function $\varphi(\mathbf{r})$ in Eq.(5.8). Since the entropy involves an integral over the whole range of \mathbf{q} , it is independent of the CM wave-vector, an expected consequence of Galilean invariance. Therefore, without any loss of generality, we choose $|\mathbf{K}| = 0$. The eigenvalues constituting the “entanglement spectrum” can be written in a scaling form

$$|\phi(\mathbf{q})|^2 = \kappa^{-d} F(\mathbf{q}/\kappa, a\kappa), \quad (5.12)$$

where $\kappa^2 = 2\mu |E|/\hbar^2 = \xi_{\perp}^{-2}$, μ being the reduced mass. Eq.(5.12) satisfies $\text{Tr} \hat{\rho} = 1$. In the critical regime (also called the “unitarity limit”), $a\kappa \rightarrow 0$, if the scaling function behaves smoothly, then

$$F(\tilde{\mathbf{q}}, a\kappa) \rightarrow F(\tilde{\mathbf{q}}, 0) \equiv f(\tilde{\mathbf{q}}), \quad (\tilde{q} \equiv q/\kappa) \quad (5.13)$$

which we find to be true for $d < 4$. For $d \geq 4$, we find that $F(\tilde{\mathbf{q}}, a\kappa)$ for $a\kappa \rightarrow 0$ behaves in a singular fashion as

$$F(\mathbf{x}, y) \sim y^{d-4} f(\mathbf{x}), \quad (5.14)$$

Chapter 5. Entanglement entropy of a quantum unbinding transition and entropy of DNA

so that the prefactor in Eq.(5.12) becomes $\kappa^{-4}a^{d-4}$. Here f represents a generic function. By using these limiting forms, we find the entanglement entropy to be

$$S^{vN} = P \ln a\kappa + c_0, \quad (5.15a)$$

$$P = \min(d, 4), \text{ and } c_0 = - \int d^d x f(x) \ln f(x). \quad (5.15b)$$

The last statement can be verified by direct computation of the momentum distribution function of the relative motion in d -dimensions. There are further log-corrections at $d = 2$ and $d = 4$ which we do not discuss here. To motivate Eq.(5.15a) let us consider a few examples. Consider the quantum problem of two particles interacting via a delta-function potential in one dimension: $V(\mathbf{x}) = -v_0\delta(x)$. By using the center of mass and the relative coordinate wave-function, we write the wave function as

$$\psi(x_1, x_2) = C e^{iK\mu\left(\frac{x_1+x_2}{m_2+m_1}\right)} e^{-\kappa|x_1-x_2|} \quad (5.16)$$

which is translationally invariant. Here K is the CM wave vector, $\kappa = \xi_{\perp}^{-1}$, and C is the normalization constant. The reduced density matrix for particle 1 is then

$$\rho(x, x') = \frac{C^2}{\kappa} e^{-(iK\mu/m_2+\kappa)|x'-x|} [1 + \kappa|x - x'|] \quad (5.17)$$

having eigenvalues (Eq.(5.11))

$$\hat{\rho}(\mathbf{q}) = \frac{2}{\pi} \frac{1}{\kappa (1 + \tilde{q}^2)^2}, \quad (K = 0), \quad (5.18)$$

which is of the form Eq.(5.13) with $f(\tilde{\mathbf{q}}) \sim (1 + \tilde{q}^2)^{-2}$. By introducing an arbitrarily chosen well strength \bar{v} or a scale $a = \hbar^2/2\mu\bar{v}$ in Eq.(5.6), the entanglement entropy is found to be of the form of Eq.(5.15a) with

$$P = 1, \text{ and } c_0 = \ln 8\pi - 2. \quad (5.19)$$

For $\kappa \rightarrow 0$, $\hat{\rho}(\mathbf{q}) \rightarrow \delta(q)$ with $S^{vN} = 0$. There is a difference between $\kappa \rightarrow 0$ and $\kappa = 0$. For a one-dimensional problem with the potential of Eq.(5.1), one can go over to the delta function potential problem by taking $a \rightarrow 0$ keeping $V_0a = v_0$ constant to get the same $\ln \kappa$ behaviour as in Eq.(5.19). We then check for a

3-dimensional potential well, Eq.(5.1). The relative wave-function ($l = 0$) for this potential is

$$\varphi(\mathbf{r}) = \begin{cases} A \frac{\sin kr}{r} & r < a \\ B \frac{e^{-\kappa r}}{r} & r > a, \end{cases} \quad (5.20)$$

with k and κ as defined earlier and constants A, B determined in the usual way of continuity of the wave function and its derivative. A direct Fourier transformation of $\varphi(\mathbf{r})$ has been used to numerically compute the entanglement entropy. To derive an analytical formula, we note that the dominant contribution in $\hat{\rho}(\mathbf{q})$ in the limit $a\kappa \rightarrow 0$ comes from the outer part. In this approximation we get

$$\hat{\rho}(\mathbf{q}) = \frac{1}{\kappa^3} \frac{1}{\pi^2} \left(\frac{1}{1 + \tilde{q}^2} \right)^2 = \kappa^{-3} f(\tilde{\mathbf{q}}). \quad (5.21)$$

This $\hat{\rho}(\mathbf{q})$ satisfies the normalization condition $\int d^3q \hat{\rho}(\mathbf{q}) = 1$. Thus for the 3D potential well interaction, the entanglement entropy is of the form of Eq.(5.15a) with

$$P = 3, \text{ and } c_0 = 2(1 + \log(4\pi)) \approx 7.06205. \quad (5.22)$$

Exact numerical computations of von Neumann entropy for $d = 3$ are done by using MATHEMATICA. For a given κ with $a = 1$, we determine V_0 , the depth of the well and then the matching conditions and the Fourier transform were used to obtain the entanglement spectra. The entanglement entropy is then obtained by a numerical integration. The results are shown in a log-linear S^{vN} vs. κ plot in Fig. 5.3 which also shows the line obtained from Eq.(5.15a) and Eq.(5.22). It shows that S^{vN} is negative for small κ and that it has linear $\ln \kappa$ dependence. The approximations show that the entropy is determined mainly by the outer part of the wave-function.

To generalize the result to any dimension we carried out the calculation for general d . The density matrix, solely from the outer part, is expected to be of the form $f(\tilde{\mathbf{q}}) \sim (1 + \tilde{q}^2)^{-2}$ as in previous cases but then there is a divergence problem for normalization for $d \geq 4$. Since we want $\text{Tr} \hat{\rho} = 1$, an ultraviolet cutoff is required. This makes $a\kappa$ an important variable even in the limit $a\kappa \rightarrow 0$. The specialty of $d = 4$ is now evident.

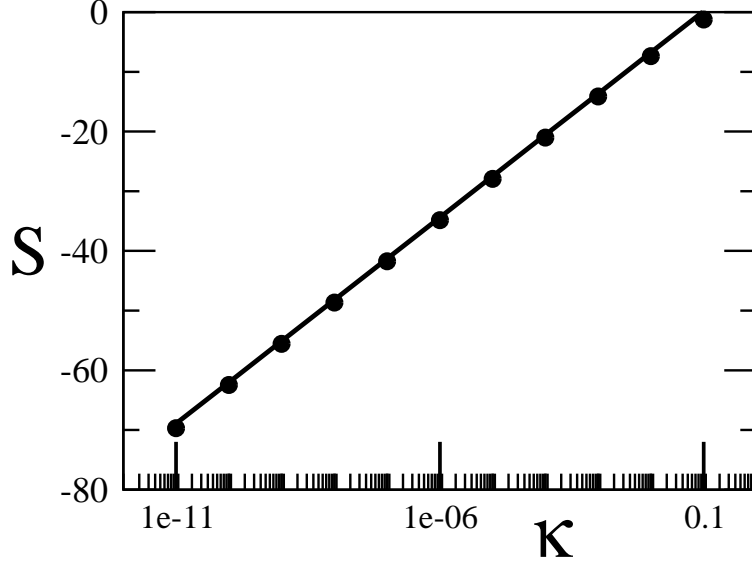


Figure 5.3: Plot of S^{vN} vs. $\ln \kappa$ with $a = 1$. The circles are the numerical values and the straight line is the predicted line $S^{vN} = 3 \ln \kappa + 7.06$, Eq.(5.22).

The radial wave function $R(r)$ ($l = 0$ state as the ground state) is,

$$R(r) = \begin{cases} A r^{\epsilon/2} J_{|\epsilon/2|}(kr) & \text{for } r < a \\ B r^{\epsilon/2} H_{|\epsilon/2|}^{(1)}(i\kappa r) & \text{for } r > a, \end{cases} \quad (5.23)$$

where $\epsilon = 2 - d$, A, B determine the normalization and matching of the inner and the outer solutions. Here J and $H^{(1)}$ are the Bessel and the Hankel function of the first kind. The continuity of the wave function at $r = a$ gives

$$A J_{|\frac{2-d}{2}|}(k_c) = B (\kappa a)^{-|\frac{2-d}{2}|}, \quad (5.24)$$

under the condition $\kappa \rightarrow 0$ and $ka \rightarrow k_c = \pi/2$. Eq.(5.3) follows from Eq.(5.24), the matching of log derivative and the Bessel function identities. By using the normalization condition and Eq.(5.24), we get

$$B = \begin{cases} \frac{\bar{\kappa}}{a} & \text{for } d < 4 \\ \frac{\bar{\kappa}^{2-d/2}}{a} & \text{for } d > 4. \end{cases} \quad (5.25)$$

In the same $\kappa \rightarrow 0$ limit, with outer part dominance,

$$\phi(q=0) \approx B\kappa^{-\frac{2+d}{2}}, \quad (5.26)$$

which gives

$$\begin{aligned} \hat{\rho}(\mathbf{q}) = |\phi(\mathbf{q})|^2 &= B^2\kappa^{-(2+d)} f(\tilde{\mathbf{q}}) \\ &\approx \begin{cases} \kappa^{-d}, & \text{for } d < 4, \\ \kappa^{-4}d^{d-4}, & \text{for } d > 4. \end{cases} \end{aligned} \quad (5.27)$$

So the von Neumann entropy is of the form Eq.(5.15a) with $P = 4$ for $d > 4$.

In terms of the deviation from the critical point, the entropy is

$$S^{vN} = \frac{d}{z(\Psi - 1)} \ln |u - u_c|, \quad \text{for } \Psi < 2. \quad (5.28)$$

For the case in hand, $\Psi = d/2$. The form of Eq.(5.28) brings out the universal behavior of the entropy and has validity for potentials different from Eq.(5.1), like e.g. scale-free $1/r^2$ potential [107]. All the details of the interaction go in the universal exponents z and Ψ . The entropy diverges at the critical point and, *is negative*.

5.3 DNA connection

We show the connection of the quantum entanglement entropy to the entropy of bubbles in DNA melting. Under an imaginary time transformation, the path integral formulation of the quantum problem is analogous to a classical statistical mechanical system of polymers used in the context of melting of DNA [100, 101, 102, 104].

Let us consider a DNA whose two strands are two Gaussian polymers in d -dimensions and index the points (monomers) by the contour length z measured from one end. The native base pairing of a DNA requires that a monomer at index z on one strand interacts with a point on the other strand with the same index z . This is the Poland-Scheraga type model [102] for DNA melting. By using one extra coordinate for the sequence or the length of the polymers, we get

directed polymers in $d + 1$ dimensions like paths in path integrals, as shown in Fig. 5.2. In this representation the base pairing interaction maps onto the same time interaction of the quantum system, time playing the role of the base pair index. The DNA partition function as a sum over all polymer configurations is equivalent to the sum over all paths in quantum mechanics. The DNA Boltzmann factor $\exp(-\beta H)$ with β as the inverse temperature and H the Hamiltonian for two chains of elastic constants K_j as

$$\beta H = \int_0^N \left[\sum_{j=1,2} \frac{K_j}{2} \left(\frac{\partial \mathbf{r}_j(z)}{\partial z} \right)^2 + V(\mathbf{r}_1(z) - \mathbf{r}_2(z)) \right] dz, \quad (5.29)$$

corresponds to the factor $\exp(i\mathcal{S}/\hbar)$ for path integrals with \mathcal{S} the classical action of two interacting particles under $z \rightarrow it$. This makes the Green function or the propagator $\mathcal{G}(x_1, x_2, \tau | x'_1, x'_2, 0)$ equivalent to the partition function $Z(x_1, x_2, N | x'_1, x'_2, 0)$, ($N \rightarrow i\tau$). Here x_j, x'_j are the coordinates of the j -th strand end-points at 0 and at length N . The free energy per unit length of DNA for $N \rightarrow \infty$ is the ground state energy of the quantum problem.

The short range base-pairing potential can be taken to be a contact potential or a well of Eq.(5.1). Then the picture of return of the quantum particles within the range of interaction after excursions outside the well gives the equivalent picture of polymers with broken base pairs having excursion away from binding and eventually coming back to the well to form pairs. This excursion swells the polymer and creates bubbles along the length of the DNA. Thermal energy opens up bubbles in the bound state of DNA. The entropy of a bubble of length N is determined by the reunion partition function of two polymers starting together and reuniting again at N , which for large N , has the form $\Omega(N) = N^{-\Psi} e^{N\sigma_0}$, or the entropy

$$S \equiv \ln \Omega(N) = N\sigma_0 - \Psi \ln N, \quad (5.30)$$

in units of the Boltzmann constant $k_B = 1$. Eq.(5.30) shows that σ_0 is the bubble entropy per unit length that survives in the thermodynamic limit. However, the power law N -dependence which gives the negative sub-extensive part of the entropy is essential for the transition and also for the bound state. The reunion exponent Ψ determines the universality class of the binding-unbinding transition and there

is a melting transition if and only if $\Psi > 1$. See Ref. [100] for details.

The one-dimensionality of the chains requires an alternating arrangement of bound regions and bubbles as in Fig. 5.2. The arrangement allows one to write the partition function, after Laplace transform with respect to the length (i.e. in the grand canonical ensemble) [100], as

$$\begin{aligned} G(x, y; s) &= G_o(x; s)G(0, s)G_o(y; s) \\ &= \frac{G_o(x; s)G_o(y; s)G^B(s, u)}{1 - G^U(s, \sigma_0)G^B(s, u)}. \end{aligned} \quad (5.31)$$

Here $x \equiv \{x_1, x_2\}$, $y = \{x'_1, x'_2\}$, G_o is the Laplace transformed partition function of two polymers tied at one end and open at the other, called the survival partition function, and $G(0, s)$ is the total partition function with two ends bound. In G_o , the tied point is to be integrated over keeping the set x or y fixed. $G(0, s)$ can be written as a sum of a geometrical series (see Fig. 5.2) involving the partition functions of the bound parts and the bubbles, $G^B(s, u)$ and $G^U(s, \sigma_0)$. The free energy comes from the singularity of $G(x, y, s)$ which is either $s = \sigma_0 \equiv 0$ or at $s = s_0$ for which

$$G^U(s, \sigma_0)G^B(s, u) = 1, \quad (5.32)$$

with $\sigma_0 = 0$, s_0 satisfies Eq.(5.3).

Near the nontrivial singularity, a pole at $s = s_0$, the form of $G(x, y, s)$ resembles the Green function in the energy eigenfunction expansion as

$$\frac{\langle y|\psi\rangle\langle\psi|x\rangle}{E - E_0}, \quad (5.33)$$

with ground state dominance. From the equivalence between DNA model and the quantum problem, we identify the density matrix as

$$\rho(x, y) \sim G_o(x; s_0)G_o(y; s_0)/G^U(s_0),$$

so that the entanglement entropy would behave like $S \sim \ln G^U(s_0, \sigma_0)$. By using Gaussian distributions for Gaussian polymers (i.e. random walkers), one recovers Eq.(5.21).

To get the behaviour of $\ln G^U$, we employ a finite-size scaling analysis. The

phase transition in the polymeric system occurs in the $N \rightarrow \infty$ limit so that a finite N acts as a finite size scale both for DNA and in the quantum problem. The finite size scaling variable is N/ξ_{\perp}^z so that the entanglement entropy is proportional to $-z \ln \xi_{\perp} \sim \frac{1}{\Psi-1} \ln |u - u_c|$ (see Eq.(5.28)). The difference in the amplitude occurs because of the different normalization used for polymers and quantum problems. The point to note is that the entanglement entropy in the quantum problem comes from the universal non-extensive part of the entropy of the bubbles. Since the full entanglement spectrum is known, it is also possible to compute the Renyi entropy [44]. We recover in the appropriate limit the result quoted in Eq.(5.15a). In the DNA interpretation, the Renyi entropy would come from many circular single strands (replicas) pairing with a large single strand, resembling the rolling circle replication of viruses. Details will be discussed elsewhere.

5.4 Discussion

A negative entropy is counter-intuitive when one has the third law of thermodynamics in the back of one's mind, though exceptions are known; e.g. negative entropy is found for perfect gases at low temperatures or as a corollary of the classical equipartition theorem. One can see the same feature by writing the reduced density matrix in terms of an entanglement Hamiltonian, $\rho \propto \exp(-\beta H_{\text{ent}})$, in a form reminiscent of a Boltzmann factor. The diagonal form in Eq.(5.21) shows

$$\beta H_{\text{ent}} = 2 \ln(1 + q^2/\kappa^2) \approx 2q^2/\kappa^2, \quad (\text{for small } q), \quad (5.34)$$

which is like a classical d -dimensional oscillator in q -space, with κ^2 as the effective temperature. A direct calculation or use of the classical equipartition theorem now tells us that the entropy has $d \ln \kappa$ behaviour as in Eq.(5.15a). We believe this to be a generic feature whenever the entanglement Hamiltonian is gapless. Another way to see this emergence of $\ln \kappa$ in entropy is to compare with the DNA problem. The equivalent classical DNA model also has a negative diverging part of entropy but that sub-extensive part vanishes in the thermodynamic limit of the entropy per unit length. In the quantum case, the equivalent limit has no such advantage in finding the entropy because demanding extensivity in time direction is meaningless. Hence the negatively diverging term is inevitable near criticality.

Chapter 5. Entanglement entropy of a quantum unbinding transition and entropy of DNA

In this chapter we show that the quantum entanglement entropy near the bound-unbound transition of two interacting particles comes out to be negative, and it diverges at the QCP. Using the equivalent classical statistical mechanical system of DNA near the melting transition we show that the negativity of the entanglement entropy is a necessity and is essential for the phase transition. The coefficient of the logarithmic term contains the information of the interaction and the universal behaviour of the phase transition. The coefficient is shown to be related to the reunion exponent of vicious walkers. This is the first time in the context of quantum entanglement that the negative entropy is found by explicit calculation. We argue that this log divergence in the quantum case and the sub-extensive part in the DNA problem are linked by finite size scaling near the critical point. From the renormalization group (RG) approach for the DNA melting problem [101, 107], one may infer that the entanglement entropy increases along the RG flow, since the critical point corresponds to the unstable fixed point. It has been argued recently that entanglement can be used to produce negative entropy [105]. The information theoretical meaning of the negative entropy in our case is not very clear. Our speculation is that the negative entropy is the norm, not an exception near a quantum binding-unbinding transition. We feel signatures of negative entropy might be detectable in cold atoms where interactions can be tuned to the unitarity limit. If one can harness the negative entropy, one may cool a system or a computer and possibly may overcome the obstacle to circuit miniaturization.

What next: In the next chapter, we are going to consider another important interaction, an inverse square potential, which itself has a great importance as a quantum as well as classical problem. The special points in the DNA phase transition are again obtained from the study of the quantum problem, thus making the connection of the interacting polymers vs. interacting quantum particles more robust.

List of symbols

A, B	Normalization constants of the wave function
a	Width of the potential
d	Dimension
H_{ent}	Entanglement Hamiltonian
H	Hamiltonian
$ k\rangle$	Basis of momentum states
λ	Reduced strength of $1/r^2$ potential
m	Mass
μ	Reduced mass
N	Length of polymer
Ω	Reunion partition function
\mathbf{p}, q	Momentum
r	Relative distance
σ_0	Bubble entropy per unit length
S^{vN}	von Neumann entropy
T	Temperature
t	Time
u	Dimensionless short range potential
V_0	Depth of the potential well
V	Potential
Ψ	Reunion exponent of two polymers
Z	Partition function

6

Quantum unbinding transition for a long range potential

It is shown in the previous chapter that the von Neumann entropy of two particles has a $d \ln \kappa$ behavior at the quantum critical point (QCP) of unbinding in dimensions $1 < d < 4$ where κ is the inverse of the width of the wave function. Here the QCP is attained when the inverse length scale κ approaches zero. This is achieved by tuning the potential or the mass. This has been established analytically for a 3D potential well [106]. Also, in analogy to polymer, it is shown that this divergence is essential for the criticality and linked to the reunion behavior of two polymers in the equivalent classical statistical mechanical problem. In this chapter, we study the von Neumann entropy for a QPT involving a marginal long-range potential. The equivalent classical statistical mechanical problem involves two directed polymers interacting at the same contour length like a DNA with native base pairing but with an additional $1/r^2$ interaction. This model has been studied using renormalization group in Ref. [107, 108]. Since the strength of the long-range interaction changes the nature of the transition, we study how the von Neumann entropy changes with variation of its strength and sign. In addition, we extend our study on the entanglement entropy to the Renyi entropy, which is another extensively studied quantity in the context of the quantum entanglement entropy.

6.1 Introduction

This chapter considers two particles interacting through the three-dimensional inverse square law potential and finds the quantum entanglement between the particles. Here we use particle partitioning [44]. The Hamiltonian for the two particles we shall be using is,

$$H = \frac{\mathbf{p}_1^2}{2m_1} + \frac{\mathbf{p}_2^2}{2m_2} + V(\mathbf{r}_1 - \mathbf{r}_2), \quad (6.1)$$

where m_i , \mathbf{r}_i and \mathbf{p}_i are the mass, position and the momentum of the i th particle and

$$V(r) = \begin{cases} -V_0, & \text{for } r < a, \\ -\frac{2\mu}{\hbar^2} \frac{g}{r^2}, & \text{for } r > a, \end{cases} \quad (6.2)$$

is a central potential, where $V_0 > 0$ and $\mu = m_1 m_2 / (m_1 + m_2)$ is the reduced mass of two particles. We take $2\mu/\hbar^2 = 1$.

The inverse square potential is of immense importance in quantum mechanics [109]. It is at the boundary of the short and long range potential. For potentials decaying like r^{-p} , there is no finite bound state if $p > 2$ while for slower divergence, i.e., $p < 2$, there is a finite negative lower bound in energy. For an attractive potential $-g/r^2$ ($g > 0$), the kinetic and the potential energies are of the same order near small r and so the bound state spectrum depends on the value of g . A manifestation of the borderline case is in the scale-free nature, $H(\lambda r) = \lambda^{-2} H(r)$. This makes, g , the dimensionless strength of the potential, a ‘‘marginal’’ parameter in the RG sense in all dimensions. The singularity of g/r^2 at the origin prevents discrete bound states to occur. A suitable modification of the potential at small r , e.g. by putting a cut off and replacing the potential by a short range finite one near origin, gives discrete bound states. This is done in Eq.(6.2).

It is established in quantum mechanics that there is no finite energy ground state for $g > 1/4$. For $g < 1/4$ the wave function is normalizable and the bound state energy can be obtained by the standard procedure. In the above-mentioned range of g , the unbinding transition can be obtained by tuning the strength of the short range potential near $r = 0$ depicting the quantum phase transition. The unbinding transition in this long range interaction is a unique example of a QPT whose type can be first order ($g < -3/4$), critical ($g = -3/4$) but non-universal, and even Kosterlitz-Thouless type ($g = 1/4$) [108]. The solvability and the wide

repertoire of QPT behavior make this model an ideal terrain for exploration of the nature of entanglement entropy around a QPT. This is what we set to do in this chapter.

A phase transition is defined as a singularity in the energy, associated with diverging length scales. In this sense the quantum unbinding transition is a genuine phase transition. This QPT exists because time of infinite extent plays a role in quantum mechanics. It becomes clear in the path integral formulation. The quantum problem can be mapped onto an equivalent classical statistical mechanical problem of polymers under the imaginary time transformation ($it \rightarrow N$). The time in the quantum problem then becomes the length of the polymer, N , the Green's function maps to the partition function and the ground state energy is equivalent to the free energy per unit length. The interaction between the polymers means the interaction of a pair of bases or monomers at the same index along the length of the polymers as in DNA. This is equivalent to the same time interaction of two quantum particles. The equivalent classical problem in the context of melting transition of two polymers interacting via a potential like Eq.(6.2) has been discussed in Ref. [107] which reveals that the results of the quantum problems can be recovered from such studies. Like the quantum particle making excursion inside and outside of the well, the polymers also come closer, they reunite, and move further, forming swollen bubbles. The entropy of a bubble of length N is

$$\ln \Omega(N) = N\sigma_0 - \Psi \ln N, \quad (6.3)$$

where $\Omega(N)$ is the reunion partition function of two polymers starting together, reuniting anywhere in space again at length N , σ_0 is the bubble entropy per unit length and Ψ is the reunion exponent. The details can be found in Refs. [106, 107, 100].

The binding-unbinding transition of polymers has been studied in the context of the necklace model of polymers and it is found that the reunion exponent Ψ determines the order of transition [100]. The phase transition occurs if $\Psi \geq 1$. The transition is continuous if $1 < \Psi < 2$, while it is first order for $\Psi > 2$. In three dimension, the reunion exponent is given by [107]

$$\Psi = 1 + \lambda, \quad \text{with} \quad \lambda = \sqrt{\frac{1}{4} - g}, \quad (6.4)$$

g	-2	-3/4	0	$< 1/4$	1/4	$> 1/4$
λ	1.5	1	1/2	real	0	imaginary

 Table 6.1: g - λ conversion table.

where the dependence on g , a bit counter-intuitive, is a consequence of its marginality. Here also we use the parameter $\lambda(> 0)$ because of its occurrence in the sequel. Table 1 gives the correspondence between g and λ for easy reference.

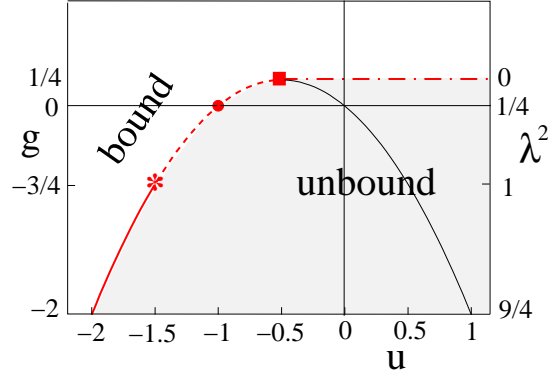


Figure 6.1: g vs. u phase diagram. The plot shows the phases and the RG fixed points in the g - u plane ($u = -V_0 a^2$). The red curve below $g = 1/4$ and $u = -0.5$ show the binding-unbinding transitions governed by a line of unstable real fixed points. The transition is first order for $g < -3/4$ and second order for $-3/4 < g < 1/4$. This line is the transition line in the limit of zero range potential ($a \rightarrow 0$, $V_0 \rightarrow \infty$, with $u = \text{constant}$) The black continuous curve for $u > -0.5$ shows the locus of stable fixed points representing the unbound phase. The dashed-dotted line at $g = 1/4$ is the boundary beyond which the fixed points are complex.

The phase diagram and the lines of RG fixed points are shown in Fig. 6.1. This plot shows the phases in the g - u plane, where

$$u = -V_0 a^2, \quad (6.5)$$

in the unit of $2\mu/\hbar^2 = 1$, is the dimensionless short range potential which the two particle state is in. The fixed points shown here are obtained from the renormalization group analysis done in Ref. [107]. The red line for $u < -0.5$ shows the unstable fixed points across which the unbinding transition takes place, and the

black continuous line for $u > -0.5$ shows the phases by stable fixed points. For $g < -3/4$, the bound-unbound transition is first order as $\Psi > 2$, which is shown by the red continuous line ending at the symbol * at $g = -3/4$, or, $\lambda = 1$, multicritical point. After that the transition is continuous upto $g = 1/4$ with $\Psi < 2$. Beyond that, where λ is imaginary, there is no real fixed point, and the system is in a bound state. Across the $g = 1/4$ line, with $u \geq -0.5$, a Kosterlitz-Thouless type phase transition from the bound to the unbound state can be induced by tuning g . The two regimes, $\Psi < 2$ and $\Psi > 2$ are governed by different behaviors, with additional log-corrections at $\Psi = 2$.

We find that the entanglement entropy also carries this signature of the speciality of $g = -3/4$ or $\lambda = 1$. The entropy in the three different regimes, $\lambda < 1$, $\lambda = 1$ and $\lambda > 1$ scale in different manners. We establish that $\lambda = 1$ behaves like a multicritical point, controlling both the first order and the critical behavior in the whole range $-2 \leq g \leq 1/4$.

6.1.1 Outline

The outline of the chapter is following. In Sec. 6.2, we describe our model and the method by which we calculate the von Neumann entropy. The analytical results are presented in Sec. 6.3 and the von Neumann entropy is calculated for $\lambda < 1$. Next we present the exact numerical results done in MATHEMATICA and discuss the behavior of the entropy and its scaling in Sec. 6.4. Finally we conclude in Sec. 6.5.

6.2 Model and method

Eq.(6.2) is used for our study. The detailed nature of the short range potential is not important and we take it as a simple square well potential. We concentrate in the range $0 < \lambda < 1.5$.

The reduced density matrix of the considered problem in the basis of momentum states $|\mathbf{k}\rangle$ has the form

$$\rho = \int d^d\mathbf{k} |\phi(\mathbf{k})|^2 |\mathbf{k}\rangle\langle\mathbf{k}| = \int d^d\mathbf{k} \frac{e^{-\beta H_{ent}}}{Z} |\mathbf{k}\rangle\langle\mathbf{k}|, \quad (6.6)$$

which makes the mixed state characteristic explicit. Eq.(6.6) allows us to define ρ as a thermal density matrix with an entanglement Hamiltonian H_{ent} at a fictitious inverse temperature β with Z as the partition function. This thermal correspondence makes the von Neumann entropy equivalent to the Gibbs entropy of H_{ent} .

In Eq.(6.6), H_{ent} is a c -number. Consider the canonical partition function of a free particle at temperature T ,

$$Z \sim \int d^d q \exp(-\beta H) \sim T^{d/2}, \quad (6.7)$$

where $H = \hbar^2 q^2 / 2m$. Then the entropy becomes,

$$S^{vN} = \ln Z \sim \ln T \quad (6.8)$$

which for very low temperature, $T \rightarrow 0$ becomes negative. In another way, one gets a constant specific heat C from the equipartition theorem, which then gives a logarithmic dependence on temperature of the entropy,

$$S^{vN} = \int^T C/T dT \sim \ln T. \quad (6.9)$$

The Sackur-Tetrode constant, S_0/R , the entropy of one mole of an ideal gas at temperature $T = 1K$ and at one atmospheric pressure, 101.325 kPa, is a fundamental constant [110]. Its value is -1.1648708 . Note that this fundamental entropy is negative. Classical harmonic oscillator is no exception. It is well-known that the condition $S^{vN} \geq 0$ does not hold for the classical continuous statistical mechanics [111].

6.3 Analytical results

In this section, we derive the asymptotic behavior of $\phi(q)$. In particular we find that the entropy is dominated by the outer part, i.e. the excursion in the classically forbidden region, if the unbinding transition is critical. This happens for $0 < \lambda \leq 1$. For first order transition, the inner part also contributes significantly.

The ground state has zero angular momentum. For this s -state, the radial part

of the Schrodinger equation then reads [112]:

$$\frac{\partial^2 R}{\partial r^2} + \frac{2}{r} \frac{\partial R}{\partial r} + (V_0 + E) R = 0, \quad \text{for } r < a, \quad (6.10)$$

$$\text{and, } \frac{\partial^2 R}{\partial r^2} + \frac{2}{r} \frac{\partial R}{\partial r} + \left(\frac{g}{r^2} + E\right) R = 0, \quad \text{for } r > a, \quad (6.11)$$

where E is the ground state energy of the particle describing the behavior of the two particles in relative coordinate. The radial part of the wave functions in the relative coordinate are then obtained by solving Eqs.(6.10) and (6.11),

$$R(r) = \begin{cases} \frac{A}{r} \sin kr, & \text{for } r \leq a, \\ \frac{B}{\sqrt{r}} H_{\lambda}^{(1)}(i\kappa r), & \text{for } r \geq a, \end{cases} \quad (6.12a)$$

$$(6.12b)$$

with A and B as the normalization constants,

$$k^2 = V_0 - |E|, \quad \kappa^2 = |E|. \quad (6.13)$$

We choose λ to be positive and it is given by Eq.(6.4). In the limit of $\kappa \rightarrow 0$, the unbinding transition takes place. This makes our interest in studying the von Neumann entropy in this limit.

The continuity of the wave functions at $r = a$ gives,

$$\frac{A}{a} \sin ka = \frac{B}{\sqrt{a}} H_{\lambda}^{(1)}(i\kappa a). \quad (6.14)$$

The matching condition of the derivative of the wave function at $r = a$ gives the relation between k and κ which determines the value of k for a given κ ,

$$ak \cot ak = i\kappa a \frac{H_{\lambda-1}^{(1)}(i\kappa r)}{H_{\lambda}^{(1)}(i\kappa r)} - \lambda + \frac{1}{2}. \quad (6.15)$$

Given the values of λ and a , one can get the threshold or minimum value of k , k_m , for just one bound state. For $\kappa = 0$,

$$ak_c \cot ak_c = \frac{1}{2} - \lambda, \quad (6.16)$$

is the condition for the transition point when the ground state energy $E \rightarrow 0$. For $\lambda = -1/2$, $k_c = 0$ and $\lambda \rightarrow \infty$ gives $ak_c = \pi/2$. But as we take $\lambda \geq 0$, there is always a k_c for any λ .

Now consider a small deviation from the critical value of k , $k = k_c - \delta$ where $\delta \sim V_0 - V_c$. Then, from Eq.(6.15),

$$(ak_c - a\delta) \cot(ak_c - a\delta) \sim \begin{cases} (\kappa a)^{2\lambda}, & \text{for } \lambda < 1, \\ \kappa^2 a^2, & \text{for } \lambda > 1, \end{cases} \quad (6.17)$$

or,

$$|E| \sim \kappa^2 \sim \begin{cases} \delta^{1/\lambda}, & \text{for } 0 < \lambda < 1, \\ \delta + O(\delta^{1/(\lambda-1)}), & \text{for } \lambda > 1. \end{cases} \quad (6.18)$$

These show that as $V_0 \rightarrow V_c \equiv k_c^2$, E remains continuous, as it should. For $\lambda < 1$, E approaches zero tangentially while for $\lambda > 1$, there is a nonzero slope at $\kappa = 0$. This discontinuity of slope classifies the $\lambda > 1$ transition as first order. Despite that, the higher derivatives on the bound side $\partial^n E / \partial \delta^n$ would show divergences like a critical point.

The normalization constants A and B are found by using the continuity condition and taking the limit $\kappa \rightarrow 0$ (see Appendix for details)

$$|B|^2 \sim \begin{cases} \kappa^2, & \text{for } \lambda < 1, \\ \kappa^2 (a\kappa)^{2\lambda-2}, & \text{for } \lambda > 1, \end{cases} \quad (6.19)$$

and,

$$|A|^2 \sim \begin{cases} (a\kappa)^{2-2\lambda}/a, & \text{for } \lambda < 1, \\ 1/a, & \text{for } \lambda > 1. \end{cases} \quad (6.20)$$

At $\lambda = 1$, there are log corrections which we do not get into here. The log correction appears in the Necklace model for polymers whenever the reunion exponent Ψ (Eq.(6.4)) is an integer. The log appears in Eq.(6.15) via $H_0^{(1)}$ for $\lambda = 1$. Now one knows the full wave function and its limiting κ behavior.

The reduced density matrix has eigenvalues $|\phi(q)|^2$, where q is the momentum space variable. To get these eigenvalues, the Fourier transformation of the wave-

function needs to be done,

$$\phi(q) = \frac{1}{(2\pi)^{3/2}} \int d^3r e^{i\mathbf{q}\cdot\mathbf{r}} R(r) = \phi_i(q) + \phi_o(q), \quad (6.21)$$

where the subscript i, o refer to the inner ($r < a$) and the outer ($r > a$) part. The Fourier transform of the inner part (Eq.(6.12a)) is

$$\phi_i(q) = \frac{A}{q} \frac{1}{\sqrt{2\pi}} \left[\frac{\sin(k-q)a}{k-q} - \frac{\sin(q+k)a}{q+k} \right], \quad (6.22)$$

and of the outer part (Eq.(6.12b)) is

$$\begin{aligned} \phi_o(q) = & |B| \kappa^{-5/2} \frac{2}{\pi} \sqrt{2} \Gamma \left[\frac{5}{4} + \frac{\lambda}{2} \right] \Gamma \left[\frac{5}{4} - \frac{\lambda}{2} \right] {}_2F_1 \left(\frac{5}{4} + \frac{\lambda}{2}, \frac{5}{4} - \frac{\lambda}{2}; \frac{3}{2}; -\tilde{q}^2 \right) \\ & - |B| \int_0^a dr \sqrt{r} \frac{\sin qr}{q} K_\lambda(\kappa r), \end{aligned} \quad (6.23)$$

where $\tilde{q} = q/\kappa$, ${}_2F_1$ is the hypergeometric function and K_λ is the modified Bessel function. The last integral in Eq.(6.23) is convergent for all $\lambda < 3/2$ and therefore can be ignored in the $a\kappa \rightarrow 0$ limit.

The limiting small κ dependence of the inner and the outer parts of the wave function from Eqs.(6.22) and (6.23) are,

$$\phi_i(q) = \begin{cases} \bar{\kappa}^{1-\lambda} a^{3/2} f_i(aq) & \text{if } \lambda < 1, \\ a^{3/2} f_i(aq) & \text{if } \lambda > 1, \end{cases} \quad (6.24)$$

and

$$\phi_o(q) = \begin{cases} \kappa^{-\frac{3}{2}} f_\lambda(\tilde{q}) & \text{if } \lambda < 1, \\ \kappa^{-\frac{3}{2}} \bar{\kappa}^{\lambda-1} f_\lambda(\tilde{q}) & \text{if } \lambda > 1, \end{cases} \quad (6.25)$$

where $\tilde{q} = q/\kappa$ and f_i is a well-behaved function. Eq.(6.24) is for large \tilde{q} .

From Eqs.(6.24) and (6.25), we see that the double limit $\kappa \rightarrow 0$, $\lambda \rightarrow 1$ is singular because of the term $\bar{\kappa}^{1-\lambda}$. This identifies $(\kappa = 0, \lambda = 1)$ as a special point. From this we also identify $(1 - \lambda) \ln \kappa$ as an appropriate scaling variable. This scaling variable will occur below in the analysis of the numerical results.

For $\lambda < 1$, i.e., $1 - \lambda > 0$, $\bar{\kappa}^{1-\lambda} \rightarrow 0$ as $\kappa \rightarrow 0$ and therefore, the contribution of outer part dominates over the inner part in the von Neumann entropy. Without

much loss, one can then write the entropy with the outer part only (Eq.(6.25)),

$$\begin{aligned} S^{vN} &\approx - \int d^3q |\phi|^2 \ln |\phi_o|^2 \\ &= 3 \ln \kappa + c_\lambda, \quad (\text{for } \lambda < 1), \end{aligned} \quad (6.26)$$

with

$$c_\lambda = \int d\tilde{q} \tilde{q}^2 f_\lambda(\tilde{q}) \ln f_\lambda(\tilde{q}). \quad (6.27)$$

As per our interest, we extract the κ -dependent term and call the rest c_λ , which is a function of other parameters. The main result is that there is a log divergence of S^{vN} as $\kappa \rightarrow 0$.

6.4 Exact numerical results

To study the nature of the entanglement entropy, over the whole range of λ we take recourse to exact numerical calculation using MATHEMATICA for the 3-dimensional potential well. We cross-check our prediction of Eq.(6.26) and then show a multi-critical scaling that covers the range $0 < \lambda < 1.5$.

6.4.1 Protocol

Although V_0 is the tuning parameter, it is more convenient to use the length scale as the independent parameter. With this trading of κ for V_0 , our protocol is like this: Given the values of κ and λ , the value of k_m was determined from Eq.(6.15), with $k_m < \pi$ that assures us the ground state. As $\kappa \rightarrow 0$, $k_m \rightarrow k_c$. Then the corresponding normalization coefficients A and B were found using the normalization condition and the continuity equation, i.e., by doing the r -integrations of the inner and the outer parts of the wave function in Eq.(6.35). These constants are used in the Fourier transformed inner and outer parts of the wave function, Eqs.(6.22) and (6.23), to calculate the von Neumann entropy. In the final integration for $S^{vN} = -\text{Tr } \rho \ln \rho$, we put an upper cut off making sure that the final numbers are independent of this choice of cut off. Also the intervals of the integration range have been chosen carefully especially for $q \sim \kappa$. This gives numerically exact numbers for the entropy for the given κ and λ . This procedure is repeated for various

λ and κ . We set $a = 1$.

6.4.2 Behavior of the von Neumann entropy S^{vN}

λ dependence:

The plots of the numerical values of the von Neumann entropy S^{vN} against $\ln \kappa$ and λ show different behavior of entropy in different ranges of λ , *viz.*, $\lambda < 1$, $\lambda > 1$ and $\lambda = 1$.

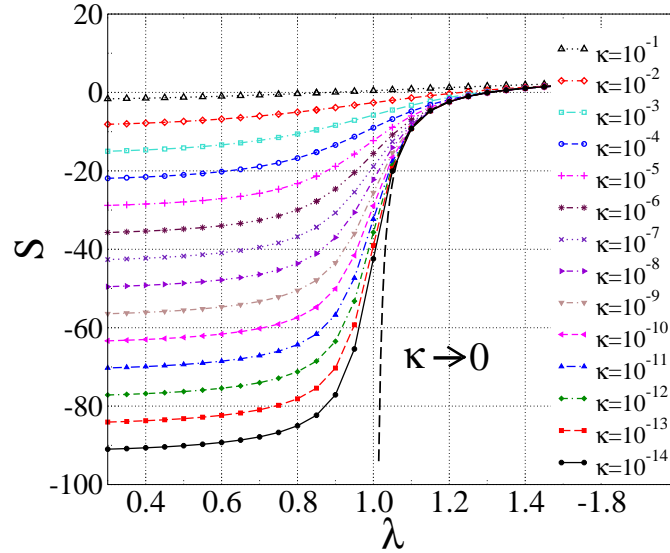


Figure 6.2: S^{vN} vs. λ for various κ . In the plot $S = S^{vN} + 8 \ln \frac{2}{\pi}$. The plot shows that the entropy diverges for $\lambda \leq 0$ as $\kappa \rightarrow 0$. The dashed line marked as $\kappa \rightarrow 0$ is the expected behavior of the entropy for $\lambda > 1$.

Let us first look at the plot of S^{vN} vs. λ in Fig. 6.2, where different lines represent different values of κ . For $\lambda < 1$, the von Neumann entropy for small κ saturates to a negative value as λ is varied and that saturation value depends on the value of κ . The smaller the value of κ , the more negative is the entropy, and $\kappa \rightarrow 0$ takes the saturation value to negative infinity. The long range part of the potential is attractive for $\lambda > 0.5$ and repulsive otherwise. But the entropy shows no signature as it crosses $\lambda = 0.5$. On the other hand, for $\lambda > 1$ where the transition becomes first order, the entropy does not decrease much with κ , rather becomes independent of κ . It remains finite for $\lambda > 1$ and diverges at $\lambda = 1$ like

the black dashed curve in Fig. 6.2. S^{vN} becomes positive at $\lambda \sim 1.3$. It seems that this point has no significance otherwise.

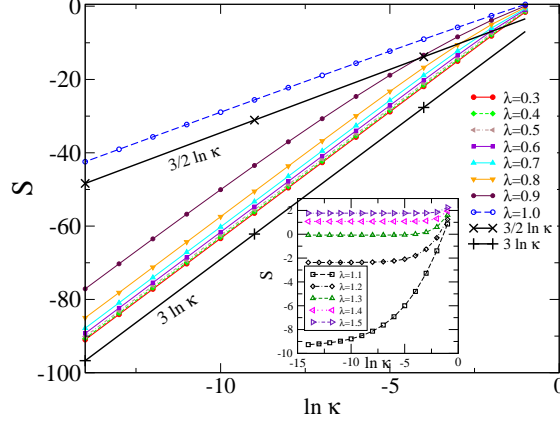


Figure 6.3: S^{vN} vs. $\ln \kappa$ for various λ . Here, as in Fig. 6.2, $S = S^{vN} + 8 \ln \frac{2}{\pi}$. For comparison, $3 \ln \kappa$ and $\frac{3}{2} \ln \kappa$ are shown by black lines with the symbols + and \times . The inset shows that the entropy is κ -independent for $\lambda > 1$.

κ dependence:

The behavior of the von Neumann entropy with λ and κ becomes more clear when one looks at the plot of S^{vN} vs. κ (Fig. 6.3). This plot shows the different characteristic behaviors of S^{vN} in the three distinct ranges of λ : $\lambda < 1$, $\lambda = 1$ and $\lambda > 1$. For small κ , all $\lambda < 1$ curves have slope 3 when plotted against $\ln \kappa$, i.e. for $\lambda < 1$, the entropy is of the expected form $3 \ln \kappa + c_\lambda$ which is shown from analytical calculations. To get $3 \ln \kappa$, one has to see below some value of κ , and as λ approaches one, even smaller κ needs to be considered. But no matter how close to 1 is the value of λ , one gets $3 \ln \kappa$ until $\lambda < 1$. Exactly at $\lambda = 1$, the slope changes suddenly to $3/2$ and hence

$$S^{vN} = \frac{3}{2} \ln \kappa + c_1, \quad \text{for } \lambda = 1. \quad (6.28)$$

A somewhat different behavior is seen for the rest with $\lambda > 1$ (inset of Fig. 6.3). For small κ , the curves reach a λ -dependent constant value and do not change with κ . Clearly the entropy has no κ -dependence for $\lambda > 1$ and it is finite. By definition, these constant values are c_λ and $S^{vN}(\lambda > 1) = c_\lambda$. So, we see that there are three

classes:

$$S^{vN} = \begin{cases} 3 \ln \kappa + c_\lambda & \text{for } \lambda < 1, \\ \frac{3}{2} \ln \kappa + c_1 & \text{for } \lambda = 1, \\ c_\lambda & \text{for } \lambda > 1. \end{cases} \quad (6.29)$$

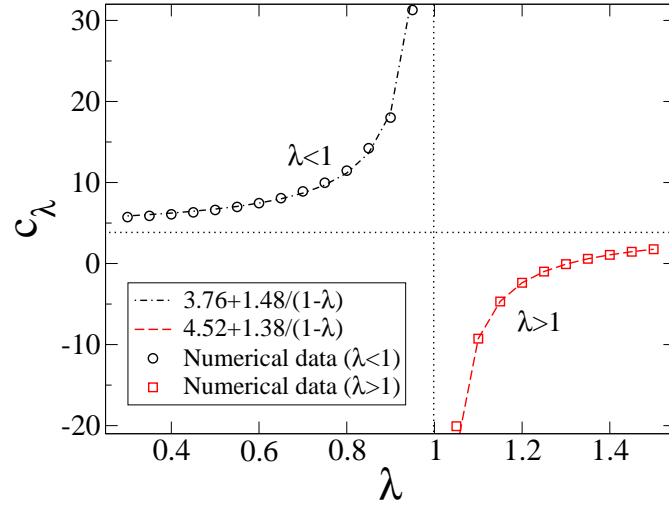


Figure 6.4: The plot of c_λ vs. λ , showing a divergence at $\lambda = 1$.

On c_λ

Now we have knowledge of the κ dependent part in the von Neumann entropy for different λ . The next question is how the c_λ behaves with λ , and if they have different nature in different regimes of λ . So, we collect the c_λ s according to Eq. eqch6:scla and plot against λ . This plot (Fig. 6.4) shows a divergence at $\lambda = 1$ indicating that $(1 - \lambda)$ is an important quantity. The data points are fit into the function

$$c_\lambda = a + b/(1 - \lambda), \quad (6.30)$$

via a and b , and the fitted set of parameters are $(4.52, 1.38)$ and $(3.76, 1.48)$ for λ greater and less than one respectively. The divergence of c_λ at $\lambda = 1$ leads to the possibility of a reduction of the slope of S^{vN} from 3 to $3/2$ when plotted against $\ln \kappa$.

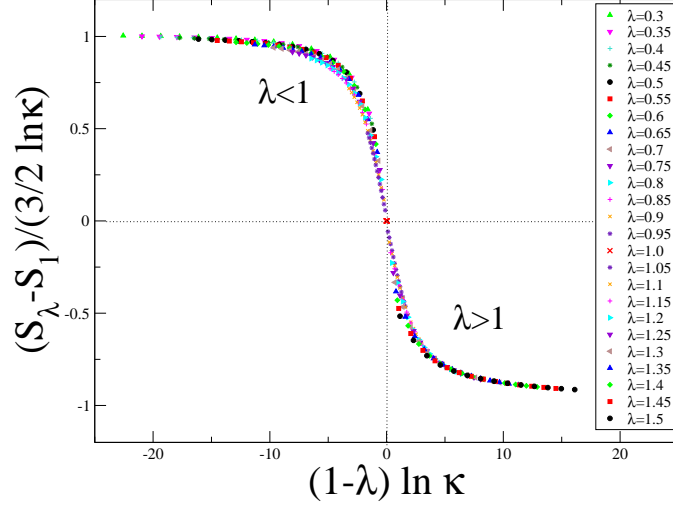


Figure 6.5: Data collapse: $(S_\lambda^{vN} - S_1^{vN})/\frac{3}{2} \ln \kappa$ vs $(1 - \lambda) \ln \kappa$.

Data collapse

We noted that for $\lambda > 1$, c_λ and hence the entropy itself, has a $(1 - \lambda)$ dependence and for $\lambda < 1$, the entropy has a $\ln \kappa$ term with $c_\lambda = f(1 - \lambda)$. It was pointed out in Sec III, below Eq.(6.25) that $(1 - \lambda) \ln \kappa$ seems to be a scaling variable. We therefore look at the plot of the entropy *vs.* $(1 - \lambda) \ln \kappa$. The entropy has different behaviors on the two sides of the $\lambda = 1$ making it a special point. Also, it has a separate scaling behavior. This drives us to plot $(S_\lambda^{vN} - S_1^{vN})/(\frac{3}{2} \ln \kappa)$ against $(1 - \lambda) \ln \kappa$. We see a good data collapse (see Fig. 6.5) for various sets of data of Fig 6.2. Hence, one can write the scaling form of von Neumann entropy:

$$(S_\lambda^{vN} - S_1^{vN})/\frac{3}{2} \ln \kappa = \mathcal{F}((1 - \lambda) \ln \kappa). \quad (6.31)$$

Fig. 6.5 shows that $(S_\lambda^{vN} - S_1^{vN})/\frac{3}{2} \ln \kappa$ reaches +1 for small enough κ for $\lambda < 1$ and -1 for $\lambda > 1$. Once we get the scaling behavior of the entropy at $\lambda = 1$, the same away from this special point can also be obtained.

6.4.3 Behaviour of the Renyi entropy

The Renyi entropy is calculated by using the same wave function and the same MATHEMATICA program, by using the formula of the Renyi entropy that,

$$S_n = \frac{1}{1-n} \ln \text{Tr} \rho^n \quad \text{with} \quad \rho = |\phi(q)|^2. \quad (6.32)$$

The limit $n \rightarrow 1$ gives the von Neumann entropy. The entropy is calculated for various λ , for $\lambda < 1$, $\lambda = 1$ and $\lambda > 1$, near $n = 1$.

λ dependence

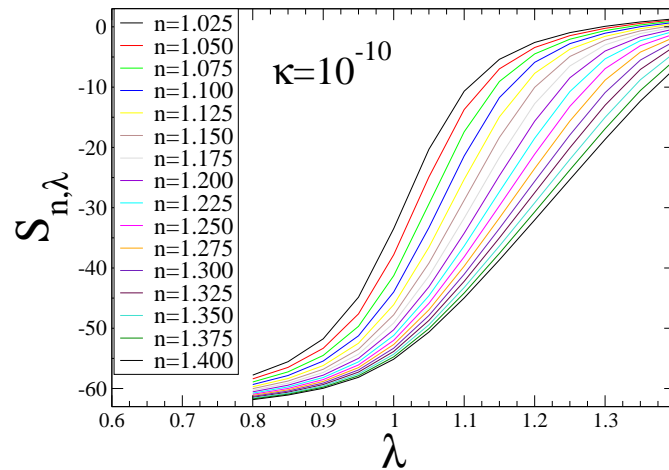


Figure 6.6: Renyi entropy: plot of S_n against λ for various n .

The Renyi entropy, when plotted against λ for various n , looks similar to that of the von Neumann entropy. All the curves merge after a certain value of λ , for $\lambda > 1.4$, and the Renyi entropy becomes positive. Similarly for $\lambda < 1$, all the curves saturate to an n -dependent constant. Fig. 6.6 shows the variation of the Renyi entropy with λ for $\kappa = 10^{-10}$. As κ decreases, the saturation value becomes more negative for $\lambda < 1$. This indicates that eventually it goes to negative infinity in the limit $\kappa \rightarrow 0$. At $\lambda = 1$, the divergence of the Renyi entropy depends on the value of n .

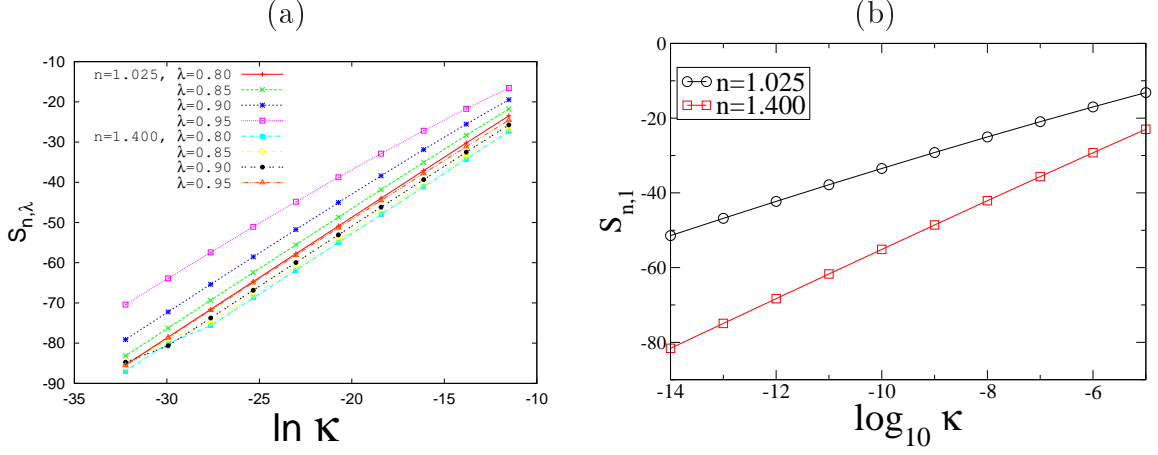


Figure 6.7: $S_{n,\lambda}$ vs. $\log \kappa$ for (a) $\lambda < 1$ and (b) $\lambda = 1$. For the both, $S_{n,\lambda}$ is linear in $\log \kappa$. For (a), slope is 3 and for (b) slope varies with n .

κ dependence

The diverging behaviour becomes more evident when one plots the Renyi entropy against κ (Fig. 6.7 a,b, and Fig. 6.8). For $\lambda < 1$, the curves of S_n vs. $\ln \kappa$ are linear with slope 3 (see Fig. 6.7(a)). For $\lambda = 1$, the slope is not fixed but changes with n (see Fig. 6.7(b)). The variation of the coefficient of $\ln \kappa$ with n is shown in Fig. 6.9(b).

For $\lambda > 1$, one finds a κ -independent entropy below some critical value of n , n_c , which again depends on the value of λ (see Fig. 6.8 a,b).

n dependence

In addition, we show, in Fig. 6.10, the n -dependence of the Renyi entropy for the three ranges of λ , viz., $\lambda < 1$, $\lambda = 1$ and $\lambda > 1$. The nature of the curves changes because of the extra n -dependence in the coefficient of $\ln \kappa$ for $\lambda = 1$.

Fig. 6.9(a) shows the behaviour of the additive κ -independent constant $c_{n,\lambda}$ for $\lambda = 1$ (see Eq.(6.33)).

The existence of a cut-off n_c , below which the entropy S_n is independent of κ , becomes evident from the plot of coefficient of $\ln \kappa$ vs. n as shown in Fig. 6.11(a). The value of n_c seems to vary with λ in a linear fashion, $n_c = \lambda - 0.1$, for $\lambda > 1$ (see Fig. 6.11(b)).

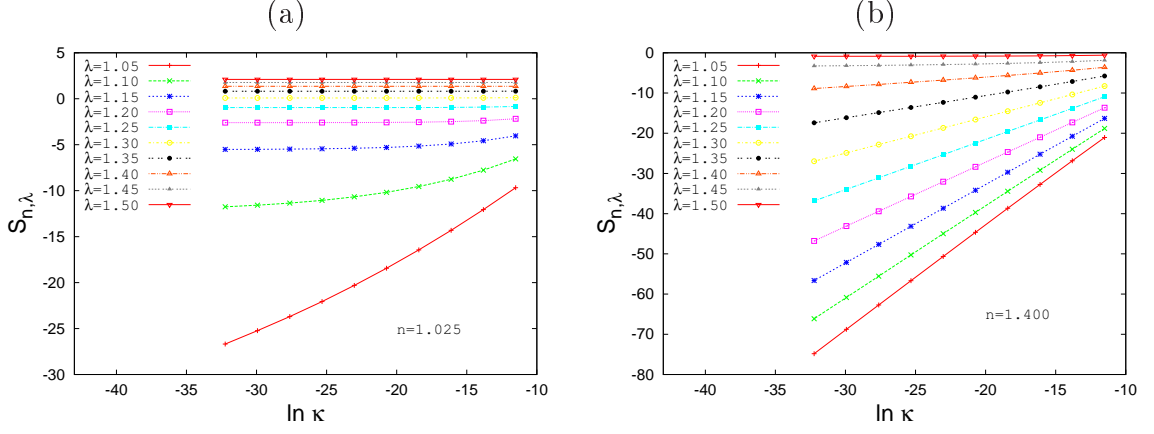


Figure 6.8: $S_{n,\lambda}$ vs. $\ln \kappa$ for $\lambda > 1$, for (a) $n = 1.025$ and (b) $n = 1.400$. $S_{n,\lambda}$ is independent of λ below some n_c .

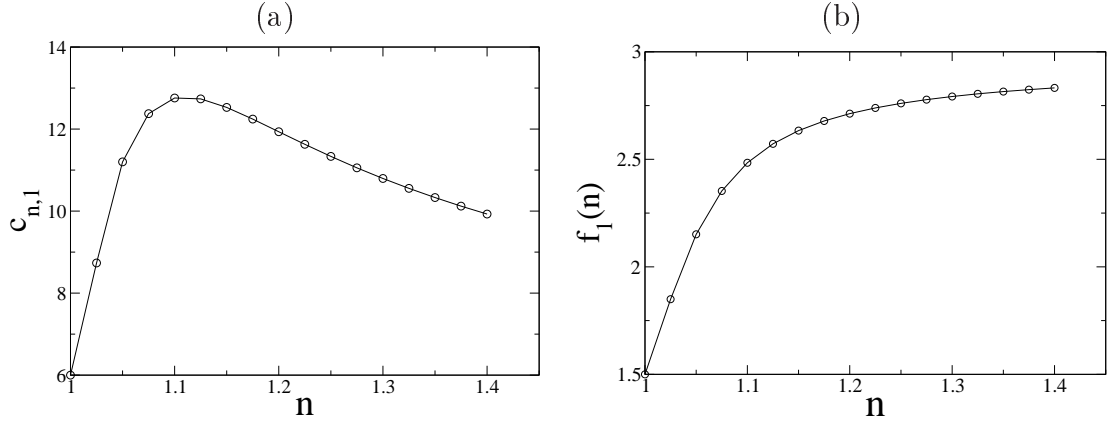


Figure 6.9: The plots show (a) $c_{n,\lambda}$ vs. n , and (b) $f_1(n)$ (coefficient of $\ln \kappa$, see Eq.(6.33)) vs. n , both for $\lambda = 1$.

Combining the results for all λ for the Renyi entropy, we then write,

$$S_n = \begin{cases} 3 \ln \kappa + c_{n,\lambda}, & \text{for } \lambda < 1, \\ f_1(n) \ln \kappa + c_n, & \text{for } \lambda = 1, \\ \begin{cases} c_{n,\lambda}, & \text{for } \lambda > 1, \quad n < n_c(\lambda), \\ f_\lambda(n) \ln \kappa + c_{n,\lambda}, & \text{for } \lambda > 1, \quad n > n_c(\lambda). \end{cases} \end{cases} \quad (6.33)$$

A scaling form of the Renyi entropy involving an n_c and n -dependent coefficient of $\ln \kappa$ is expected, but yet unknown.

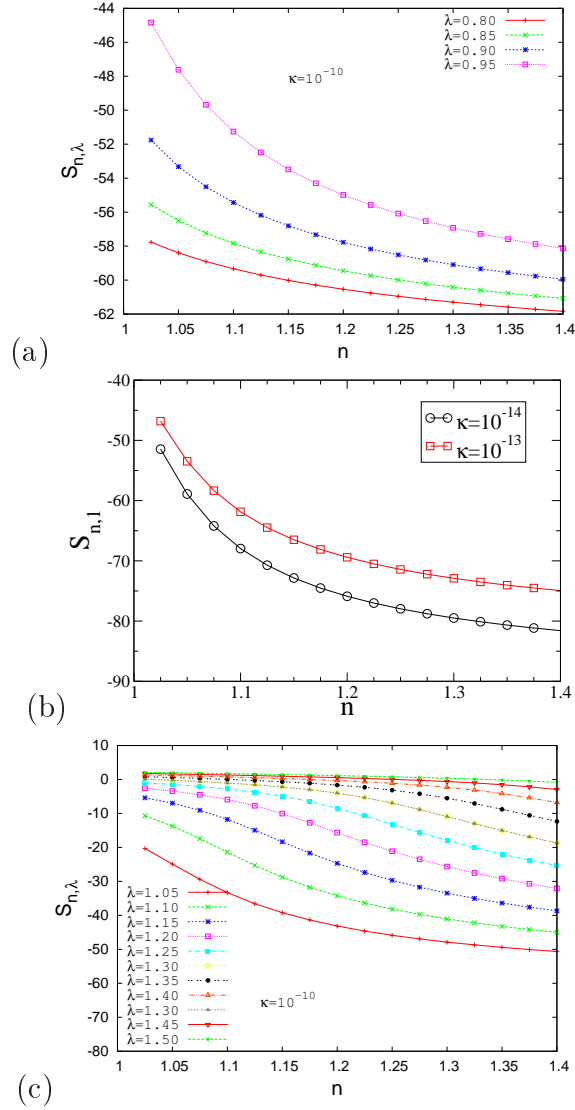


Figure 6.10: Plot of S_n vs. n for different λ values, (a) $\lambda < 1$, (b) $\lambda = 1$ and (c) $\lambda > 1$. For (a) and (c), $\kappa = 10^{-10}$, while for (b) $\kappa = 10^{-13}$ and $\kappa = 10^{-14}$.

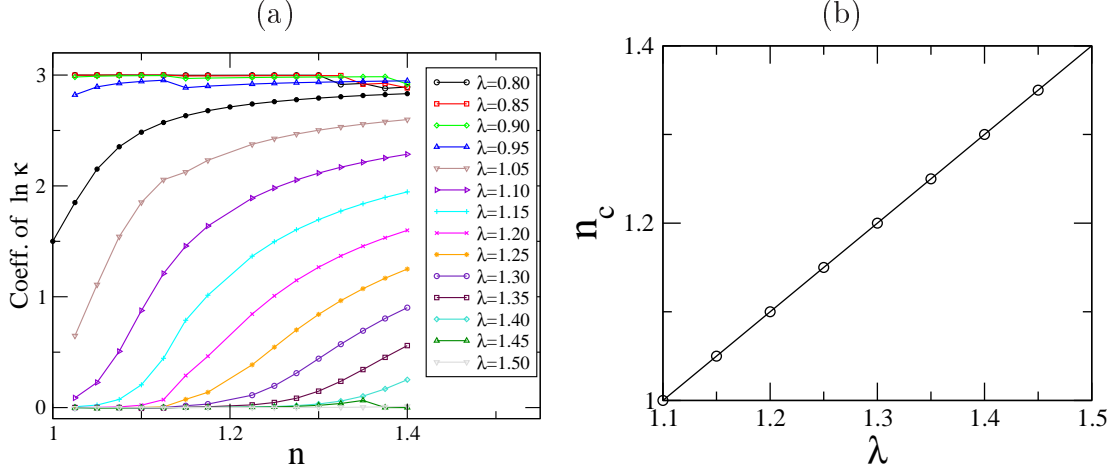


Figure 6.11: (a) The plot shows $f_\lambda(n)$ vs. n (coefficient of $\ln \kappa$, see Eq.(6.33)). It shows the existence of a special value of n , below which the Renyi entropy S_n is independent of κ . (b) The variation of n_c with λ .

6.5 Discussion and conclusion

In this chapter we studied the von Neumann entropy S^{vN} and the Renyi entropy S_n , the most common measures of the entanglement entropy, for an inverse square potential in three dimensions.

The von Neumann entropy behaves in different ways for three different ranges of modified interaction strength λ and given by Eq. (6.29). For $\lambda < 1$ and $\lambda = 1$, the entropy has a diverging nature as one approaches quantum critical point by tuning κ , except for $\lambda = 1$ the prefactor is different from that for $\lambda < 1$. The behavior of entropy is completely different for $\lambda > 1$, where the κ -dependence of the entropy vanishes. There is a $\frac{1}{1-\lambda}$ divergence in the entropy. These three distinct classes collapse onto a single curve when $(S_\lambda^{vN} - S_1^{vN})/\frac{3}{2} \ln \kappa$ is plotted against $(1-\lambda) \ln \kappa$. This data collapse indicates that there is a common scaling behavior of the entropy for any λ and that $\lambda = 1$ is special. Because of the dependence of the diverging factor on $(1-\lambda)$, one has to be careful in taking the required limit of $\kappa \rightarrow 0$ as that would give a log correction in entropy for $\lambda = 1$. For $g > 1/4$, λ is imaginary which we do not consider here. Here we focused on the multicritical point at $\lambda = 1$. There is one more multicritical point at $\lambda = 0$ with KT transition which has not been studied so far.

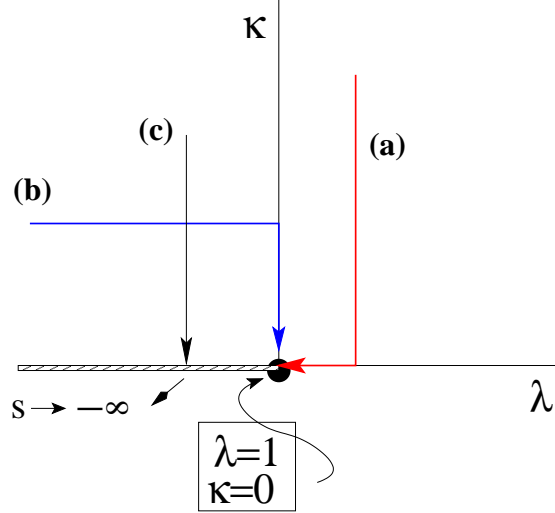


Figure 6.12: The path dependence of entropy. Two different limits of approaching $\{\lambda = 1, \kappa \rightarrow 0\}$. (a) First $\kappa \rightarrow 0$ and then $\lambda = 1$ (red line). The entropy diverges like $1/(1 - \lambda)$. (b) First $\lambda \rightarrow 1$ and then $\kappa \rightarrow 0$ (blue line). The entropy diverges like $\ln \kappa$. Thick line along x -axis for $\lambda \leq 1$ denotes divergent entropy. (c) For $\lambda < 1$, taking the limit $\kappa \rightarrow 0$ (black vertical line with arrow) leads to divergent entropy and S^{vN} remains so along the horizontal stretch.

The nature of the divergence of the entanglement entropy at $\lambda = 1$ depends on the path of approaching $\lambda = 1$ in a λ - κ plane. Diagrammatically it has been shown in Fig. 6.12. If we take the limit $\kappa \rightarrow 0$ first and then $\lambda = 1$, the entropy diverges like $1/(1 - \lambda)$ (shown by red line (a) in Fig. 6.12), and like $\ln \kappa$ for the other way around (see the blue line (b) in the same figure). For $\lambda < 1$, the $\kappa \rightarrow 0$ line corresponds to $S^{vN} = -\infty$, but for $\lambda > 1$ the same line gives a finite value for entropy. The path dependence of Fig. 6.12 summarizes the features of the entanglement entropy, with $\lambda = 1, \kappa = 0$ as a special point controlling the behavior in its neighborhood. The data collapse of Fig. 6.5, then, suggests that the paths should be classified by the constant value of $X = (1 - \lambda) \ln \kappa$.

The Renyi entropy is studied for the same interaction. The behaviour for $\lambda < 1$ is same as the von Neumann entropy, i.e., for $\lambda < 1$, the Renyi entropy is of the form, $S_n = 3 \ln \kappa + c_{n,\lambda}$. The origin of an extra n -dependence in the behaviour of $\lambda = 1$, $S_n = f(n) \ln \kappa + c_\lambda$, is not very clear. Like the von Neumann entropy, S_n is independent of λ above some n_c . We find a linear dependence of n_c on λ . One

would then expect an n -dependent scaling of the Renyi entropy.

For $\lambda < 1$, restricting to the critical case, we see $\rho(q) \sim |\phi(q)|^2$. These are the eigenvalues of the density matrix. Now the reduced density matrix ρ describes a mixed state, though the full ground state is pure. Being a mixed state, we may represent ρ as a ‘‘thermal’’ density matrix, $\rho \sim \exp(-\beta H_{ent})$, as done in Eq.(6.6). Since the entanglement spectrum is known, we have

$$\beta H_{ent} \approx \ln |{}_2F_1|^2 \approx \frac{1}{2} \frac{q^2}{\kappa^2}, \quad \text{for } q \rightarrow 0, \quad (6.34)$$

identifying $\beta = 1/\kappa^2$ and $H_{ent} = q^2/2$. As mentioned before for this Hamiltonian $S^{vN} = \frac{d}{2} \ln T$. Since in this case $T \simeq \kappa^2$, we find $S^{vN} \sim d \ln \kappa$.

What next: In the next chapter, we study the stochastic paths viewing polymers length as time. A polymer then can be considered as a random walker. The problem of random walk is itself is a vast area of study. We concentrate on the effect of the random medium on the mean square displacement, correlation and the persistence of the random walker in a disordered medium.

Appendix : Calculation of the normalization constants A and B

The normalization constants A and B are found using the continuity condition and taking limit $\kappa \rightarrow 0$, that

$$4\pi \left[\int_0^a |A|^2 \sin^2 kr \, dr + \int_a^\infty r |B^2 H_\lambda^{(1)2}(i\kappa r)| \, dr \right] = 1.$$

The continuity condition, Eq.(6.14), replacing A by B ,

$$\left[\left(2\pi a - \frac{\pi}{k} \sin 2ak \right) \frac{|H_\lambda^{(1)}(i\kappa a)|^2}{\sin^2 ka} + 4\pi \int_a^\infty r |H_\lambda^{(1)}(i\kappa r)|^2 \, dr \right] |B|^2 = 1. \quad (6.35)$$

Now we use the form of the Hankel function in the limit $\kappa \rightarrow 0$,

$$|H_\lambda^{(1)}(i\kappa r)|^2 \sim \frac{2^\lambda \Gamma^2(\lambda)}{\pi^2} r^{-2\lambda}, \quad (6.36)$$

and rewrite the outer part integral in the normalization condition in a simpler form,

$$\begin{aligned}
 & \int_{\kappa a}^{\infty} r |H_{\lambda}^{(1)}(ir)|^2 dr \\
 = & \int_{\kappa a}^1 \left[|H_{\lambda}^{(1)}(ir)|^2 - \frac{2^{\lambda} \Gamma^2(\lambda)}{\pi^2} r^{-2\lambda} \right] dr + \int_{\kappa a}^1 \frac{2^{\lambda} \Gamma^2(\lambda)}{\pi^2} r^{-2\lambda} dr + \int_1^{\infty} r |H_{\lambda}^{(1)}(ir)|^2 dr \\
 = & \frac{\Gamma^2(\lambda)}{\pi^2} \frac{1 - (a\kappa)^{2(1-\lambda)}}{1 - \lambda} + \dots \tag{6.37}
 \end{aligned}$$

Putting Eqs.(6.37) and (6.36) in the Eq.(6.35) after simplification one gets,

$$|B|^2 = \frac{\pi}{2^{\lambda+1} \Gamma^2(\lambda)} \left[\left(\frac{\lambda^2 + a^2 k^2 - 1/4}{a k^2} \right) (a\kappa)^{-2\lambda} + \frac{1}{\kappa^2} \frac{1 - (a\kappa)^{2(1-\lambda)}}{(1 - \lambda)} \right] \tag{6.38}$$

which in the extreme limit of $\kappa \rightarrow 0$ gives the κ dependence of B ,

$$|B|^2 \sim \begin{cases} \kappa^2, & \text{for } \lambda < 1, \\ \kappa^2 (a\kappa)^{2\lambda-2}, & \text{for } \lambda > 1. \end{cases} \tag{6.39}$$

Once B is obtained, the κ -dependence of the other constants A can be found using the continuity condition,

$$|A|^2 \sim \begin{cases} (a\kappa)^{2-2\lambda}/a, & \text{for } \lambda < 1, \\ 1/a, & \text{for } \lambda > 1. \end{cases} \tag{6.40}$$

List of symbols

A, B	Normalization constants of the wave function
a	Width of the potential
\mathbf{p}, q	Momentum
d	Dimension
g	Strength of $1/r^2$ potential
H_{ent}	Entanglement Hamiltonian
H	Hamiltonian
$ k\rangle$	Basis of momentum states
λ	Reduced strength of $1/r^2$ potential
m	Mass
μ	Reduced mass
N	Length of polymer
Ω	Reunion partition function
Ψ	Reunion exponent of two polymers
r	Relative distance
σ_0	Bubble entropy per unit length
S^{vN}	von Neumann entropy
S_n	Renyi entropy
T	Temperature
t	Time
u	Dimensionless short range potential
V_0	Depth of the potential well
V	Potential
Z	Partition function

7

Random walks in disordered media

Anomalous diffusion arising from broad waiting time distributions, has been used to model a variety of physical phenomena. For example, dynamics of carrier diffusion and recombination in disordered media, the electrical properties of disordered media, photo-conductivity of amorphous insulating materials, frequency dependent conductivity of hollandite etc. have been described in terms of a continuous time random walk (CTRW) [48]-[118].

Many physical situations are encountered which can be modeled as random walks in quenched disordered media, e.g., conductivity of amorphous materials or quasi-one-dimensional ionic conductors, dynamics of domain walls or dislocations etc. In this chapter, we study the random walk with a power law distribution of transition rates in which the spreading becomes subdiffusive [119]-[123], namely,

$$\langle x^2(t) \rangle \sim t^{2\beta}, \quad \text{with } \beta < 1/2. \quad (7.1)$$

This chapter is organized as follows. In Sec. 7.1 we discuss the model and its relevance to physical systems. The results are discussed in Sec. 7.2. Considering four models of disorders, the behaviour of the mean square displacement, the waiting time distribution, two time correlation function and the persistence probability are observed in this section. In Sec. 7.2.5 we try to give explanations to the anomalous behaviour of the persistence probability of one of those four models.

7.1 Lattice models and simulations

The random walk is performed on a 1D regular lattice of L sites, with periodic boundary conditions, i.e., the site $i = L + 1$ is identified with the first site $i = 1$. Only hopping between nearest neighbor sites are allowed and the hopping rates $W_{i,j}$ are chosen from the power law distribution Eq. (1.60). This is carried out numerically by first generating a uniform random number r in the interval $[0, 1]$ and using the transformation $w = r^{1/(1-\alpha)}$ with suitable rescaling by a constant. There are two standard choices in assigning the hopping rates $W_{i,j}$ between two neighbouring sites, namely,

(i) Random barrier model or bond disorder (RB): Hopping rates are assigned to the bonds, $W_{i,i+1} = W_{i+1,i}$. I.e. the transition rate from i to $i + 1$ is the same as the rate for the reverse transition and thus bond connecting two neighboring sites acts as a symmetrical barrier (Fig. 7.1)

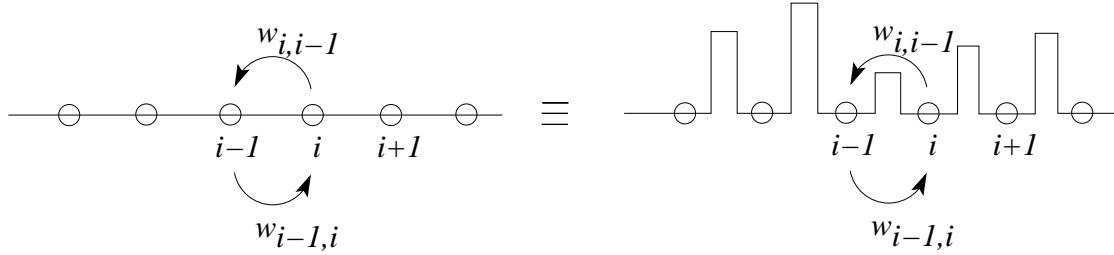


Figure 7.1: The bond disorder or random barrier model. In this model the hopping rate $W_{i,i-1} = W_{i-1,i}$.

(ii) Random trap model or site disorder (RS): Random hopping rate is assigned to each site which acts as a trap, $W_{i,i+1} = W_{i,i-1}$. I.e. the transition rate from a site i is independent of the target site ($i \pm 1$) and once the random walker comes out of the trap it has equal probability to jump to either of the two neighboring sites (Fig. 7.2).

Further, for each of the above type of assignment of transition rates one can define further an *annealed* or a *quenched* model. In the annealed models, a new transition rate $W_{i,j}$ is assigned each time the walker visits a site i . In the quenched models, a set of $W_{i,j}$'s for the entire lattice is chosen at the beginning of the simulation and is referred to as a *disorder realization*.

Hence, we have **four** models, namely, (a) Annealed Site disorder (AS), (b)

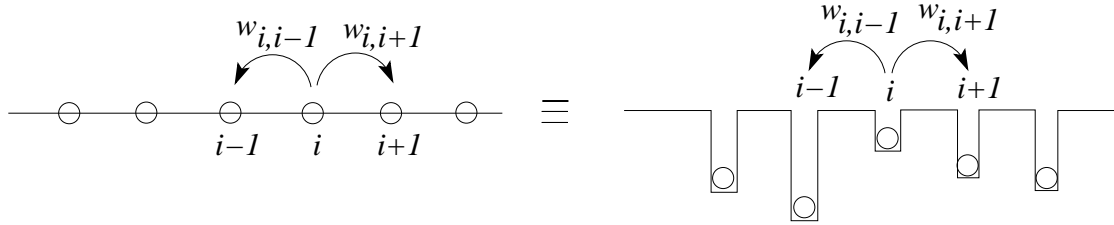


Figure 7.2: The site disorder or random trap model. In this model the hopping rate $W_{i,i-1} = W_{i,i+1}$.

Annealed Bond disorder (AB), (c) Quenched Site disorder (QS) and (d) Quenched Bond disorder (QB).

In each Monte Carlo Step (MCS), the random walker at site i makes an attempt to jump to either neighbouring site ($j = i \pm 1$) with a probability proportional $W_{i,j}$. All the Monte Carlo simulations have been performed on a lattice of $L = 10^3$ sites with periodic boundary condition. The random walker starts at an arbitrarily chosen site at $t = 0$ and the simulations are carried out for a typical maximum time $T \sim 10^6 \text{ MCS}$. For the annealed models, the observed quantities are averaged over all initial conditions randomly chosen with equal weight. For the quenched models, a further averaging over disorder realizations is done (typically 10^3 samples).

The difference between quenched disorder and annealed disorder models lies in the fact that the mean waiting time at a given site is the same for each visit of the site for the quenched models, thus inducing strong correlations between the successive waiting times encountered. It makes the quenched problem more difficult to analyze.

7.1.1 Relevance to real systems

The choice of power law distribution of hopping rates find many applications in modeling various physical systems. Some examples are following [113]:

- (i) The temperature dependence of the dynamical conductivity exponent observed in the one-dimensional superionic conductor hollandite [124].
- (ii) Continuum random systems such as the Swiss-cheese model can be mapped onto random percolation networks with a power-law distribution of bond conductivities [125].
- (iii) The problem of biased diffusion in random structures such as the random

comb or the percolation system can be modeled by biased diffusion in a linear chain with a power-law distribution of transition rates [126, 127].

(iv) Anomalous relaxation in spin glasses can be interpreted in terms of stochastic motion in phase space with a power-law distribution of transition rates [128, 129].

7.2 Numerical results

We present below, the numerical results for the mean square displacement $\langle x(t)^2 \rangle$, waiting time distribution $\omega(\tau)$, two-time incremental correlation function $C(t_1, t_2)$ and persistence probability $P(t)$ for all the four models for 10 values of α in the interval $[0, 1]$.

7.2.1 Mean square displacement $\langle x^2(t) \rangle$

The disorder averaged square displacement $\langle x^2 \rangle$ for all cases can be written in a general form:

$$\langle x^2 \rangle \sim t^{2\beta}. \quad (7.2)$$

The wandering or spreading exponent β for the four models we consider are known from various analytical arguments [67, 69, 48], which are verified by our numerical results.

1. Annealed bond disorder: $\beta = \begin{cases} \frac{1}{2}, & 0 \leq \alpha < \frac{1}{2}, \\ 1 - \alpha, & \alpha > \frac{1}{2}, \end{cases}$
2. Annealed site disorder: $\beta = \frac{1-\alpha}{2}, \quad 0 \leq \alpha < 1,$
3. Quenched bond disorder: $\beta = \frac{1-\alpha}{2-\alpha}, \quad 0 \leq \alpha < 1,$
4. Quenched site disorder: $\beta = \frac{1-\alpha}{2-\alpha}, \quad 0 \leq \alpha < 1.$

7.2.2 Waiting time distribution $\omega(\tau)$

The distribution of the hopping rates, $\rho(W) \sim W^{-\alpha}$, in turn produces a waiting time distribution $\omega(\tau) \sim \tau^{-\mu}$. For the annealed models and the quenched site model, the waiting time distribution $\omega(\tau)$ and $\rho(W)$ are simply related, since the

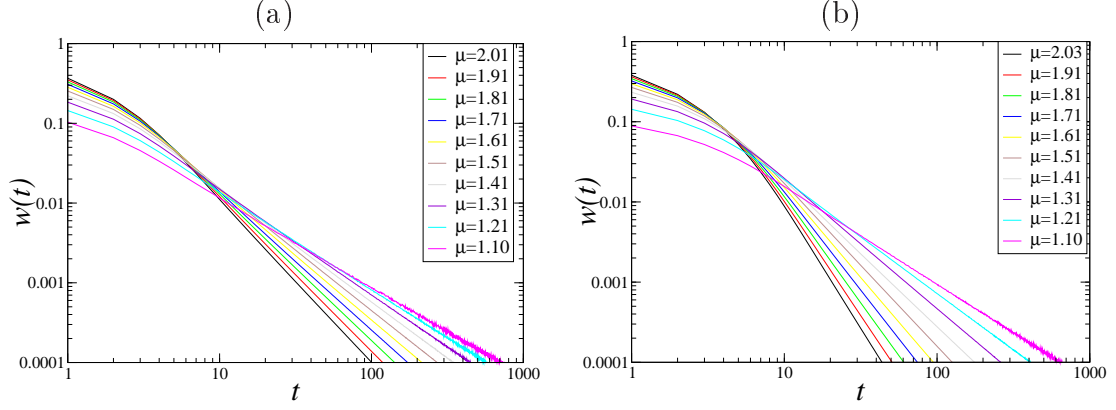


Figure 7.3: The waiting time distribution $\omega(\tau)$ vs. τ for (a) annealed site disorder and (b) annealed bond disorder for different α .

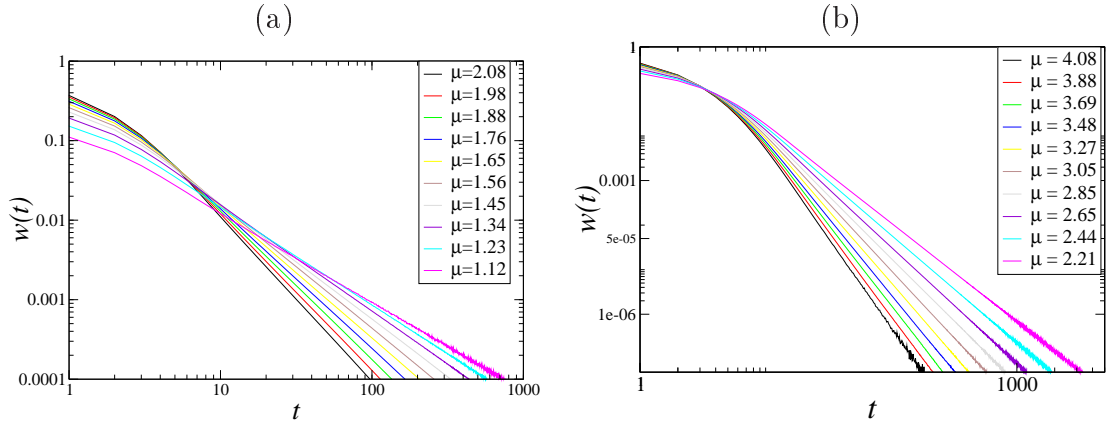


Figure 7.4: The waiting time distribution $\omega(\tau)$ vs. τ for (a) quenched site disorder and (b) quenched bond disorder for different α .

random walk encounters the barriers or traps with the same probability they are chosen from. Thus, for the annealed and quenched site (AS, QS) models we have $\omega(\tau)d\tau = \rho(W)dW$ and with $\tau = 1/W$, we obtain $\mu = 2 - \alpha$. For the annealed bond disorder (AB), the mean waiting time τ at a given site i is related to the transition rates of two bonds on either side as $\tau^{-1} = W_{i,i-1} + W_{i,i+1}$. This results in a mean waiting time distribution with $\mu = 3 - 2\alpha$. For the quenched bond (QB) disorder a large τ would result when $(W_{i-1,i} + W_{i,i+1})^{-1}$ is large, i.e. for a valley enclosed by two large barriers (Fig. 7.1). But these are difficult to reach as well and hence are sampled less in quenched bond disorder model. In this case the bonds are not sampled according to the original disorder distribution and thus the

waiting time distribution can not be related to $\rho(W)$ as simply [48].

We find that the waiting time distributions found in our numerical simulations are consistent with the analytical predictions:

$$\omega(\tau) = \begin{cases} \tau^{-(3-2\alpha)} & \text{for annealed bond (AB),} & (7.3a) \\ \tau^{-(2-\alpha)} & \text{for annealed site (AS),} & (7.3b) \\ \tau^{-(4-2\alpha)} & \text{for quenched bond (QB),} & (7.3c) \\ \tau^{-(2-\alpha)} & \text{for quenched site (QS).} & (7.3d) \end{cases}$$

Figs. 7.3 and 7.4 show the variation of waiting time distribution with time. The value of β obtained in the previous section for the cases AB, AS are consistent with the above results for the waiting time distribution ($\beta = \frac{\mu-1}{2}$). For the QS problem, it can be seen that even though the waiting time distribution is the same as that for AS, the exponents β in the two cases are different. This is a consequence of the temporal correlations induced due to the quenched randomness in the model. For the AB model, for $0 \leq \alpha < \frac{1}{2}$, $\mu > 2$ and thus one gets normal diffusion, which is consistent with the value of β observed for this regime.

7.2.3 Two point incremental correlation function $C(t_1, t_2)$

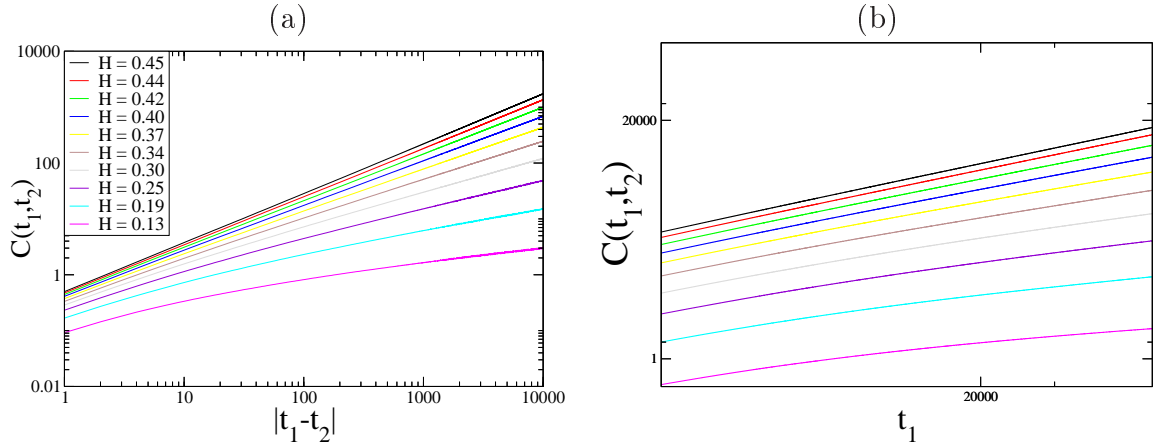


Figure 7.5: (a) Plot of $C(t_1, t_2)$ vs. $|t_1 - t_2|$ for quenched bond disorder. Here H denotes the Hurst exponent. (b) Plot of $C(t_1, t_2)$ vs. t_1 for quenched site disorder. Here t_2 is kept fixed and region of interest in $t_1 \gg t_2$.

Although all of the models studied have similar scaling behaviour, the two point

incremental correlations behave qualitatively differently. For annealed disorder, the form of two point incremental correlation is known from a representation in terms of coupled Langevin equations as shown by Baule *et al.* The two-point correlation for quenched disorder is not analytically known. The same for annealed disorder displays the non-stationary character of the CTRW process. For annealed bond and annealed site disorder it is expected to be $|t_1^{2\beta} - t_2^{2\beta}|$ and from simulations we do get results consistent with these. Further, for quenched site disorder we see the same behaviour of two-point correlation (see Fig. 7.5(b)) whereas for quenched bond disorder

$$C(t_1, t_2) \sim |t_1 - t_2|^{2\beta},$$

for long times. To show the stationarity more clearly, we plot $C(t_1, t_2)$ against $|t_1 - t_2|$ in Fig. 7.5(a). In log scale, this plot is a straight line for large $|t_1 - t_2|$. For the other case, we take $t_1 \gg t_2$ and keep t_2 fixed, and plot against t_1 . The reason of plotting against t_1 is that, in this limit,

$$|t_1^{2\beta} - t_2^{2\beta}| = t_1^{2\beta} \left| 1 - \left(\frac{t_2}{t_1} \right)^{2\beta} \right| \sim t_1^{2\beta}. \quad (7.4)$$

We see, only quenched bond disorder has a stationary two point incremental correlation while others have decaying correlations. The stationarity can be observed in the plot of $C(t_1, t_2)$ vs. t_1 for fixed $|t_1 - t_2|$. Hence, in spite of having the same scaling behaviour of the mean square displacement with the same dynamic exponent β , $C(t_1, t_2)$ behaves qualitatively differently for the quenched bond disorder.

7.2.4 Persistence probability

Figs. 7.6 and 7.7 are the log-log plots of $P(t)$ vs. t for different models of disorder. In each graph there are ten data sets for ten different α values. Asymptotically, these plots are straight lines with slope θ which is extracted for each data set using standard fitting routines. In Fig. 7.8, exponents θ and β are plotted against α simultaneously. It is observed that the persistence exponent θ is equal to the corresponding β in all cases except for quenched bond disorder, in which case

$$\theta = \min(1 - \beta, 2\beta).$$

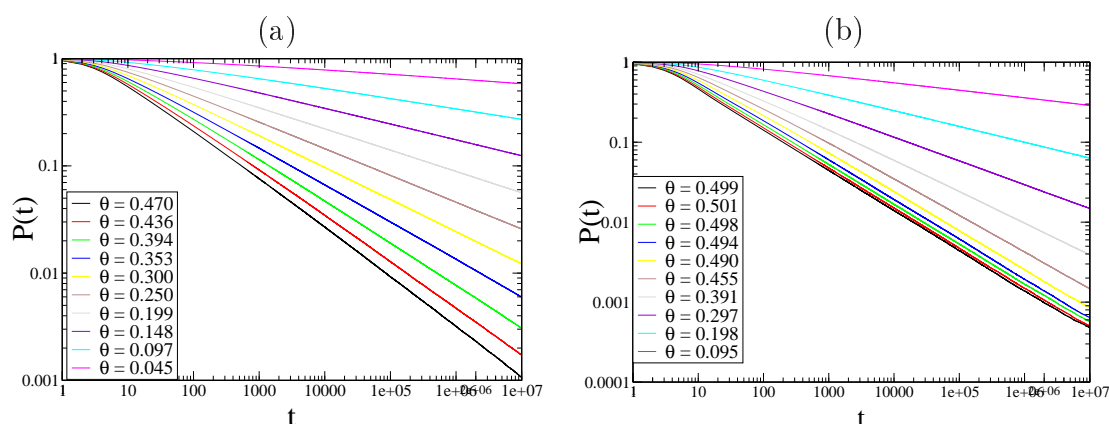


Figure 7.6: Persistence probability $P(t)$ vs. t for (a) annealed site disorder and (b) annealed bond disorder for different α .

The main result of our work is this observation and possible explanations for this qualitatively nontrivial result.

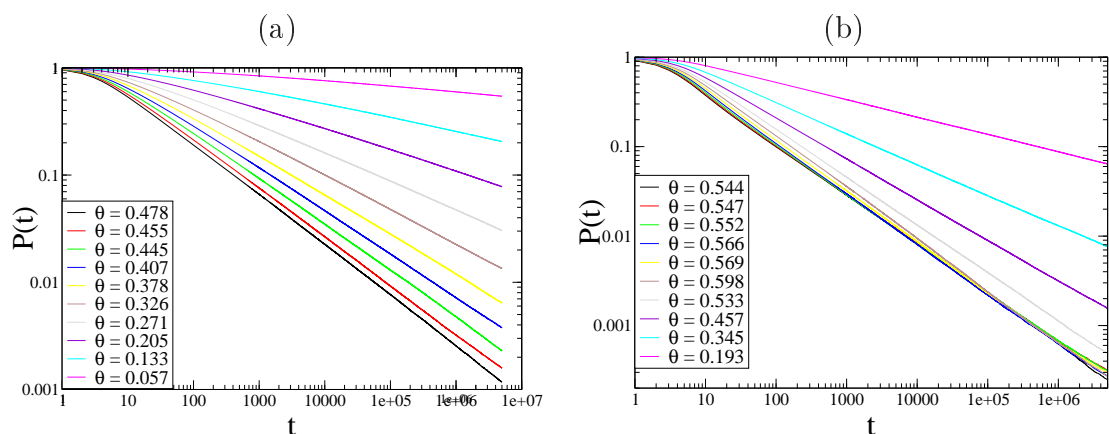


Figure 7.7: Persistence probability $P(t)$ vs. t for (a) quenched site disorder and (b) quenched bond disorder for different α .

We put together all the exponents related to the diffusion, waiting time, two-time correlation function and persistence for all the four models in table 7.1.

7.2.5 Explanation of the observed $P(t)$

As the value of α increases, the probability of encountering deep traps or high barrier increases resulting in trapping of the random walker. This decreases the probability of coming back to the starting point. Thus, one would normally expect

	Annealed		Quenched	
	Bond	Site	Bond	Site
$\langle x^2 \rangle$	$t^{0.5}; 0 < \alpha < \frac{1}{2}$ $t^{2\beta}; \frac{1}{2} < \alpha < 1$ $\beta = 1 - \alpha$	$t^{2\beta}; 0 < \alpha < 1$ $\beta = \frac{1-\alpha}{2}$	$t^{2\beta}; 0 < \alpha < 1$ $\beta = \frac{1-\alpha}{2-\alpha}$	$t^{2\beta}; 0 < \alpha < 1$ $\beta = \frac{1-\alpha}{2-\alpha}$
$\omega(\tau)$	$\tau^{-(3-2\alpha)}$	$\tau^{-(2-\alpha)}$	$\tau^{-(4-2\alpha)}$	$\tau^{-(2-\alpha)}$
$C(t_1, t_2)$	$ t_2^{2\beta} - t_1^{2\beta} $	$ t_2^{2\beta} - t_1^{2\beta} $	$ t_1 - t_2 ^{2\beta}$	$ t_2^{2\beta} - t_1^{2\beta} $
θ [$P(t) \sim t^{-\theta}$]	β	β	$\min(1-\beta, 2\beta)$	β

Table 7.1: The table shows the forms and values of different quantities of interest in the four types of disorder models: annealed bond, annealed site, quenched bond, and quenched site disorder cases. The quantities in gray are known from earlier works and confirmed by our simulations. The remaining data are from our simulations. The quenched bond disorder case has entirely different persistence and correlation properties from the other three models.

this would result in increase of persistence probability and hence decrease in the exponent θ . This, indeed, is what is observed in the three types of disorder, and for the quenched bond disorder for $\alpha > 1/2$. However, counter-intuitively, for the quenched bond disorder case with $\alpha < 1/2$, the persistence exponent actually increases with α (see Fig. 7.8). One could possibly argue that as the walker can not go farther with increasing α because of lower mean square displacement, it has higher probability to come back to the starting point. But this explanation fails for $\alpha > 1/2$ for the quenched disorder case and the other three models. By one of these or similar qualitative arguments, one would expect a monotonic θ - α plot. In the following, we use a number of different analytic and scaling arguments to explain the observed nontrivial dependence of θ and α .

Space-time rescaling

The simplest way to predict the persistence exponent in the disordered system, is to compare with the persistence probability $P_0(t)$ for the pure system via a straight

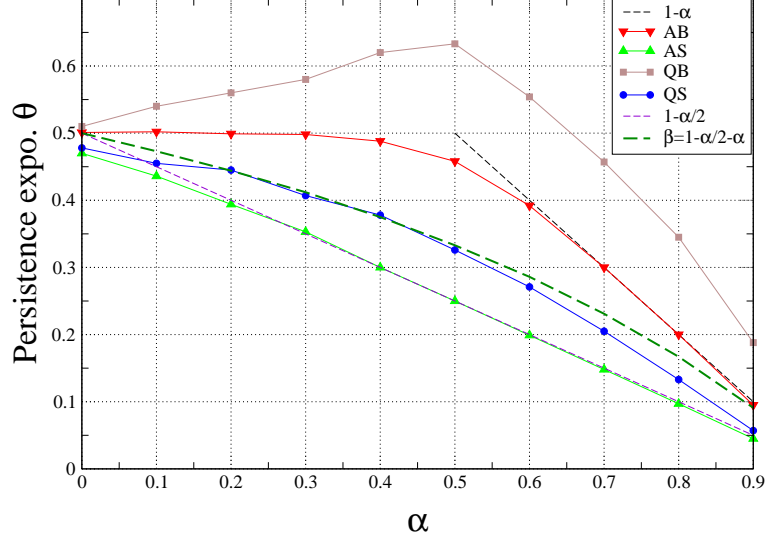


Figure 7.8: Persistence exponent θ vs. α for different models of disorder.

forward space-time rescaling. In a pure medium,

$$P_0(t) \sim \frac{1}{t^{\theta_0}}, \quad \text{with } \theta_0 = \frac{1}{2}. \quad (7.5)$$

For a random walk in an ordered medium, or for a normal Brownian motion, $t \sim \langle x^2 \rangle$. Thus, we rewrite $P_0(t)$ in terms of the $\langle x^2(t) \rangle$,

$$P_0(t) \sim \frac{1}{\langle x^2 \rangle^{\theta_0}}. \quad (7.6)$$

Now we use the scaling relation for $\langle x^2 \rangle$ in the disordered system to get the corresponding $P(t)$,

$$P(t) \sim \frac{1}{(t^{2\beta})^{\theta_0}} \sim \frac{1}{t^\beta}. \quad (7.7)$$

I.e., for the disordered system $\theta = \beta$. Surprisingly, this simple scaling argument works quite well as seen from the numerical results, in all cases, except for the quenched bond disorder case. Below, we put a couple of seemingly independent arguments to explain the nontrivial results for the quenched bond disordered case.

Fractional Brownian motion (fBm)

A process is termed as a fractional Brownian motion (fBm) if the asymptotic two point incremental correlation is stationary in time,

$$C(t_1, t_2) = \langle [x(t_1) - x(t_2)]^2 \rangle \sim |t_1 - t_2|^{2H}.$$

The exponent H is called the Hurst exponent. Depending on the value of H , the processes are divided into three types.

- (i) $H = 1/2$: normal Brownian motion,
- (ii) $H > 1/2$: a process with positively correlated increments,
- (iii) $H < 1/2$: a process with negatively correlated increments.

It is shown in [130, 131], that for an fBm, the persistence probability is given by $P(t) \sim t^{-(1-H)}$.

For the quenched bond disorder case we found that the two point incremental correlation function is: $C(t_1, t_2) \sim |t_1 - t_2|^{2\beta}$ for large $|t_1 - t_2|$. Thus, identifying the process as an fBm with Hurst exponent $H = \beta$, we predict the persistence exponent as $\theta = 1 - \beta$. This relation holds quite good for $\alpha < 1/2$ (Fig. 7.9).

However, for $\alpha > 1/2$, the prediction clearly does not hold. In the following subsection, we use the scaling arguments based on the first passage time to have a quantitative understanding of of the persistence exponent for $\alpha > 1/2$.

First passage time distribution (FPT)

The first return time problem can be decomposed into two first passage time problems. I.e. The random walk starts at x_0 at $t = 0$ and reaches a specified target x for the first time at $t = t'$ and then starting from x comes to X_0 at time $t = t$. Let us denote $F(x, t|x_0, t_0)$ as the probability that the walker reaches x for the first time at time instant t , starting from x_0 at time t_0 .

Here we recall that the first passage time is related to the survival probability $S(t)$, the probability that the walker *does not* reach to the specified point upto time t through

$$F(t) = -\frac{dS}{dt} \sim t^{-(1+\gamma)}.$$

We find numerically that $S(t)$ decays with a power law $S(t) \sim t^{-\gamma}$ and from the simulation results we find that $\gamma = \beta$ (see Fig. 7.9). Hence the first passage time

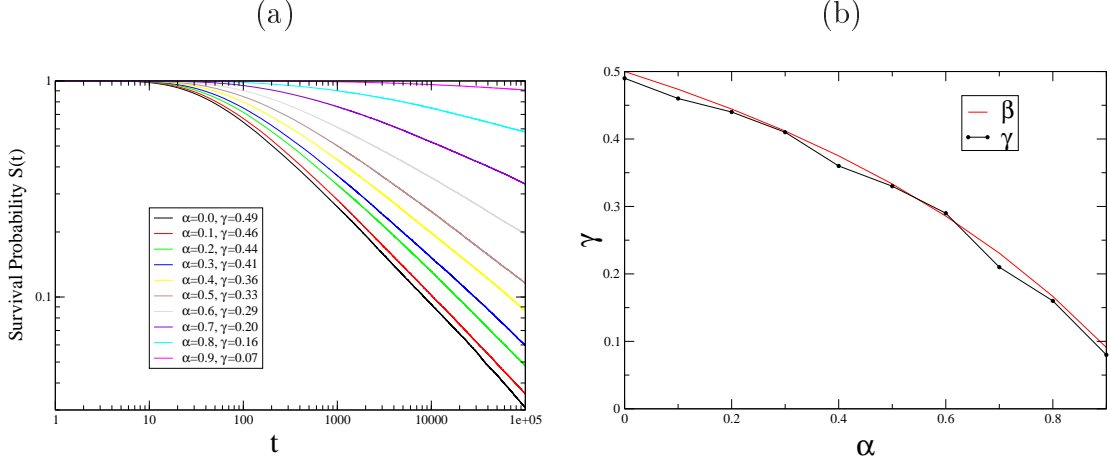


Figure 7.9: The survival probability for the quenched bond disorder. (a) The plot shows the survival probability with time in log-log plot. (b) This is the plot of the survival exponent γ for different α . Here, x -axis is the value of α and the y -axis is the survival exponent γ . The red curve shows the variation of β with α .

distribution is

$$F(x, t|x_0, t_0) \sim t^{-(1+\beta)}.$$

Thus, the first return probability density $N(t)$, that the walker comes back to the starting point, x_0 , for the first time at t , is

$$\begin{aligned} N(t) &= \int_0^t F(x_0 + \Delta, t'|x_0, 0) F(x_0, t|x_0 + \Delta, t') dt' \\ &= \int_0^t t'^{-(1+\beta)} (t-t')^{-(1+\beta)} dt' \\ &\sim t^{-(1+2\beta)}. \end{aligned} \quad (7.8)$$

This in turn yields the persistence probability $P(t)$, which is the probability that the walker reaches the target for the first time at $t' > t$ as,

$$P(t) = \int_t^\infty N(t') dt' \sim t^{-2\beta}. \quad (7.9)$$

As for both fBm and FPT based arguments, there seems to be no restriction on their applicability based on the value of α . Hence we conjecture that the persistence probability is in fact a sum of the two terms, each resulting from a different set of

actual dynamical trajectories, $P(t) = At^{-(1-\beta)} + Bt^{-2\beta}$ for large t . This form of $P(t)$ easily explains the two exponents for two different ranges of α as the slowly decaying part will dominate the long time behaviour and hence the asymptotic persistence exponent. Thus, for large t , $\min(1 - \beta, 2\beta)$ dominates implying that $\theta = \min(1 - \beta, 2\beta)$ which matches with our numerical results rather well.

Similarly, for other three models, i.e., annealed site, annealed bond and the quenched site, we similarly write the persistence probability as a sum of two terms $P(t) = At^{-\beta} + Bt^{-2\beta}$. In these cases, the asymptotic behaviour is always dominated by the first term and hence the persistence exponent $\theta = \beta$ for the entire range of α . This is consistent with the analytical known result for the survival probability $S(t) \sim t^{-\beta}$ for $t \rightarrow \infty$.

7.3 Summary and concluding remarks

In this chapter, we have studied numerically the persistence properties of a random walker in 1D lattice where disorder in the hopping rates is introduced. We consider four different models depending upon whether the rates are introduced on bonds or sites and as annealed or quenched. The rates are chosen from a power law distribution. The persistence exponent obtained for annealed bond, annealed site and quenched site disorder agrees very well with the prediction from a simple space-time scaling argument. However, the corresponding exponent for the quenched bond disorder model is qualitatively different. The exponent in this case varies non-monotonically with the disorder strength exponent α . Using two different arguments, one based on a result for fractional Brownian motion (fBm) and another using the first passage time distribution we show that the persistence probability in this case is a sum of two terms $P(t) = At^{-(1-\beta)} + Bt^{-2\beta}$. Thus, one of the terms dominates depending on whether β is greater or less than $1/3$, i.e., whether α is greater or less than $1/2$. We further argue that though in cases of annealed bond and site disorder and quenched site disorder we see a single exponent at large time, two exponents, β and 2β are present simultaneously for all α . At large time only the slowly decaying part, having exponent $\min(\beta, 2\beta) = \beta$, shows up in our results. For the quenched bond disorder case, based on numerical studies we conjecture that there seems to be two classes of dynamical trajectories, both

present for all α , responsible for two exponents. It would be interesting to analyze the persistence properties of quenched bond disorder in some more detail as it may provide some new information and explore properties relating to the random motion of particles in this kind of disordered media.

List of symbols

α	Hopping rate exponent
β	Root mean square (RMS) displacement exponent
$C(t_1, t_2)$	Two-point incremental correlation function
$F(t)$	First passage time distribution: $F(t) \equiv F(x_0, t x_0, 0)$
$F(x, t x_0, t_0)$	First passage time distribution that the walker reaches x for the first time at t starting from x_0 at time t_0
γ	Exponent of survival probability distribution
H	Hurst exponent
$l(t)$	RMS displacement of a random walker after time t
μ	waiting time exponent-1
$N(t)$	First return probability
$\omega(\tau)$	Waiting time distribution
$P(t)$	Persistence probability upto time t
$\rho(W)$	Hopping rate distribution
$S(t)$	Survival probability
θ	Persistence exponent
T	$\ln t$
t, τ	Time
$W_{i,j}$	Hopping rate from i-th to j-th site
$x(t)$	Position of the random walker at time t
$\langle x^2(t) \rangle$	Mean square displacement of a random walker after time t

8

Summary

This thesis contains some studies on stochastic paths, especially in the context of unbinding transition of polymers. The unbinding transition occurs when the interaction between the two polymers are varied, or, in the case of the DNA, the pulling force on the strands of a double helical bound DNA is increased. The overall qualitative features for this phase transitions and the phase diagram are very similar to some other system, though the mechanisms or the detailed dynamics are completely different. We explore such connections for better understanding and generic nature of the problem.

The first chapter shows that by using thermodynamic arguments, one can understand the phase diagram and the nature of the phase transition. Our focus is on the interfaces between phases rather than looking at the phases. By emphasizing the fact that the double helical state is a broken symmetry phase compared to the denatured phase, we introduce the helical order parameter to describe melting. Along with this, we put in another modification that the pulling force actually tries to penetrate the zipped phase but experiences resilience and decays to zero after some distance. In our study, we find that the combined effect of the helical order and the force penetration into the zipped phase can actually produce a phase transition which is second order. Moreover, the competition of the two independent length scales, one for the damage in the helical order through the interface and the other for the penetration of force upto a length, can change the sign of the interfacial energy from positive to negative, resulting in a second order phase transition. Because of the similarity of the formulation to that of the superconductors, we name the two classes of DNA as Type I (positive surface energy) and

Type II (negative surface energy).

In the next chapter, we move our attention from a fixed force case to a periodic one, the unzipping of a DNA by an external force on the strands, where the force is varied periodically. Because of the first order nature of the zipping-unzipping phase transition at the critical force, one would expect hysteresis for a periodic force. The results from the MD simulation on a DNA hairpin shows that the standard averaging over many cycles of the force suppresses the actual picture of the states. Here we emphasize the point that one should look at the time-resolved loops, the quantity of interest being the average separation between the two strands over one cycle. The two-state nature of the problem reminds us of another simpler and well-known system, *viz.*, an Ising ferromagnet. Very similar results are shown to be produced from the MC simulation of an Ising ferromagnet under a periodic magnetic field. The relevant quantity for the Ising case is the average magnetization over one cycle. In terms of that we propose a dynamical phase diagram in the magnetic field *vs.* frequency plane. The main lesson one learns from this study is that though the two systems, DNA and the Ising magnet, have completely different dynamics, they behave in a similar way under the periodic drive. The dynamical phase diagram reveals the possibility of the phase transition by varying only the frequency of the external drive.

When a system undergoes a first order phase transition, then under a periodic variation of the parameter inducing the phase transition, the system shows hysteresis. It is because of the mismatch in the time scales of the relaxation of the system and the applied drive. The relaxation time becomes very large near the phase transition. In this context, in the third chapter, we discuss a method to get the equilibrium quantities from nonequilibrium measurements by using the work theorem and the histogram technique. We present a dynamics-independent proof of the work theorem and generalize the theorem to any thermodynamic intensive parameter including the temperature and any arbitrary number of them. The nonequilibrium work connecting to configurations are used to construct a special matrix whose principal eigen-vector is the equilibrium probability distribution. This chapter also shows how an equilibrium curve can be obtained from the nonequilibrium hysteresis loop by using appropriate weight factors. The results are verified by the MC simulation of an Ising magnet.

The focus of the fourth and the fifth chapters is on exploring the connection of

the polymer unbinding transition to the quantum dissociation. An imaginary time transformation maps a classical polymer partition function into a quantum propagator. Thus a problem of two interacting polymers maps on to the problem a two quantum particles interacting via a potential. In the case of the quantum problem, the QPT is achieved by varying the strength of the interaction. The quantum dissociation being a quantum phase transition (QPT), we use the quantum entanglement to observe the signatures of the QPT. The von Neumann entropy shows the special features of a polymer unbinding transition. This is verified analytically for a short-ranged potential and by exact numerical calculations for inverse square potential. The special points or the RG fixed points show different scaling behaviours which are justified from the polymer entropy. We find the quantum entanglement entropy to be negative which can be justified when thought of in terms of the polymer language. The study of the quantum entanglement is then extended to the Renyi entropy where we have extra complexities, though similar type of the scaling behaviour is expected. The exact scaling form is not yet known to us.

Lastly, we go beyond the polymer picture to consider a polymer as a random walker. We study the random walk problem in presence of disorder in the medium. We look at the mean square displacement, two-point correlation function, and the persistence probability as a function of the strength of disorder. The persistence probability can be identified as the reunion probability of the polymer. We study one-dimension random walker with a power-law distribution of hopping rates. According to the assignment of the hopping rates to the left and to the right, one can have random bond model and random site model. For a disordered medium, one may think of two kinds of disorder averaging, quenched and annealed. Thus, we consider all the four cases; quenched site, quenched bond, annealed site, annealed bond disordered cases. For such types of models with broad waiting time distribution, generated by the power-law hopping rate distributions, makes the diffusion anomalous, more specifically, sub-diffusive. Although we start from the same hopping rate distributions, the four cases have different waiting time distributions, two-point correlations and the persistence properties. The results of the quenched site, annealed bond, and annealed site disordered cases are in line with our expectations, while the quenched bond disorder has qualitatively different behaviour. We use a result from the fractional Brownian motion (fBm) and an

argument based on the first passage times to explain the nontrivial dependence of the persistence exponent in the case of quenched bond disorder.

In conclusion, this thesis sees a few polymer problems from a new angle and explores the connections to other systems which are apparently different. The behaviour of the polymers and DNA are studied in equilibrium and nonequilibrium. Viewing a polymer as a fluctuating path, the paths are studied through work theorem, as quantum trajectories, and as random walkers. Thus different topics are unified through the polymer language, hence revealing its generic nature.

Bibliography

- [1] D. Poland and H. Scheraga, *J. Chem. Phys.* **45**, 1456 (1966).
- [2] S. M. Bhattacharjee, *J. Phys. A* **33**, L423 (2000); cond-mat/9912297.
- [3] D. Marenduzzo, S. M. Bhattacharjee, A. Maritan, E. Orlandini and F. Seno, *Phys. Rev. Lett.* **88**, 028102 (2002).
- [4] S. Kumar and M. S. Li, *Phys. Rep.* **486**, 1 (2010).
- [5] R. Kapri, S. M. Bhattacharjee, and F. Seno, *Phys. Rev. Lett.* **93**, 248102 (2004).
- [6] R. Kapri and S. M. Bhattacharjee, *Phys. Rev. E* **72** 051803 (2005).
- [7] R. Kapri and S. M. Bhattacharjee, *Phys. Rev. Lett.* **98** 098101 (2007).
- [8] O. Gotoh, *Adv. Biophys.* **16**, 1 (1983).
- [9] M. Payrard and A. R. Bishop, *Phys. Rev. Lett.* **62**, 2755 (1989).
- [10] D. Marenduzzo et al., *Phys. Rev. Lett.* **88**, 028102 (2001).
- [11] B. H. Zimm, *J. Chem. Phys.* **33**, 1349 (1960).
- [12] M. E. Fisher, *J. Chem. Phys.* **45**, 1469 (1966).
- [13] Y. Kafri, D. Mukamel, and L. Peliti, *Phys. Rev. Lett.* **85**, 4988 (2000).
- [14] Y. Kafri, D. Mukamel, and L. Peliti, *Eur. Phys. J. B* **27**, 132 (2002).
- [15] R. M. Wartell and A. S. Benight, *Phys. Rep.* **126**, 67 (1985).
- [16] A. Kornberg and T. A. Baker, DNA Replication, 2 ed. (W. H. Freeman and Company, New York, 1992).
- [17] M. E. Fisher, *J. Stat. Phys.* **34**, 667 (1984).
- [18] S. Mukherji and S. M. Bhattacharjee, *Phys. Rev. E*, **48** 3427 (1993).
- [19] G. N. Bochkov and Yu E. Kuzovlev *Zh. Eksp. Teor. Fiz.* **72**, 238 (1977) [*Sov. Phys. -JETP* **45**, 125 (1977)].

- [20] C. Jarzynski *Phys. Rev. E* **56**, 5018 (1997).
- [21] G. Hummer and A. Szabo *Proc. Natl. Acad. Sci. USA* **98**, 3658 (2001).
- [22] G. E. Crooks *Phys. Rev. E* **61**, 2361 (2000).
- [23] A. Saha, J. K. Bhattacharjee and S. Chakraborty *Phys. Rev. E*, **83** 011104 (2011).
- [24] M. Suman Kalyan, G. Anjan Prasad, V. S. S. Sastry, K. P. N. Murthy *Physica A* **390** 1240 (2011).
- [25] E. G. D. Cohen and D. Mauzerall *J. Stat. Mech.: Theor. Exp.* P07006 (2004).
- [26] G. N. Bochkov, Y. E. Kuzovlev, arXiv: 1208.1202.
- [27] C. Jarzynski, *Phys. Rev. Lett.* **78**, 2690 (1997).
- [28] C. Jarzynski, *Phys. Rev. E* **56**, 5018 (1997).
- [29] G. E. Crooks, *Phys. Rev. E* **60**, 2721 (1999).
- [30] W. Lechner, H. Oberhofer, C. Dellago, and P. Geissler, *J. Chem. Phys.* **124**, 044113 (2006).
- [31] J. P. Valleau and D. N. Card, *J. Chem. Phys.* **57**, 5457 (1972).
- [32] M. Falcioni et.al. *Phys. Lett. B* **108**, 331 (1982).
- [33] A. M. Ferrenberg and R. H. Swendsen, *Phys. Rev. Lett.* **61**, 2635 (1988).
- [34] Z. W. Salzburg, J. D. Jacobson, W. Fickett and W. W. Wood, *J. Chem. Phys.* **30**, 65 (1959).
- [35] A. M. Ferrenberg and R. H. Swendsen, *Phys. Rev. Lett.* **61**, 2635 (1988).
- [36] I. Bose and E. Chattopadhyay *Phys. Rev. A* **66**, 062320 (2002).
- [37] R. Horodecki, P. Horodecki, M. Horodecki and K. Horodecki *Rev. Mod. Phys.* **81**, 865 (2009).

- [38] L. Amico, R. Fazio, A. Osterloh and V. Vedral *Rev. Mod. Phys.* **80**, 517 (2008).
- [39] G. Vidal, J. I. Latorre, E. Rico and A. Kitaev *Phys. Rev. Lett.* **90**, 227902 (2003).
- [40] A. Einstein, B. Podolsky, and N. Rosen, *Phys. Rev.* **47**, 10 (1935).
- [41] M. B. Plenio and S. Virmani, *Quant. Inf. Comp.* **7**, 1 (2007).
- [42] A. Renyi, *Proc. Fourth. Berkeley Symp. Math. Stat. Prob.* 1960, Vol. I, University of California Press, Berkeley, 1961, p. 547.
- [43] J. Pipek and I. Varga, *Phys. Rev. A* **46**, 3148 (1992).
- [44] See, e.g., the articles in the special issue *J. Phys.A: Math. Theor.* **42**, 500301 (2009).
- [45] A. Osterloh, L. Amico, G. Falci, and R. Fazio *Nature* **416**, (2002) 608.
- [46] J. S. Dehesa, T. Koga, R. J. Yanez, A. R. Plastino, and R. O. Esquivel, *J. Phys. B: At. Mol. Opt. Phys.* **45**, 015504 (2012).
- [47] D. Slepian, *Bell Syst. Tech. J.* **41**, 463 (1962).
- [48] J. P. Bouchaud and A. Georges, *Phys. Rep.* **195**, 4-5, p.127-293 (1990).
- [49] R. Engelman and Z. Jaeger, *Fragmentation Form and Flow in Fractured Media* (Bristol: IPS) (1986).
- [50] E. Guyon, J. P. Hulin and R. Lenormand, *Ann. Mines*, **17**, 40 (1984).
- [51] J. Nittmann, G. Daccord and H. E. Stanley, *Nature*, **314**, 141 (1985); J. Nittmann, G. Daccord and H. E. Stanley, *Nature*, **321**, 663 (1986).
- [52] Y. Uemura and R. J. Birgeneau, *Phys. Rev. Lett.*, **57**, 1947.
- [53] E. Courtens, J. Pelous, J. Phalippou, R. Vacher and T. Woignier, *Phys. Rev. Lett.*, **58**, 128 (1987).
- [54] A. Avogadro, S. Aldrovandi, and F. Borsa, *Phys. Rev. B*, **33**, 5637 (1986).

- [55] G. Grinstein, and J. F. Fernandez, *Phys. Rev. B*, **29**, 6389 (1984); R. J. Birgenau, G. Shirane, and H. Yoshizawa, *Phys. Rev. Lett.*, **54**, 2147 (1985).
- [56] N. Levitt, *Ann. Rev. Biophys. Bioengng*, **11**, 251 (1982).
- [57] J. Bernasconi, J. U. Beyeler, S. Strassler, and S. Alexander, *Phys. Rev. Lett.*, **42**, 819 (1979).
- [58] A. Kapitulnik, and G. Deutscher, 1982, *Phys. Rev. Lett.*, **49**, (1944).
- [59] R. Voss, R. Leibowitz, and E. Alessandrini, *Phys. Rev. Lett.*, **49**, 1441 (1982).
- [60] A. Palevski, and G. Deutscher, *J. Phys. A*, **17**, L895 (1984).
- [61] R. Kopelman, *J. statist. Phys.*, **42**, 185 (1986).
- [62] Ya. G. Sinai, *Theory of Prob. and Appl.* 27(2), 247 (1982).
- [63] F. J. Dyson, *Phys. Rev.*, **92**, 1331 (1953).
- [64] J. Schmidt, *Phys. Rev.*, **105**, 425 (1957).
- [65] C. Domb, *Proc. R. Soc.*, **276**, 418 (1963).
- [66] B. I. Halperin, *Phys. Rev. A*, **139**, 104 (1965); *Adv. chem. Phys.*, **13**, 123 (1966).
- [67] J. Bernasconi, S. Alexander, and R. Orbach, *Phys. Rev. Lett.*, **41**, 185 (1987).
- [68] S. Alexander, *Phys. Rev. B*, **23**, 2951 (1981).
- [69] S. Alexander, J. Bernasconi, W. R. Schneider, and R. Orbach, *Rev. mod. Phys.* **53** 175 (1981).
- [70] G. Bonnet, O. Krichevsky, and A. Libchaber, *Proc. Natl Acad. Sci.* **95**, 8602 (1998).
- [71] S.J. Chen and K.A. Dill, *Proc. Natl. Acad. Sci.* **97** 646 (1997).
- [72] G. Mishra, P Sadhukhan, S. M. Bhattacharjee and S. Kumar, arxiv:1204.2913.

- [73] P. de Gennes, *Comptes Rendus de l'Académie des Sciences - Series IV - Physics* **2**, 1505 (2001).
- [74] J. D. Watson et. al., *Molecular Biology of the Gene*, 6th Ed. (Pearson Education, Singapore) 2008
- [75] B. B. Goodman, *Rev. Mod. Phys.* **36**, 12 (1964).
- [76] X. Q. Cao, J. Zeng and H. Yan, *Phys. Rev. E* **77**, 041908 (2008).
- [77] C. H. Choi *et al*, *Biophys. J.* **95**, 597 (2008).
- [78] J. van Mameren *et al*, *Proc. Natl. Acad. Sci.* **106**, 18231 (2009).
- [79] D. Marenduzzo, E. Orlandini, F. Seno and A. Trovato, *Phys. Rev. E* **81**, 051926 (2010).
- [80] G. L. Randall, L. Zechiedrich and B. M. Pettitt, *Nucl. Acids Res.* **37**, 5568 (2009).
- [81] F. Mueller-Planitz and D. Herschlag, *Nucl. Acids. Res.* **35**, 3764 (2007).
- [82] A. A. Abrikosov, *Soviet Physics JETP* **5**, 1174 (1957).
- [83] I. Donmez and S. S. Patel, *Nucl. Acids Res.* **34**, 4216 (2006).
- [84] S. S. Velankar, P. Soultanas, M. S. Dillingham, H. S. Subramanya, and D. B. Wigley, *Cell* **97**, 75 (1999).
- [85] M. F. Williams and E. Jankowsky, *J. Mol. Biol.* **415**, 819 (2012).
- [86] G. Mishra, D. Giri, M. S. Li, and S. Kumar, *J. Chem. Phys.* **135**, 035102 (2011).
- [87] R. Kapri, arXiv:1201.3709 (2012).
- [88] G. Bertotti *Hysteresis in Magnetism : For Physicists, Material Scientists and Engineers* (London Academic Press) (1998).
- [89] B. K. Chakrabarti and M. Acharyya, *Rev. Mod. Phys.* **71**, 847 (1999).

- [90] S. M. Bhattacharjee and F. Seno, *J. Phys. A* **36**, L181 (2003); S. M. Bhattacharjee, *Europhysics Lett.* **65**, 574 (2004) ; *J. Phys.: Condens. Matter* **22**, 155102 (2010) ; M. D. Betterton and F. Jülicher, *J. Phys.: Condens. Matter* **17**, S3851 (2005).
- [91] P. Sadhukhan, J. Maji, and S. M. Bhattacharjee, *EuroPhys. Lett.* **95**, 48009 (2011).
- [92] A. N. Gupta et. al., *Nature Physics* **7**, 631 (2011).
- [93] The value $g_c \sim 0.2$ is from Fig. 4a of [86], marked by an arrow there. We have chosen $T = 0.1$ because hysteresis starts occurring as noted there.
- [94] H. Barkhausen *Z Phys.* **20**, 401 (1919).
- [95] G. Bertotti, *Hysteresis in magnetism*, Academic, San Diego, 1998.
- [96] N. I. Akhiezer, *The classical moment problem* (Oliver and Boyd, Edinburgh, 1965).
- [97] Bhattacharyya A *Bull. Cal. Math. Soc.* **35**, 99 (1943).
- [98] A. Kopp, X. Jia and S. Chakravarty *Ann. Phys.* **322** 1466 (2007).
- [99] F. Igloi and R. Juhasz *Europhys. Lett.* **81**, 57003 (2008).
- [100] M. E. Fisher *J Stat. Phys.* **34**, 667 (1984).
- [101] S. Mukherji and S. M. Bhattacharjee *J. Phys. A: Math Gen.* **26**, L1139 (1993).
- [102] M. E. Fisher *J. Chem. Phys.* **45**, 1469 (1966).
- [103] M. Haque, O. S. Zozulya and K. Schoutens *J. Phys. A: Math Theor.* **42**, 504012 (2009).
- [104] M. Doi and S. F. Edwards, *Theory of Polymer Dynamics*, (International Series of Monographs on Physics, 73, Oxford U press, Oxford, 1988).
- [105] L. Rio, J. Aberg, R. Renner, O. Dahlsten and V. Vedral *Nature* **474**, 61 (2011).

- [106] P. Sadhukhan and S. M. Bhattacharjee *Europhys. Lett.* **98**, 10008 (2012).
- [107] S. Mukherji and S. M. Bhattacharjee *Phys. Rev. E* **63**, 051103 (2001).
- [108] E. B. Kolomeisky and J. P. Straley *Phys. Rev. B* **46**, 12664 (1992).
- [109] L. D. Landau and L. M. Lifshitz *Quantum Mechanics Non-Relativistic Theory*, 3 ed., Butterworth-Heinemann, Amsterdam (2004).
- [110] P. J. Mohr, B. N. Taylor and N. D. Newell *Rev. Mod. Phys.* **80**, 633 (2008).
- [111] E. H. Lieb and M. B. Ruskai *Phys. Rev. Lett.* **30**, 434 (1973).
- [112] H. van Haeringen *J. Math. Phys.* **19** 2171 (1978).
- [113] S. Havlin and D. Ben-Avraham, Diffusion in disordered media, *Adv. Phys.* **36**, 695 (1987).
- [114] H. Scher and M. Lax, *Phys. Rev. B* **7**, 4491 (1973).
- [115] H. Scher and E.W. Montroll, *Phys. Rev. B* **12**, 2455 (1975).
- [116] M.F. Shlesinger, *J. Stat. Phys.* **10**, 421 (1974).
- [117] J. Klafter and R. Silbey, *Phys. Rev. Lett.* **44**, 56 (1980).
- [118] A. Blumen, J. Klafter, and G. Zumofen, *Phys. Rev. B* **27**, 3429 (1983).
- [119] S. Alexander, and R. Orbach, *J. Phys. Lett.*, **43**, L625 (1982).
- [120] I. Webman, *Phys. Rev. Lett.*, **47**, 1497 (1981).
- [121] D. Ben-Avraham, and S. Havlin, *J. Phys. A*, **15**, L691 (1982); S. Havlin, D. Ben-Avraham, and H. Sompolinsky, *Phys. Rev. A*, **27**, 1730 (1983).
- [122] Y. Gefen, A. Aharony, and S. Alexander, *Phys. Rev. Lett.*, **50**, 77 (1983).
- [123] R. Rammal, and G. Toulouse, *J. Phys. Lett.*, **44**, L13 (1983).
- [124] J. Bernasconi, J. U. Beyeler, S. Strassler, and S. Alexander, *Phys. Rev. Lett.*, **42**, 819 (1979).
- [125] B. I. Halperin, S. Feng, and P. N. Sen, *Phys. Rev. Lett.*, **54**, 2391 (1985).

- [126] F. J. Dyson, *Phys. Rev.*, **92**, 1331 (1953).
- [127] A. Bunde, H. Harder, and S. Havlin, *Phys. Rev. B*, **34**, 3540 (1986).
- [128] H. Sompolinsky, *Phys. Rev. Lett.*, **47**, 935 (1981).
- [129] S. Teitel, and E. Domany, *Phys. Rev. Lett.*, **5**, 2176 (1985).
- [130] J. Krug, H. Kallabis, S. N. Majumdar, S. J. Cornell, A. J. Bray, and C. Sire, *Phys. Rev. E* **56**, 2702 (1997).
- [131] M. Ding and W. Yang, *Phys. Rev. E* **52**, 207 (1995).